

AD-A196 542

UNCLASSIFIED

SECURITY CLASSIFICATION OF THIS PAGE (When Data Entered)

DTIC FILE COPY

①

REPORT DOCUMENTATION PAGE		READ INSTRUCTIONS BEFORE COMPLETING FORM
REPORT NUMBER AFIT/CI/NR 88-20	2. GOVT ACCESSION NO.	3. RECIPIENT'S CATALOG NUMBER
TITLE (and Subtitle) ANALYSIS OF TEMPERATURE AND VELOCITY MICROTURBULENCE PARAMETERS FROM AIRCRAFT DATA AND RELATIONSHIP TO ATMOSPHERIC REFRACTIVE INDEX STRUCTURE		5. TYPE OF REPORT & PERIOD COVERED MS THESIS
		6. PERFORMING ORG. REPORT NUMBER
AUTHOR(s) ELIZABETH A. BEECHER		8. CONTRACT OR GRANT NUMBER(s)
PERFORMING ORGANIZATION NAME AND ADDRESS AFIT STUDENT AT: PENN STATE UNIVERSITY		10. PROGRAM ELEMENT, PROJECT, TASK AREA & WORK UNIT NUMBERS
1. CONTROLLING OFFICE NAME AND ADDRESS		12. REPORT DATE 1988
		13. NUMBER OF PAGES 165
11. MONITORING AGENCY NAME & ADDRESS (if different from Controlling Office) AFIT/NR Wright-Patterson AFB OH 45433-6583		15. SECURITY CLASS. (of this report) UNCLASSIFIED
		15a. DECLASSIFICATION/DOWNGRADING SCHEDULE
16. DISTRIBUTION STATEMENT (of this Report) DISTRIBUTED UNLIMITED: APPROVED FOR PUBLIC RELEASE		
17. DISTRIBUTION STATEMENT (of the abstract entered in Block 20, if different from Report) SAME AS REPORT		
18. SUPPLEMENTARY NOTES Approved for Public Release: IAW AFR 190-1 LYNN E. WOLAVER Dean for Research and Professional Development Air Force Institute of Technology Wright-Patterson AFB OH 45433-6583		
19. KEY WORDS (Continue on reverse side if necessary and identify by block number)		
20. ABSTRACT (Continue on reverse side if necessary and identify by block number) ATTACHED		

DTIC
SELECTED
AUG 03 1988
H

ABSTRACT

Due to inherent turbulence, the atmosphere has a temporally and spatially variable refractive index, which degrades propagating electromagnetic radiation. C_n^2 is a key parameter for describing refractive variations. Data was analyzed from several instruments involved in an electro-optics/meteorology experiment at Penn State University: scintillometer (RADC, AFGL, NPS), thermosonde (AFGL), radar vertical profiler (PSU), and instrumented aircraft (ARA). The aircraft measured C_T^2 and C_u^2 using hot- and cold-wire sensors and FM recording apparatus. The taped data was processed via FFT to produce one-dimensional variance spectra (wavenumber range 0.01 to 10 m^{-1}). Flights usually produced a 10 km vertical profile processed to give roughly 0.5 km resolution. Spectral editing was based on regression analysis fit to $-5/3$ frequency dependence. A majority of spectra showed the classic inertial subrange. C_n^2 and ϵ were calculated from C_T^2 and C_u^2 , respectively. In active regions, the following relationship can be derived (Fairall and Markson 1984):

$$C_T^2 / C_u^2 = 1.6 R_i / (P_r - R_i) (\theta/g) (\partial\theta/\partial z)$$

A scatter plot of C_T^2 vs. $(\theta/g \partial\theta/\partial z) C_u^2$ in the free troposphere showed a range of values from 0.3 to 10 for high and low values of C_T^2 , respectively. C_T^2 versus C_u^2 showed high correlation, with $\log C_u^2 = 1.7 \log C_T^2$. Plots of $C_T^2/C_u^2 (\theta/g \partial\theta/\partial z)$ vs. $\epsilon/(\nu N)$ (Gregg 1987) approached an ordinate value of 0.4 at high activity levels. Values of N and S were

used to obtain values of C_n^2 and ϵ with the model of VanZandt et al. (1981). Comparisons of C_n^2 profiles showed average ratios of each to the thermosonde profile were: aircraft 8, model 6.8, profiler 8.1, and the scintillometer 1.1. Numerical estimates of θ_0 from C_n^2 profiles differed from the aircraft by an average of 17% for the thermosonde and scintillometer. Estimates of r_0 differed by 35% for the thermosonde. Aircraft-measured and model-predicted values of ϵ differed by several orders of magnitude.



Accession For	
NTIS GRA&I	<input checked="" type="checkbox"/>
DTIC TAB	<input type="checkbox"/>
Unannounced	<input type="checkbox"/>
Justification	
By	
Distribution/	
Availability Codes	
Dist	Avail and/or Special
A-1	

The Pennsylvania State University

The Graduate School

Department of Meteorology

Analysis of Temperature and Velocity Microturbulence Parameters
from Aircraft Data
and Relationship to Atmospheric Refractive Index Structure

A Thesis in

Meteorology

by

Elizabeth A. Beecher

Submitted in Partial Fulfillment
of the Requirements
for the Degree of

Master of Science

May 1988

I grant The Pennsylvania State University the nonexclusive right to use this work for the University's own purposes and to make single copies of the work available to the public on a not-for-profit basis if copies are not otherwise available.

Elizabeth A. Beecher

We approve the thesis of Elizabeth A. Beecher.

Date of Signature:

12/11/87

C. W. Fairall

Christopher W. Fairall, Associate Professor
of Meteorology, Thesis Advisor

11.12.87

Dennis W. Thomson

Dennis W. Thomson, Professor of Meteorology

11 Dec 87

William M. Frank

William M. Frank, Associate Professor of
Meteorology, Head of the Department of
Meteorology

ABSTRACT

Due to its inherently turbulent nature, the atmosphere has a temporally and spatially variable refractive index, which degrades propagating electromagnetic radiation. The refractive index turbulent structure constant, C_n^2 , is a key parameter for describing refractive variations. C_n^2 can be inferred from optical turbulence (scintillometer), temperature turbulence (aircraft instrumentation or thermosonde) or radar backscatter (profiler) measurements. Vertical integrals of C_n^2 give transverse coherence length, r_0 , and isoplanatic angle, θ_0 . These can also be measured remotely by an r_0 scintillometer and isoplanometer, respectively.

During an atmospheric optics/meteorology experiment (acronym EWAK) conducted at Penn State University primarily during April and May of 1986, data was collected by all of the aforementioned instruments. An instrumented research aircraft was used to measure vertical profiles of temperature and velocity turbulence (C_T^2 and C_u^2) and other meteorological variables. The turbulence instrumentation aboard the aircraft consisted of cold-wire and hot-wire sensors and FM recording apparatus. The taped data was processed via FFT to produce one-dimensional variance spectra (wavenumber range 0.01 to 10 m^{-1}). Flights usually produced a 10 km vertical profile; the data was processed to give roughly 0.5 km vertical resolution (similar to that of the radar wind profiler).

Editing was based on percent error between a regression analysis and theoretical $-5/3$ frequency dependence of the spectra. A majority of spectra showed good evidence of the classic inertial subrange with

-5/3 slope. C_T^2 and C_u^2 were calculated from the regression fit to the inertial subrange power spectral density. The rate of dissipation of turbulent kinetic energy, ϵ , was calculated using the so-called Corrsin relation for velocity turbulence. Optical C_n^2 was calculated from C_T^2 .

Considerable interest has developed in models that relate microturbulence parameters to the mean gradients. One such model, proposed by VanZandt et al. (1978; 1981), has as a key variable the gradient Richardson number, R_i . In actively turbulent regions, R_i can be related to C_T^2 and C_u^2 as follows:

$$C_T^2 / C_u^2 = 1.6 R_i / (P_r - R_i) (\theta/g) (\partial\theta/\partial z)$$

A scatter plot of C_T^2 versus $(\theta/g \partial\theta/\partial z) C_u^2$ in the free troposphere showed a range of values from 0.3 to 10 for high and low values of C_T^2 , respectively. Scatter plots of C_T^2 versus C_u^2 showed high correlation of these two parameters, with $\log C_u^2 = 1.7 \log C_T^2$. $R_i = N/S$ and plots of N versus S roughly corresponded to the curve depicted by Fairall and Markson (1985).

Plots of $C_T^2 / C_u^2 (\theta/g \partial\theta/\partial z)$ versus a turbulent activity parameter (Gregg 1987) clearly showed agreement with the suggested activity levels and associated values. At high activity levels, the ordinate value approached 0.4 (equivalent to $1.6 R_i$ when approximating P_r as 1 and R_i as 0.25).

Values of N and S were used to obtain values of C_n^2 and ϵ with the model of VanZandt et al. Comparisons of C_n^2 profiles measured by the various instruments showed good agreement between scintillometer and thermosonde, and between the VanZandt et al. model

and the aircraft data. The profiler (converted optical values) had some agreement with the thermosonde. Average ratios of each profile to the thermosonde profile were: aircraft 8, model 6.8, profiler 8.1, and the scintillometer 1.1.

Numerical integration of C_n^2 gave estimates of r_o and θ_o . Values from scintillometer, thermosonde and aircraft did not show clear agreement. Based on the aircraft values, the scintillometer and thermosonde θ_o values differed by an average of 17%. The thermosonde r_o values differed by an average of 35%.

Despite good agreement on C_n^2 , the aircraft data and the VanZandt et al. model output clearly disagreed on vertical profiles of ϵ , in some cases by several orders of magnitude.

Overall, EWAK provided a chance to compare methods of measuring C_n^2 , as well as an opportunity to obtain microturbulence data for examining relations to the mean gradient structure.

TABLE OF CONTENTS

	<u>Page</u>
ABSTRACT.....	iii
LIST OF TABLES.....	viii
LIST OF FIGURES.....	ix
ACKNOWLEDGEMENTS.....	xii
<u>Chapter</u>	
1 INTRODUCTION.....	1
2 BACKGROUND ON ATMOSPHERIC PROPAGATION.....	3
2.1 Refractive Index.....	3
2.2 Propagation Effects.....	5
2.3 Propagation Parameters and C_n^2 Measurements.....	7
3 MICROTURBULENCE THEORY.....	10
3.1 The Refractive Index Structure Function...	10
3.2 C_n^2 From Radar Measurements.....	12
3.3 C_T^2 and C_u^2 Relationships.....	13
3.4 The Turbulent Kinetic Energy Dissipation Rate.....	16
3.5 Turbulence Size Scales.....	17
4 THE EWAK EXPERIMENT.....	19
4.1 Overview.....	19
4.2 Aircraft Instrumentation.....	22
4.3 Additional Instrumentation.....	23
5 DATA PROCESSING.....	25

TABLE OF CONTENTS
(continued)

<u>Chapter</u>		<u>Page</u>
6	ANALYSIS METHODS.....	37
6.1	Aircraft Turbulence Data Analysis.....	37
6.2	Mean Aircraft Meteorological Profiles.....	53
6.3	Other Data Sources.....	54
7	RESULTS AND DISCUSSION.....	73
7.1	Analysis of C_T^2/C_u^2	73
7.2	Mean Gradients and Richardson Number.....	114
7.3	Profiles of C_n^2	128
7.4	Propagation Parameters.....	145
7.5	VanZandt et al. Model for ϵ	150
8	SUMMARY AND CONCLUSIONS.....	157
	REFERENCES.....	163

LIST OF TABLES

<u>Table</u>		<u>Page</u>
1	Aircraft flight logistics and corresponding data from other instruments during EWAK.....	20
2	Representative editing results for each flight and in total.....	51
3	Estimates of the height of the PBL based on the strength of the signal-to-noise ratio exhibited in the spectra.....	89
4	Calculated vertical profiles of Richardson number based on $R_i = N/S$ and using N and S values shown in Figure 17.....	120
5	The arithmetically averaged Richardson number at each height for all vertical flights.....	123
6	X^2 vertical profiles for each flight during which the profiler operated, calculated at each aircraft observation level in MSL altitude with aircraft-measured temperature and specific humidity profiles.....	129
7	X^2 vertical profiles for each flight during which the profiler operated, calculated at each profiler observation level in MSL altitude with aircraft-measured temperature and specific humidity profiles.....	132
8	Arithmetically averaged X^2 vertical profiles from the Table 7 profiles.....	135
9	AFGL-calculated optical parameters from thermosonde data.....	147
10	Average of AFGL-calculated optical parameters from scintillometer data.....	148
11	Optical parameters from aircraft data calculated with the Murphy and Battles assumptions.....	149

LIST OF FIGURES

<u>Figure</u>		<u>Page</u>
1	Voltage variance spectra from first FFT program (128 points).....	31
2	Voltage variance spectra produced by the signal analyzer's 1600 point FFT.....	34
3a	The measured 2 Hz high pass temperature turbulence channel filter.....	38
3b	The measured 5 Hz high pass velocity turbulence channel filter.....	38
4a	The derived atmospheric 2 Hz high pass temperature turbulence channel filter.....	40
4b	The derived atmospheric 5 Hz high pass velocity turbulence channel filter.....	40
5a	Voltage variance spectra showing editing procedure.	41
5b	Voltage variance spectra showing editing procedure.	44
5c	Voltage variance spectra showing editing procedure.	47
6	Potential temperature (θ) vertical profiles as measured by aircraft instrumentation.....	55
7	Specific humidity vertical profiles as measured by aircraft instrumentation.....	60
8	Mean wind speed (solid line) and direction (broken line) as measured by the profiler.....	63
9	AFGL thermosonde-measured potential temperature vertical profiles correlating to aircraft flights..	66
10	AFGL thermosonde-measured specific humidity vertical profiles correlating to aircraft flights..	67
11	AFGL thermosonde-measured vertical profiles of mean wind speed (solid line) and direction (broken line).....	68
12	AFGL thermosonde-calculated vertical ₂ profiles of raw C_n^2 -optical based on measured C_T	69

LIST OF FIGURES
(continued)

<u>Figure</u>	<u>Page</u>
13 AFGL scintillometer-measured vertical profiles of C_n^2 -optical taken during the aircraft flight time period.....	71
14 RADC scintillometer-measured vertical profiles of C_n^2 -optical taken during the aircraft flight time period.....	72
15 Vertical profiles of C_n^2 , C_T^2 , and C_u^2	74
16 A comparison for each vertical flight of C_T^2 versus C_u^2 for spectra above the PBL.....	90
17 A comparison for each level flight of C_T^2 versus C_u^2 for spectra above the PBL.....	98
18 A composite comparison of C_T^2 versus C_u^2 for all vertical profiles.....	100
19 A composite comparison of C_T^2 versus C_u^2 for all level profiles	103
20 A composite comparison of C_T^2 versus C_u^2 normalized by the expression $[T/g (\partial T/\partial z + \Gamma)]$	104
21 Comparison for each vertical profile of C_T^2 divided by C_u^2 normalized as in Figure 20 versus a turbulent activity parameter, $\epsilon/(\nu N)$	106
22 A composite comparison of C_T^2 divided by C_u^2 normalized as in Figure 20 versus a turbulent activity parameter $\epsilon/(\nu N)$ for all vertical profiles.....	115
23 Comparisons of the VanZandt et al. parameters N, the Brunt-Vaisala frequency squared, and S, the shear squared.....	116
24 A composite comparison of N versus S for all flights shown in Figure 23.....	119
25 Comparison of the VanZandt et al. model vertical profile prediction of C_n^2 -optical (solid line) and the aircraft C_T^2 -derived vertical profile of C_n^2 -optical (broken line).....	124

LIST OF FIGURES
(continued)

<u>Figure</u>	<u>Page</u>
26 A comparison of C_n^2 -radar as derived from profiler (solid line) and from aircraft C_n^2 -optical, multiplied by the conversion factor X^2 to give C_n^2 -radar (broken line).....	137
27 Comparison of vertical profiles of C_n^2 -optical.....	141
28 Comparison of vertical profiles of C_n^2 -optical.....	143
29 Comparison of vertical profiles of epsilon (ϵ), the turbulent kinetic energy dissipation rate, predicted by the VanZandt et al. model (solid line) and measured by the aircraft (broken line)...	151
30 Average vertical profile of eta (η), the turbulence inner size scale, from aircraft- measured epsilon profiles.....	155

ACKNOWLEDGEMENTS

First and foremost, I would like to express my sincerest gratitude to my thesis advisor, Dr. Christopher W. Fairall. Without his gentle guidance and patient corrections, this work could not have been completed. I also acknowledge Dr. Dennis W. Thomson for his helpful suggestions concerning my work. A special thanks to my fellow graduate students, Mark Miller and James Edson, and their computer expertise that they so willingly shared.

With regard to my program coursework, I thank Dr. Craig F. Bohren and his humor for putting a smile on my face whenever I needed one and for always reminding me of the sheer joy of studying a physical science.

Thanks also to all those involved in EWAK who provided their time, expertise, instruments, and data, and who answered my multitudinous questions: Dr. Ralph Markson (ARA), Capt Mike Moss (Florida State University), Mr. Donald Stebbins (RADC), Mr. Paul Cook (RADC), Mr. James Brown (AFGL), Mr. Robert Beland (AFGL), Mr. Edmund Murphy (AFGL), Dr. Donald Walters (NPS) and Capt Jack Davidson (AFWL).

Finally, I would like to thank my loving husband, Jeff Beecher, for providing "R and R" when needed, as well as always willingly acting as my sounding board for ideas and my source of practical mechanical knowledge.

This research was sponsored in part by the U. S. Air Force under contract #AFOSR-86-0049.

CHAPTER 1

INTRODUCTION

For many reasons, there is considerable interest in the vertical profile of the refractive index structure parameter, C_n^2 . This parameter quantifies effects of refractive index fluctuations important for electromagnetic radiation systems whose signals propagate through the turbulent atmosphere. Examples of such systems are satellite communications, remote sensing such as clear air radars, astronomical observation, and certain weapons. In situ measurements are a necessary first step to set up a database for verifying physical and numerical models. Both are required to facilitate the interpretation of remote sensing measurements and to achieve the goal of prediction based on readily available atmospheric data and models.

This project was an analysis of the first segment of the EWAK (E xperiment W ithout AK ronym) electro-optical/meteorological experiment at Penn State University. The purpose of EWAK, conducted principally in April and May of 1986, was to simultaneously operate at the same location several different instruments to measure the refractive index structure parameter, both in situ and remotely, throughout different synoptic and diurnal conditions.

Specifically, this thesis describes a detailed analysis of research aircraft measurements of temperature and velocity turbulence taken with the instrumented Beechcraft Baron of the Airborne Research Associates of Weston, Massachusetts. From these two measurements can be derived the temperature and velocity structure parameters, C_T^2 and C_u^2 . Optical C_n^2 is a function of C_T^2 . The turbulent

kinetic energy dissipation rate, ϵ , is related to C_u^2 . Another important relationship examined was that between C_T^2 and C_u^2 .

CHAPTER 2

BACKGROUND ON ATMOSPHERIC PROPAGATION

2.1 Refractive Index

A turbulent fluid creates three general effects: it imposes varying forces on any objects embedded in the fluid or in the fluid path, it generates fluxes of fluid properties (e.g., temperature or momentum), and it creates (by density fluxes) variations in the refractive index of the fluid (Panofsky and Dutton 1984). These refractive index variations will affect electromagnetic (EM) and sonic radiation propagating through the fluid. The atmosphere, being a turbulent fluid, has a temporally and spatially variable refractive index structure. The atmosphere's turbulent refractive index fluctuations have plagued astronomers since some of the earliest recorded observations. The twinkling of stars is one of the most obvious visible manifestations. Today, our atmospheric uses of EM radiation are far more diverse than merely receiving visible starlight with our eyes or at a telescopic aperture. Hence, the need exists to characterize and predict the refractive index and its variations over arbitrary pathlengths and view angles.

Henceforth, in this thesis, unless it is specifically otherwise stated, the discussion will be concerned with propagating electromagnetic radiation. Refraction can be considered as a type of scattering (i.e., deviation from the forward direction). Turbulent, non-homogeneous variations of the atmospheric refractive index are on the order of one part in 10^6 . This results in very small scattering angles, for which depolarization and intensity attenuation generally

can be neglected (Strohbehn 1978). The real part of the complex refractive index, n , of a medium can be thought of as a measure of the medium's effect on wave propagation as compared to propagation in a vacuum: $n(\text{medium}) = c(\text{vacuum})/c(\text{medium})$, where c is the phase velocity of the wave. Refractivity, usually denoted by N , is $(n-1) \times 10^6$. The phase speed of the wave is altered (slowed in air compared to vacuum, thus $n > 1$), but the energy E and frequency ν remain the same, $E = h\nu$ (Hecht 1986). Using geometric optics theory, this can be shown to result in a deviation of the beam's path which is referred to as the phenomenon of refraction (in molecular dipole theory, it is referred to as a scattering event).

Two factors determine the phase speed (and thus refractive index) in a medium: density (number of atoms, molecules or particles per unit volume) and, since each molecule has a wavelength dependent polarizability, molecular composition (Hecht 1986). At optical or shorter wavelengths, temperature variations effectively dominate refractivity changes since atmospheric molecules have low rotational polarizability at these wavelengths (Balsley and Gage 1980). However, at longer wavelengths, specifically microwave radar wavelengths, both temperature and the relative concentration of various molecular species with permanent dipole moments determine the refractive index gradients affecting radiation transmittance (Wesely 1976; Balsley and Gage 1980). In the boundary layer, water vapor content is often highly variable, and thus, may dominate refractivity changes (Balsley and Gage 1980).

If temperature and molecular composition varied negligibly from the standard atmosphere, then the refractive index profile could

easily be calculated. The importance of turbulence is its resultant mixing (Strohbehn 1978). Mixing due to turbulence causes the variations in space and time of the refractive index profile. It is the random nature of turbulence that introduces chaos into the density profile.

2.2 Propagation Effects

Variations in refractive index can cause at least six types of EM propagation degradation: beam steering, image dancing, beam spread, spatial coherence degradation, temporal coherence degradation, and scintillation (Dewan 1980).

Beam steering is deviation from the line-of-sight (i.e., the most direct path from source to receiver). The transverse deviation of a narrow beam increases with subsequent distance from the deviating medium. If a turbulent eddy is larger than the width of the beam, it may act as a "prism." This effect can be quite significant for earth-to-space uplinks, because the planetary boundary layer (PBL) is highly turbulent (Dewan 1980).

Image dancing is the modulation of the arrival angle of the whole beam wavefront. It can cause the focal plane for the beam to be angled to a receiver normal to the beam, causing photographic blurring or necessitating larger apertures with lower signal-to-noise ratios (Dewan 1980).

Beam spreading is caused by scattering at small angles near the edge of the beam. This occurs when the beamwidth is greater than the turbulent eddies. This phenomenon occurs most on the space-to-earth downlink (Dewan 1980).

At large distances, a spherical wave from a point source can be approximated as a plane wave. According to Huygen's model, a single wavefront can be thought to consist of an infinite number of points each emitting a "wavelet." The wavelets add together to give the total wave. If the wavelets have a constant phase relation, the wavefront is said to be coherent. When phase difference randomly and continuously changes, the wavefront becomes incoherent (Hecht 1986). When a pathlength difference is introduced across a coherent wavefront (e.g., refraction), a Fraunhofer diffraction pattern may be seen in which maxima/minima occur where the amplitudes of wavelets constructively/destructively interfere. Thus diffraction is one method of testing coherence (Hecht 1986).

A coherent source can be viewed as emitting "pulses," or wave packets (this model combines wave and particle concepts). No source is perfectly monochromatic, thus each wave pulse has a frequency bandwidth. The inverse of the pulse frequency band is the "period" band or coherence period (Hecht 1986). Temporal (or longitudinal) coherence occurs within the coherence period. Spatial (or horizontal) coherence occurs across a wave pulse emitted from a coherent source. Spatial degradation is loss of phase coherence across a wavefront, causing spot blurring on photographic images. It also distorts photomixing processes which rely on mixing of an incoming to a local signal to form a "beat." Temporal degradation is a loss of phase coherence during the coherence period, thus distorting amplitude modulated signals (Dewan 1980).

Scintillation is a coherence effect describing amplitude changes at a focal plane (interference patterns). Spatial scintillation being

fluctuations across a beamwidth (or wavefront), temporal scintillation being fluctuations in time of the total beam amplitude (signal fading) (Dewan 1980).

2.3 Propagation Parameters and C_n^2 Measurements

A variety of theories have been developed for these degradation effects. In general, an atmospheric turbulence parameter, the refractive index structure constant, C_n^2 , must be specified along the propagation path. By measuring some relevant propagation parameter (e.g., scintillation) the theory can be "inverted" to determine C_n^2 .

One such instrument, the NOAA (National Oceanic and Atmospheric Administration) scintillometer, measures C_n^2 -optical remotely, based on starlight amplitude fluctuations. As one of the six distortions described previously, scintillation has been quantified using an integral of $C_n^2(z)$, where z is the altitude. Tatarskii has shown for temporal scintillations, time averaged amplitude fluctuations (Dewan 1980), that

$$\langle [\ln(A/A_0)]^2 \rangle = 0.56 \quad k^{7/6} \int_0^z C_n^2(z) z^{5/6} dz \quad (2.1)$$

where A is the signal amplitude, A_0 is the mean amplitude, k is the optical wave number, and the angle brackets denote a time average. A stellar scintillometer measures $\sigma_I^2(d_i)$, the normalized variance of the spatially filtered signal irradiance for 3 spatial wavelengths, d_i . Then a profile of C_n^2 is calculated for seven predetermined levels, based on seven weighting functions (only four of which are independent)

$$C_n^2 = B \sum_{i=1}^3 R_i K_i^{8/3} \sigma_I^2(d_i) \quad (2.2)$$

where R_i weight is given to the i th spatial wavenumber K_i ($K_i = 2\pi/d_i$) and

$$B = 1.87 \times 10^{-13} \left[\int_0^\infty W_c(z) dz \right]^{-1} \quad (2.3)$$

where $W_c(z)$ is a composite path weighting function (Ochs et al. 1976). The seven predetermined levels are line-of-sight distance from the instrument, so that actual height above ground depends on the zenith angle of the observed star. Some improvements to the NOAA scintillometer were made by AFGL (Air Force Geophysical Lab) to their instrument. They are described in more detail by Murphy and Battles (1986).

An NPS (Naval Postgraduate School) r_o scintillometer optically measures the transverse coherence length, r_o , of the image in the focal plane (Donald Walters, telephone conversation, October 1987). r_o is a scalar measure (in units of aperture size) of spatial wavefront coherence. Crudely stated, the resolution of an image cannot be improved by increasing a single aperture beyond r_o (Dewan 1980). This helps delineate the aperture size for adaptive optics elements. It has been shown that

$$r_o = 18.5 \lambda^{1.2} \left(\int_0^\infty C_n^2(z) dz \right)^{-3/5} \quad (2.4)$$

with r_o in cm, wavelength (λ) in m, C_n^2 in $m^{-2/3}$, and altitude in m. Using this integral, r_o can also be calculated from profiles of C_n^2 (Fried and Mevers 1974).

An AFWL (Air Force Weapons Lab) isoplanometer optically measures θ_o , the isoplanatic angle. θ_o is a measure of angular coherence for an object with angular size (vs. a point source) that delineates the region through which the object can be viewed coherently without adaptive optics (Loos and Hogge 1979; Murphy and Battles 1986). θ_o can also be calculated from a vertical profile of C_n^2 (Murphy and Battles 1986)

$$\theta_o = 58000 \lambda^{1.2} \left[\int_0^\infty z^{5/3} C_n^2(z) dz \right]^{-3/5} \quad (2.5)$$

with θ_o in μrad , and λ , z and C_n^2 in the same units as for r_o .

Notice that the three parameters discussed here have different propagation path weighting functions (σ_I^2 as $z^{5/6}$, r_o as 1.0, θ_o as $z^{5/3}$). Thus, for ground-to-space optical paths, r_o tends to be dominated by the boundary layer, θ_o by the stratosphere, and σ_I^2 is somewhere in between.

CHAPTER 3

MICROTURBULENCE THEORY

3.1 The Refractive Index Structure Function

The atmosphere is predominantly hydrostatically stable above the planetary boundary layer (PBL). Nevertheless, observations, such as contrails and rocket trails, have clearly shown that discreet turbulent layers exist (VanZandt et al. 1981). Although turbulence and byproducts of turbulence (fossil eddies) are undoubtedly present, they exist only on an intermittent basis.

While atmospheric turbulence is inherently anisotropic, at small size scales, where viscous dissipation occurs, turbulence can be considered isotropic. For isotropic and homogeneous turbulence, the structure function, D , depends on spatial scalar distance, ξ , and is defined as the mean squared difference of the measured passive parameter (e.g., temperature) at two points in space (Hinze 1975).

$$D_T(\xi) = \langle (T(r) - T(r+\xi))^2 \rangle \quad (3.1)$$

where the angle brackets indicate an averaged quantity. In anisotropic turbulence, D also depends on the orientation of the separation (Hinze 1975).

The autocorrelation R is defined as the average of the product of deviations from the mean (e.g., T') at two points in space.

$$R_T(\xi) = \langle T'(r) T'(r+\xi) \rangle \quad (3.2)$$

In the limit, as ξ approaches infinity, the structure function approaches twice the variance. Variance is equal to the

autocorrelation function at $\xi=0$ (Tatarskii 1971). Thus,

$$\frac{1}{2} D_T(\xi) = R_T(0) - R_T(\xi) \quad (3.3)$$

In the inertial subrange, it can be shown that the structure function has a power law relation to separation with a constant designated C_x^2 (e.g., C_T^2) (Hinze 1975).

$$D_T(\xi) = C_T^2 \xi^{2/3} \quad (3.4)$$

Similarly, we can define for refractive index,

$$D_n(\xi) = C_n^2 \xi^{2/3} \quad (3.5)$$

The structure constant is only a "constant" in that it is independent of the separation distance; it is still variable over time and space [e.g., $C_T^2(x,y,z,t)$]. The optical refractive index structure constant can be related to the temperature and humidity structure constants (Nastrom et al. 1981).

$$C_n^2 = f_1^2 C_q^2 + 2 f_1 f_2 C_{qT}^2 + f_2^2 C_T^2 \quad (3.6)$$

where $f_1 = 0.60 P/T^2$, and

$$f_2 = -1.2 P q / T^2 \theta - 77.6E-6 P / T \theta \quad (3.7)$$

with pressure in mb, and where q is specific humidity. Neglecting the effects of humidity, this reduces to (Tatarskii 1971)

$$C_n^2 (\text{optical}) = (79 \times 10^{-6} (P/T^2))^2 C_T^2 \quad (3.8)$$

During the EWAK experiment, the aircraft-measured C_T^2 allowed computation of "dry" C_n^2 -optical. A Lyman-alpha detector on the

aircraft was intended to measure C_q^2 but the threshold sensitivity was too high for the vapor concentrations at the altitudes of interest.

3.2 C_n^2 From Radar Measurements

Data from a clear-air radar (often referred to as a profiler) can be used to calculate C_n^2 -radar based on radar reflectivity. The backscatter cross section from received power, σ , at the wavelength, λ , can be characterized by C_n^2 (VanZandt et al. 1977) as

$$\sigma = 0.38 C_n^2 \lambda^{-1/3} \quad (3.9)$$

Tatarskii (1971) derives a dimensional relation for C_n^2 based on a refractivity gradient across a turbulent layer

$$C_n^2 = a M^2 L^{4/3} \quad (3.10)$$

where a is an empirical constant, L is the layer thickness and

$$M^2 = -77.6 \times 10^{-6} (P/T) [N/g(1 + 15500q/T) - 7750 q'/T] \quad (3.11)$$

where P is pressure in mb, T is absolute temperature, q is specific humidity in kg/kg, q' is $\partial q / \partial z$, g is acceleration due to gravity, and N is the Brunt-Vaisala frequency squared. For C_n^2 -optical, q and q' are set equal to zero in M^2 (Dewan 1980), which gives the resulting ratio relating optical and radar values

$$(C_n^2\text{- radar}) / (C_n^2\text{- optical}) = X^2 \quad (3.12)$$

with (Fairall and Thomson 1985)

$$X^2 = [1 - 7750 q' (q/T)(g/N) + 15500 q/T]^2 \quad (3.13)$$

3.3 C_T^2 and C_u^2 Relationships

Dimensional analysis shows that in the inertial subrange of isotropic turbulence, the variance spectral density obeys a $k^{-5/3}$ wavenumber dependence.

$$\phi_T(k_1) = \beta_T \chi_T \epsilon^{-1/3} k_1^{-5/3} \quad (3.14)$$

where β_T is an empirical constant, χ_T is the rate of dissipation of one half the temperature variance, ϵ is the dissipation rate of the turbulent kinetic energy, and k_1 is the spatial wavenumber ($k_1 = 2\pi \lambda^{-1}$) (Panofsky and Dutton 1984). Since the one dimensional variance spectrum is defined as the Fourier transform of the autocorrelation (Panofsky and Dutton 1984),

$$\phi_T(k_1) = \frac{2}{\pi} \int_0^\infty R_T(\xi_1) \cos(k_1 \xi_1) d\xi \quad (3.15)$$

it can be shown using the relation of the structure function to variance and the autocorrelation, that

$$\phi_T(k_1) = 0.25 C_T^2 k_1^{-5/3} \quad (3.16)$$

in which 0.25 is the result of combining several constants. Now, the so-called Corrsin relation is obtained from 3.14 and 3.16 (Tatarskii 1971).

$$C_T^2 = 4 \beta_T \chi_T \epsilon^{-1/3} \quad (3.17)$$

β has been determined for temperature, $\beta_T=0.8$, and velocity,

$\beta_u = 0.5$ (Champagne et al. 1977; Panofsky and Dutton 1984). β_q is assumed to be equal to β_T . Since $\chi_u = \epsilon$ for velocity, a simplified Corrsin relation is obtained

$$C_u^2 = 4 \beta_u \epsilon^{2/3} = 2 \epsilon^{2/3} \quad (3.18)$$

Using this relation, it is simple to calculate ϵ , the turbulent kinetic energy dissipation rate.

ϵ is an important term in the variance budget equations for a turbulent layer. These equations, neglecting transport (Ottersten 1969), are (Fairall and Markson 1984)

$$de/dt + \overline{u'w'} \partial u / \partial z - g/\theta \overline{w'\theta'} = -\epsilon \quad (3.19)$$

$$\frac{1}{2} \frac{d\sigma_\theta^2}{dt} + \overline{w'T'} \partial \theta / \partial z = -\chi_T = -C_T^2 \epsilon^{1/3} / (4 \beta_T) \quad (3.20)$$

where primed quantities are fluctuations, barred quantities are means, $e = 1/2(\sigma_u^2 + \sigma_v^2 + \sigma_w^2)$ is the turbulent kinetic energy, g is the acceleration due to gravity, z is altitude, σ_θ is variance of potential temperature, χ_T is the rate of dissipation of one half the thermal variance, and u , v , and w are the horizontal and vertical velocity components respectively. If the flux Richardson number is defined as

$$R_f = [(\overline{w'\theta'} g/\theta) / (\overline{u'w'} \partial u / \partial z)] \quad (3.21)$$

and the eddy diffusion coefficient is invoked

$$\overline{w'\theta'} = -K_H \partial \theta / \partial z \quad (3.22)$$

$$\overline{u'w'} = -K_m \partial u / \partial z \quad (3.23)$$

then the following ratio results when using the Corrsin relations in a ratio of equation 3.20 to 3.19. (Fairall and Markson 1984)

$$C_T^2 / C_u^2 = 1.6 (\theta/g) \partial\theta/\partial z R_f / (1 - R_f) \quad (3.24)$$

$$C_T^2 / C_u^2 = 1.6 (\theta/g) \partial\theta/\partial z R_i / (P_r - R_i) \quad (3.25)$$

where R_f is replaced by the gradient Richardson number,

$$R_i = g \partial \ln \theta / \partial z / (\partial u / \partial z)^2 \quad (3.26)$$

and the turbulent Prandtl number,

$$P_r = K_m / K_H \quad (3.27)$$

In an actively turbulent layer in the free troposphere,

$R_i \approx R_{icrit} = 0.25$ and $P_r \approx 1$ (Dewan 1980), then

$$C_T^2 / C_u^2 \approx 1.6 (\theta/g) \partial\theta/\partial z R_i \quad (3.28)$$

Gradient Richardson number is the basis for a model developed by VanZandt et al. (1978, 1981). This model predicts C_n^2 -optical and ϵ based on measured values of $N (=g/\theta \partial\theta/\partial z)$ and $S (= \partial u/\partial z^2 + \partial v/\partial z^2)$, and input values of L , the outer scale or overturning size of the turbulent eddies. Note that the gradient Richardson number is equal to N/S . Based on equation 3.28, this model can also be related to the ratio of C_T^2 and C_u^2 . The model is based on Tatarskii's dimensional relationships

$$C_n^2 = a M^2 L^{4/3} \quad (3.29)$$

$$\epsilon = b S^{3/2} L^2 \quad (3.30)$$

where a and b are constants. A statistical integration is performed assuming that turbulence occurs in discrete layers with $R_i \leq 0.25$. Theoretical probability density functions are assumed for shear and temperature gradients. The internal model variable L is adjusted to give best match to radar-derived C_n^2 profiles. The model is inherently based on averaging over a length much greater than the turbulent scale, of which only a fraction, F , is actively turbulent (VanZandt et al. 1981). Thus high resolution in situ measurements (such as measurements by aircraft) may differ from model predictions.

3.4 The Turbulent Kinetic Energy Dissipation Rate

Few in situ measurements of C_u^2 or ϵ have been made above the PBL. Barat and Bertin (1984) measured C_T^2 and C_u^2 with stratospheric balloons, and Fairall and Markson (1984) with an aircraft. Kennedy and Shapiro (1980) calculated various turbulence parameters from research aircraft observations of CAT episodes associated with jetstreams.

Substituting for C_u^2 in equation 3.22 gives another relationship for ϵ

$$C_T^2 = 3.2 (\theta/g) \partial\theta/\partial z R_i \epsilon^{2/3} \quad (3.31)$$

This can be used to calculate ϵ from C_T^2 measurements, and from high altitude (where water vapor contribution is negligible) profiler measurements of C_n^2 -optical (Tatarskii 1971) with

$$C_n^2 = [79 \times 10^{-6} P/T^2]^2 3.2 (\theta/g) \partial\theta/\partial z R_i \epsilon^{2/3} \quad (3.32)$$

or by assuming a Corrsin relation for C_n^2

$$C_n^2 = 3.2 \chi_n \epsilon^{-1/3} \quad (3.33)$$

and assuming

$$\chi_n = K_n (\partial n / \partial z)^2 \quad (3.34)$$

$$K_H = R_i N^{-1} \epsilon \quad (3.35)$$

$$K_n = K_H \quad (3.36)$$

$$M^2 = (\partial n / \partial z)^2 \quad (3.37)$$

then

$$C_n^2 = 3.2 R_i M^2 N^{-1} \epsilon^{2/3} \quad (3.38)$$

where N is Brunt-Vaisala frequency squared and M is Tatarskii's refractivity gradient (Barat and Bertin 1984, Panofsky and Dutton 1984). Notice that equation 3.28 implies the factor R_i should actually be $R_i / (P_r - R_i)$.

3.5 Turbulence Size Scales

For oceanic turbulence, Gregg (1987) defines a turbulence bandwidth based on the ratio of Ozmidov scale $L_o = [\epsilon / N^{3/2}]^{1/2}$ (a buoyancy scale at which buoyancy equals inertial force) and the Kolmogorov scale, $\eta = [\nu / \epsilon^3]^{1/4}$ (the inner scale or cutoff wavelength for the inertial subrange where viscous equal inertial forces).

$$L_o / \eta = [\epsilon / \nu N]^{3/4} \quad (3.39)$$

where ν is the kinematic viscosity. The eddy overturning scale is proportional to the buoyancy scale in actively turbulent layers. Thus, the inertial subrange occurs for size scales less than the buoyancy scale and greater than the inner scale. Gregg provides the following empirical guideline to interpret the bandwidth ratio parameter as a turbulence activity parameter.

Value of $\epsilon/\nu N$	Turbulence State
<15	Decaying turbulence, fluxes negligible
>200	Fully isotropic
>10000	Fully developed flow

A spectrum begins to deviate from -5/3 slope at size scales one order of magnitude greater than the Kolmogorov microscale (Hill and Clifford 1978). For $L_0 \approx 10\eta$, no inertial subrange should be apparent.

CHAPTER 4

THE EWAK EXPERIMENT

4.1 Overview

Two segments of the EWAK experiment were analyzed in this thesis study. The first and major segment was performed from 14 April 1986 to 6 May 1986. This segment was conducted at the Meteorological Field Site, located several miles southwest of State College, PA, on the Rock Springs Agronomy Research Farm. The relevant instruments operating at various times during the experiment were an Air Force Geophysical Lab (AFGL) scintillometer, Rome Air Development Center (RADC) scintillometer, an AFGL thermosonde, an Air Force Weapons Lab (AFWL) isoplanometer, a Naval Postgraduate School (NPS) r_o scintillometer, a Penn State University (PSU) Doppler radar profiler, a PSU Doppler sodar, and the Airborne Research Associates (ARA) aircraft. A summary of the database relevant to this study is given in Table 1.

The aircraft was based at University Park Airport, several miles northwest of State College, PA. Data gathering flights were made over the field site and insofar as possible within a radius of 10 miles. Eight flights were made, six yielded useable results: flight 1 was a test flight and flight 5 had a total failure of the instrument recorder. Each flight consisted of a fairly rapid climb to maximum altitude (approximately 30 kft or 10 km) and then a slow descent (500 fpm). All descents were analyzed (because of the greater resolution), but for comparison purposes several ascents were also analyzed. Level

Table 1.
Aircraft flight logistics and corresponding data from other
instruments during EWAK.

Aircraft Flight	Site	Date	Type	GMT Time	Radar Wind Observe Time	Thermosonde Flight Time	Scintillimeter Run Time	Radar C _n ² Observe Time
1	PSU	4/13/86	test flight					
2	PSU	4/14/86	Descent Level	1534-1554 1611-1732	1500-1600			1600-1700
3	PSU	4/18/86	Descent	2107-2207	2000-2100			2100-2200
4	PSU	4/19/86	Descent	1710-1809	1700-1800			1600-1700
5	PSU	5/3/86	recording failure					
6	PSU	5/4/86	Ascent Descent	0400-0438 0439-0540	0500-0600	L4033	0342-0513	0500-0600
7I	PSU	5/4/86	Descent	1725-1822	1700-1800			1800-1900
8	PSU	5/6/86	Ascent Descent	0259-0331 0332-0430	0300-0400	L4019	0317-0420	0300-0400
9	RADC	8/11/86	Ascent Descent	2247-2324 2325-2357				
10	RADC	8/12/86	Ascent Descent	1557-1706 1707-1751				
11I	RADC	8/13/86	Ascent Descent	0219-0300 0301-0357				
11II	RADC	8/13/86	Level	1410-1452				
12	RADC	10/10/86	Level Descent	1738-1825 1911-1943				

flight data of return trips by the aircraft to Boston was also added to several flights.

The second segment of EWAK was conducted at Griffiss Air Force Base, Rome, NY, from 11 August through 15 August 1986. Both ARA aircraft and RADC scintillometer measurements were taken, however, scintillometer data taken during these flights was unavailable for this thesis. One additional flight was made on 20 October 1986. For these flights, the aircraft was based at Oneida County Airport and performed similar flight patterns centered around RADC's field site in Verona, NY.

4.2 Aircraft Instrumentation

A summary of the instrumentation available on the aircraft is given by Fairall and Markson (1984; 1987). Thus only the relevant turbulence measurements are discussed here. Temperature and velocity signals were amplified, filtered, and recorded on FM tape. Recorder gain settings were correlated to tape counters and recorded manually. Filters were set for a bandpass between 2 and 200 Hz for the temperature signal, and 5 and 200 Hz for the velocity signal. The FM tape recorder was set at the 15/16 ips speed, which provided an additional low pass filtering at 256 Hz.

Temperature fluctuations were measured with a fast response resistance bridge driving microthermal sensor probes as the temperature sensitive resistance elements. The bridge used was a Thermo Systems, Inc. (TSI) type 1044, dc Wheatstone bridge with a frequency response of 800 hz. The microthermal probes were TSI type 1210 with T1.5 configuration (W wire, 4.5 μ m dia., ice point resistance

$R_i \sim 5\Omega$). A wingtip boom carried matched sensors that were connected to the two bridge arms. One sensor was covered so that bridge signal output was proportional to temperature fluctuations sensed by the exposed probe.

Velocity fluctuations were measured with hot-wire anemometry in a constant temperature circuit. The bridge used was a TSI model 1050. Probes used were the same TSI type 1210 T1.5 tungsten sensors with a 50% overheat.

Other measurements taken that were used in this analysis were air temperature (measured with a standard Rosemont sensor and bridge circuit), dew-point temperature (measured with a Cambridge Systems, Inc. aircraft chilled mirror instrument), pressure altitude (measured with a Rosemont sensor), and radar altitude (measured with a Bonzair Mark 10 altimeter).

4.3 Additional Instrumentation

Both the RADC and the AFGL scintillometers are instruments that measure stellar scintillation amplitude fluctuations based on the NOAA model II instrument described in detail by Ochs et al. (1977). Additional modifications were made to the AFGL scintillometer as described by Murphy and Battles (1986). The AFWL isoplanometer and NPS r_0 scintillometer are instruments also based on measuring stellar scintillations and may be regarded to be derivatives of the NOAA instrument. These instruments are described in some detail by Eaton et al. (1985), and Stevens (1985), respectively.

The AFGL thermosonde is essentially a special temperature turbulence measuring package attached to a radiosonde. The instrument package is described in detail by Brown et al. (1982).

Penn State's Doppler radar profiler is, basically, of the type described by Strauch et al. (1986). It is a VHF (6 m wavelength) pulsed Doppler radar with a phased array antenna located near McAlevys Fort, PA, on Shantytown Road, approximately 10 miles south of State College, PA. With the profiler, vertical profiles of wind speed and direction are obtained as well as radar reflectivity (backscatter cross section). Radar volume reflectivity can be used to calculate C_n^2 values at each of the radar gates (VanZandt et al. 1978). The profiler produces both high and low resolution profiles. High resolution is ~290 m from ~1 km to 8 km MSL. Low resolution is ~870 m from ~1.5 km to 17.5 km MSL.

PSU Doppler sodar data was not used in this study.

CHAPTER 5

DATA PROCESSING

The relation of the structure constant to the variance spectral density as a function of wavenumber (Equation 3.16) allows determination of C_T^2 and C_u^2 from spectral analysis of turbulence data. The aircraft data was a time series record of voltage fluctuations, which could be transformed into frequency spectra. Taylor's frozen turbulence hypothesis allows for translation of the spatial spectrum $\phi(k_1)$ to a frequency spectrum $\phi'(f)$ (Panofsky and Dutton 1984), by the relation

$$k_1 = 2\pi f/u \quad (5.1)$$

where k_1 is the spatial wavenumber, u is the relative speed of the passing eddies (in this case, $u=60$ m/s, the aircraft speed), and f is the frequency in Hz. Since total spectral intensity must be invariant (Panofsky and Dutton 1984), temporal and spatial spectra can be related by

$$\phi(k_1)dk_1 = \phi'(f)df \quad (5.2)$$

Substitution gives

$$\phi'(f) = \phi(2\pi f/u)dk_1/df = \phi(2\pi f/u) 2\pi/u \quad (5.3)$$

and then

$$\phi_T'(f) = 2\pi/u \phi_T(k_1) \quad (5.4)$$

$$\phi_T'(f) = 2\pi/u (0.25 C_T^2 k_1^{-5/3}) \quad (5.5)$$

$$\phi'_T(f) = (2\pi/u)^{-2/3} (0.25 C_T^2 f^{-5/3}) \quad (5.6)$$

Similarly for velocity

$$\phi'_u(f) = (2\pi/u)^{-2/3} (0.25 C_u^2 f^{-5/3}) \quad (5.7)$$

Rearranging gives the equation(s) relating the structure functions to the measured spectra

$$C_{T,u}^2 = 4 (2\pi/u)^{2/3} \phi'_{T,u}(f) f^{5/3} \quad (5.8)$$

where $\phi'_{T,u}(f)$ is a representative value in the inertial subrange (Fairall and Markson 1984).

Another method to determine the structure constants (the single probe RMS method) is suggested by the relation of total variance to spectral density (Fairall and Markson 1984)

$$\text{Variance} = \text{mean square} = \int_{f_1}^{f_u} \phi'(f) df \quad (5.9)$$

where f_u =upper frequency limit, and f_1 =lower frequency limit.

Thus the filtered RMS of the signal can be used to directly obtain the structure constant by integrating 5.6 or 5.7

$$\text{Variance} = (\text{RMS})^2 = (2\pi/u)^{-2/3} 0.25 C_{T,u}^2 \left(-\frac{3}{2}\right) (f_u^{-2/3} - f_1^{-2/3}) \quad (5.10)$$

Rearranging gives

$$C_{T,u}^2 = \frac{8}{3} (2\pi/u)^{2/3} (\text{RMS})^2 (f_1^{-2/3} - f_u^{-2/3})^{-1} \quad (5.11)$$

The thermosonde instrument calculated C_T^2 directly using the double probe RMS method. If two probes with a known separation ξ are used, then with an RMS of the difference of the signal

(Brown et al. 1982)

$$C_T^2 = \langle (T_1 - T_2)^2 \rangle / \xi^{2/3} = (\text{RMS})^2 / \xi^{2/3} \quad (5.12)$$

The spectral method has the advantage of greater accuracy over the RMS method because a region of the spectrum can be selected which is relatively free of noise. The RMS variance includes all noise in the bandwidth analyzed (Fairall and Markson 1984). However, the disadvantage to the spectral method is the greatly increased computation time. RMS methods can be done on a virtually real time basis.

The aircraft temperature turbulence data was taken as voltage fluctuations in bridge output due to resistance fluctuations of the probes. Temperature fluctuations cause these resistance changes. This relation is given by

$$dV/dt = i G_B dR/dt \quad (5.13)$$

where the current to the probe sensor is i , and bridge amplification or gain is $G_B (=4000)$ (Fairall and Markson 1984).

The resistance-temperature relation is linear for tungsten sensors over a broad temperature range, giving

$$R = R_i [1 + \alpha(T - T_i)] \quad (5.14)$$

where R_i and T_i are values at the ice point ($R_i=5\Omega$), and α is the effective thermal resistance coefficient ($\alpha=.0026 \text{ K}^{-1}$), which includes the loss of sensitivity due to probe support effects (Fairall and Markson 1984). Thus,

$$dR/dt = R_i \alpha dT/dt \quad (5.15)$$

and

$$dV/dt = i G_B G (R_i \alpha dT/dt) \quad (5.16)$$

where the added G term accounts for any additional signal conditioning or gains applied (usually $G=10$). The voltage variance spectrum is the Fourier transform of the square of voltage fluctuations which then can be related to the temperature variance spectrum (Fairall and Markson 1984),

$$\phi'_V = (i G G_B R_i \alpha)^2 \phi'_T(f) \quad (5.17)$$

Including noise sources, this would be

$$\phi'_V = (i G G_B R_i \alpha)^2 (\phi'_T + N_u + N_T + N_v / (i R_i \alpha)^2) \quad (5.18)$$

where N_v is broadband voltage noise in the system, N_T is temperature noise detected by the sensors but not due to turbulence (e.g., sonic adiabatic compression), and N_u is velocity contamination due to cooling rate variations associated with velocity fluctuations. An indepth study of signal-to-noise ratio was done by Fairall and Markson (1984). It was concluded that, in flight, most noise was temperature noise. Although the source of this noise could not be identified, it could be lessened by changing sensor location. Optimal sensor location proved to be on the wingtip. Sensor currents were kept at a maximum just below the velocity contamination threshold ($i=5$ mA).

Velocity turbulence data was also taken as a time series of voltage fluctuations. King's Law voltage relationship (Hinze 1975) was used

$$V^2 = V_o^2 + B u^{1/2} \quad (5.19)$$

where V_o^2 and B are calibration constants (Fairall and Schacher 1977) computed for 50% overhear at STP as $V_o^2 = 2.7 \text{ Volts}^2$ and $B_o = 1.0 \text{ Volts}^2 / (\text{ms}^{-1})^{1/2}$. Correcting for varying temperature and pressure gives

$$B = B_o (P/1013)^{1/2} (288/T)^{1/4} [(453-T)/288] \quad (5.20)$$

(Fairall and Markson 1984). Velocity fluctuations cause bridge output voltage variations as

$$dV/dt = [B G / (4 V u^{1/2})] du/dt \quad (5.21)$$

with G additional signal conditioning gains (usually $G=100$) and V the mean bridge voltage (about 3 Volts for nominal aircraft speeds).

Relating the square of fluctuations to the variance spectrum gives

$$\phi'_V = (B G / 4 V \sqrt{u})^2 \phi'_u \quad (5.22)$$

The final forms used for calculating C_T^2 and C_u^2 from the aircraft data (Fairall and Markson 1984) were

$$C_T^2 = 4 (2\pi/u)^{2/3} (i G G_B R_i \alpha)^{-2} \phi'_{V(T)}(f) f^{5/3} \quad (5.23)$$

$$C_u^2 = 4 (2\pi)^{2/3} u^{1/3} (4 V / B G)^2 \phi'_{V(u)}(f) f^{5/3} \quad (5.24)$$

Flight 12 gain settings were not recorded. They were assumed to be the same as flight 11 for processing, but for that flight, this should be noted.

Initially, the temperature and velocity channels of the taped data were converted from analog to digital with an Infotek A/D board. Approximately two minutes of analog data were digitized. A 128 point Fast Fourier Transform (FFT) was done and a final spectrum produced from an average of 400 spectral blocks. This gave a vertical resolution of 0.3 to 0.5 km, about the same as the radar profile.

The log of power spectral density (Volts^2/Hz) was plotted as decibels [$10 \cdot \log (V^2/\text{Hz})$] against log of frequency (Hz) for 4 to 256 Hz. A key frequency was chosen that consistently appeared in the inertial subrange (in a region of high signal to noise) and the spectral density at this point was used to plot a $-5/3$ slope through the spectrum to show goodness-of-fit to the Kolmogorov turbulence theory. Due to the small number of points, the spectra obtained with this method were somewhat crude and very difficult to interpret. Figure 1 shows three different spectra from flight 2 as examples (indicated as EWAK2BT-rec#). Record 1 has a high signal-to-noise ratio, record 31 is very noisy with little signal, and record 45 is an unusual steeply sloped spectra.

A second method gave far more satisfactory results. Roughly two minutes of data were analyzed by a dual channel Hewlett-Packard 3562A dynamic signal analyzer by linearly averaging 55 times with an overlap of 75%. A 1600 point FFT, using a Hanning window, produced a power spectrum from .125 to 100 Hz. This frequency range corresponds to a wavenumber range of 0.01 to 10 m^{-1} . Resolution of the spectra was greatly increased. The same three records from flight 2 are shown in Figure 2.

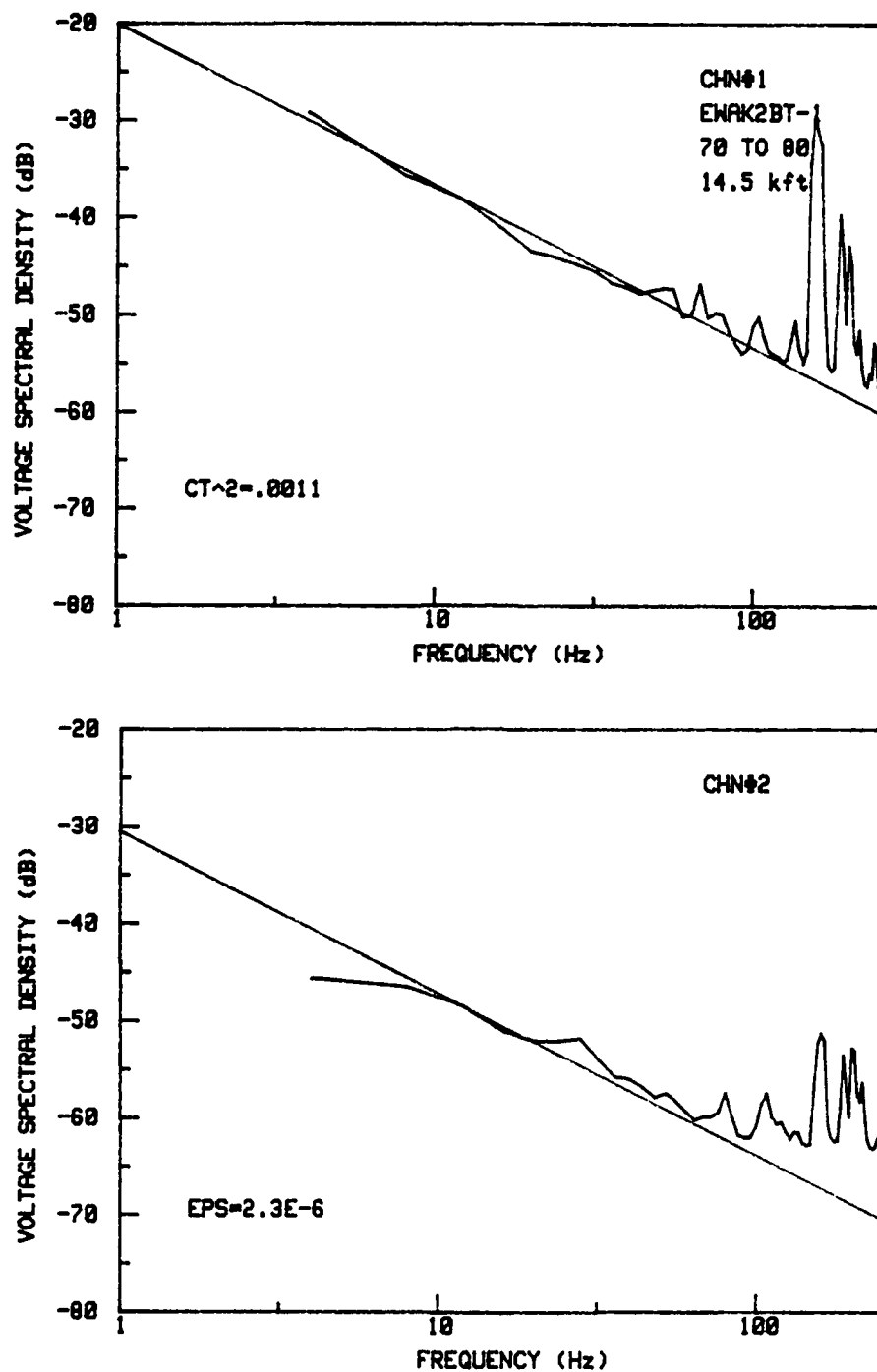


Figure 1. Voltage variance spectra from first FFT program (128 points). For each record, the top spectrum (channel #1) is temperature variance and the bottom spectrum (channel #2) is velocity variance. Voltage power spectral density (dB) is plotted against frequency (log Hz). The slanted line represents a $-5/3$ slope for comparison. Coded flight name (e.g., EWAK2BT) and record number (e.g., - 1), tape footage, and altitude are shown interior to each channel #1 graph. Three different dual-channel records in flight 2 are shown: 1, 31, and 45.

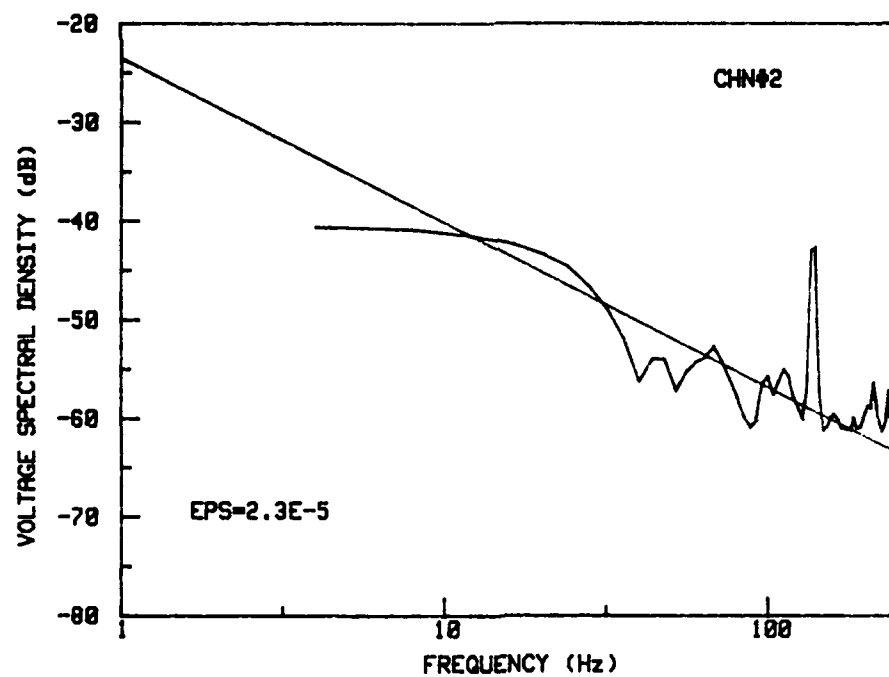
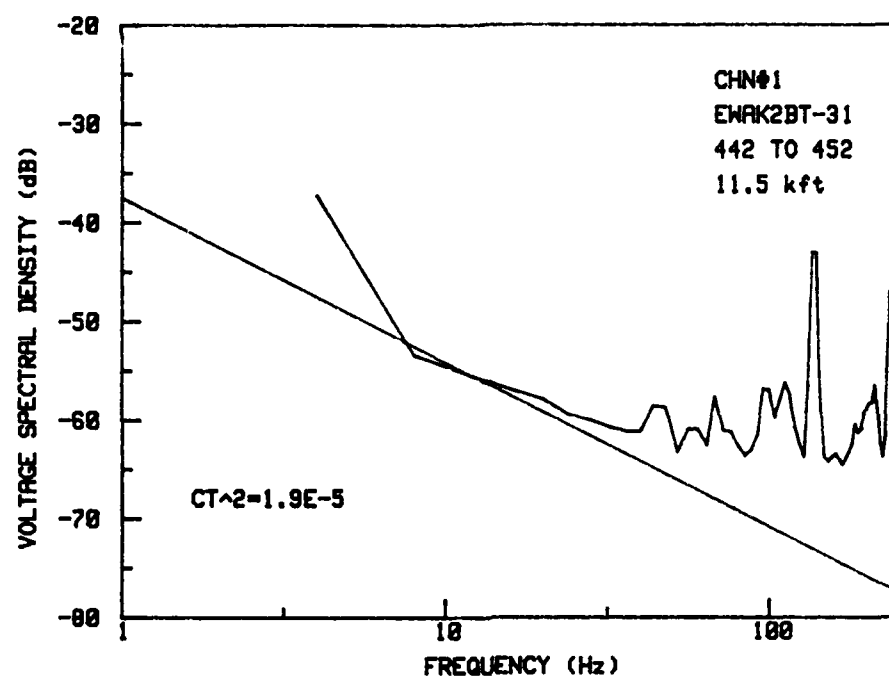


Figure 1. (continued)

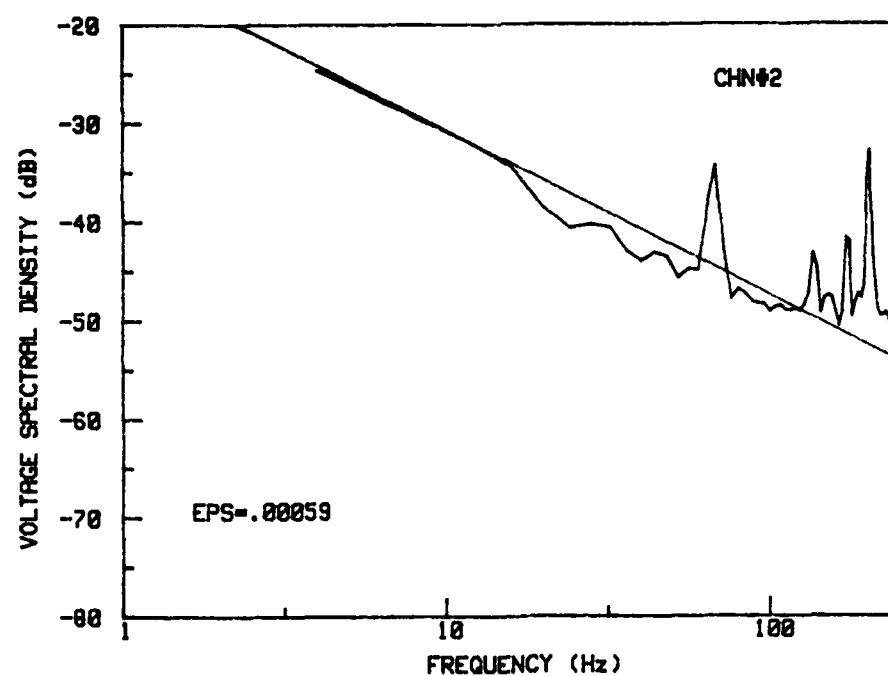
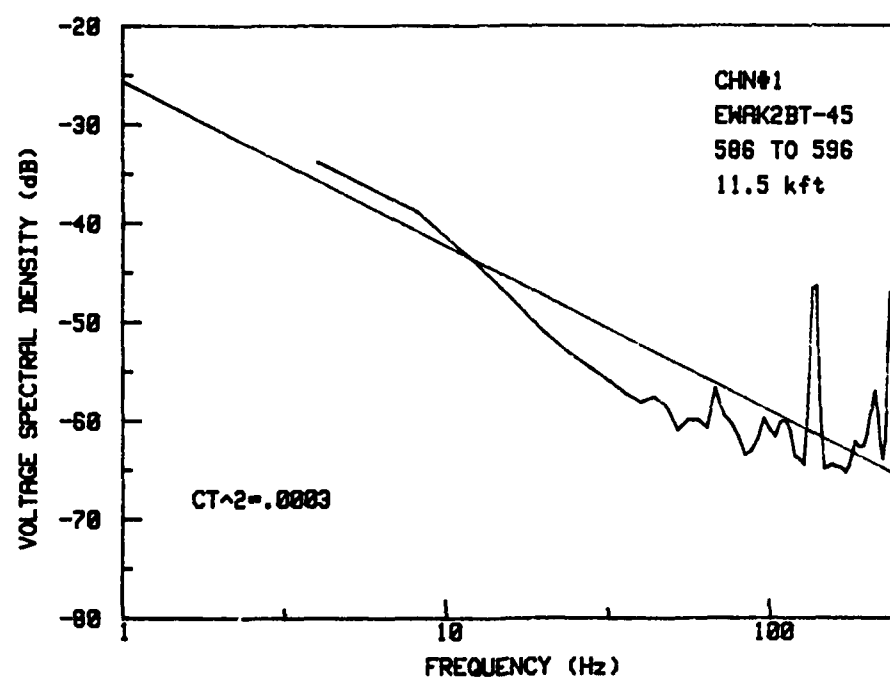


Figure 1. (continued)

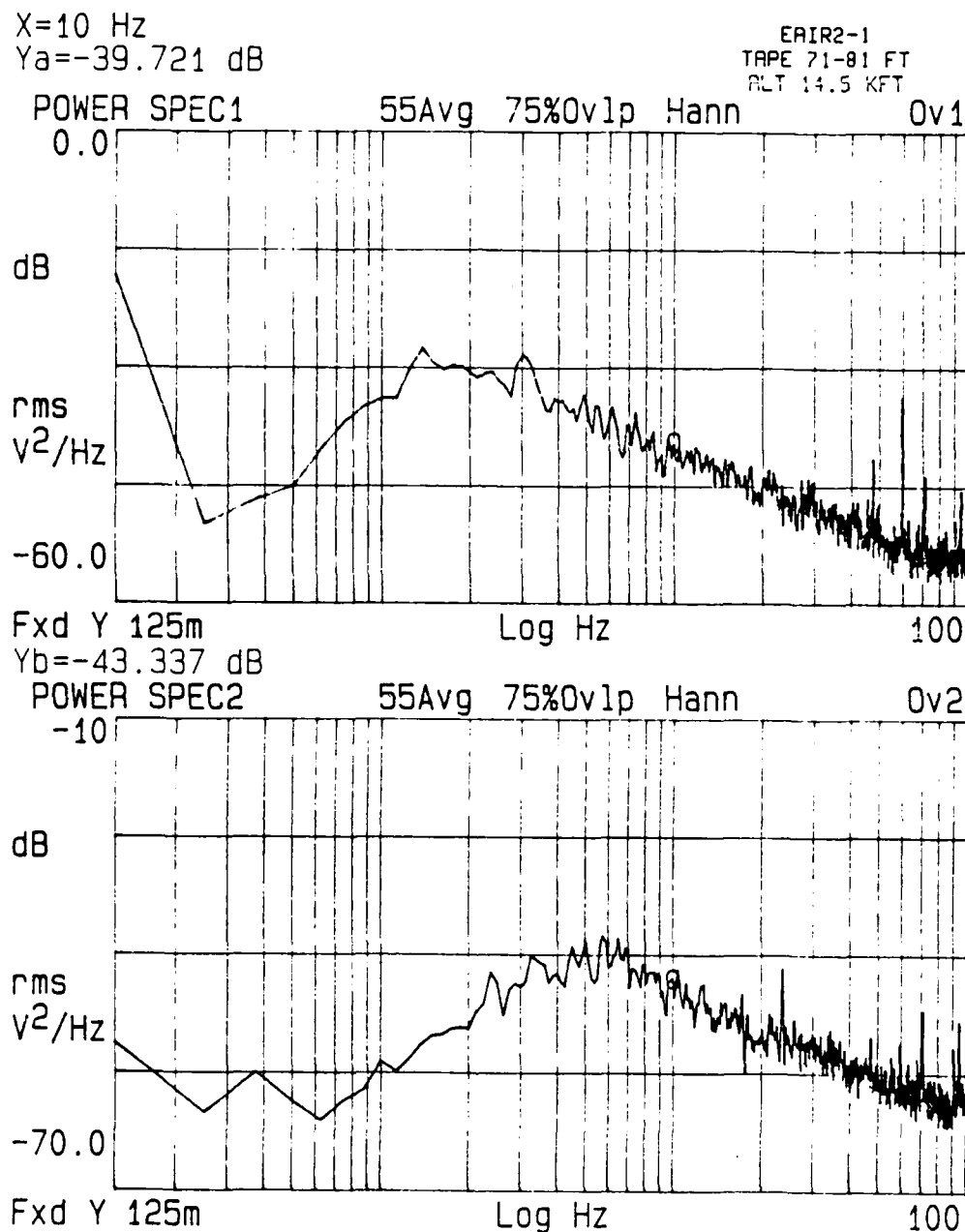
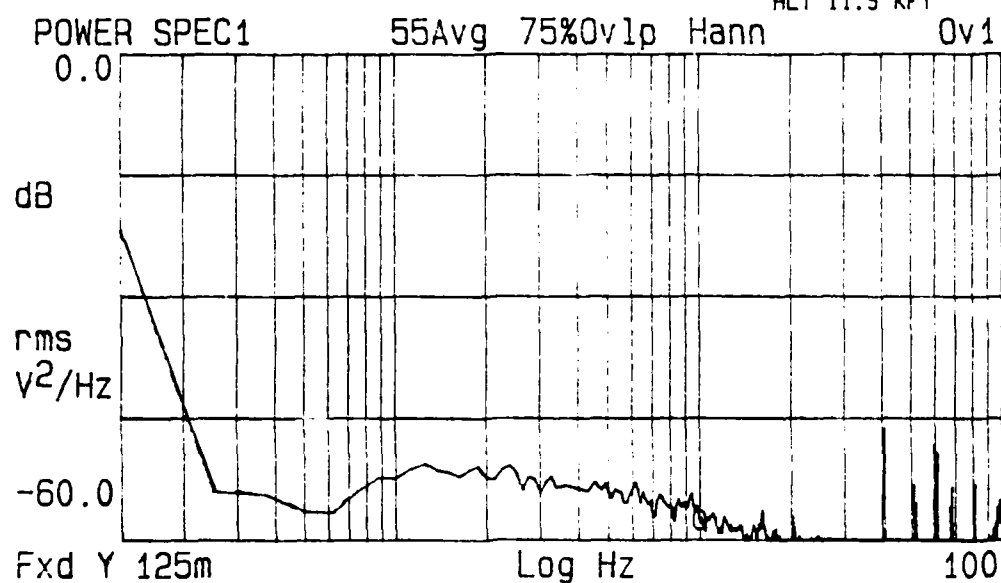


Figure 2. Voltage variance spectra produced by the signal analyzer's 1600 point FFT. For each record, Ov1 (top) is temperature variance and Ov2 (bottom) is velocity variance. Voltage power spectral density (dB) is plotted against frequency (log Hz). Processing parameters are stated above each spectrum. Coordinates of the cursor are given in the upper left corner of each spectrum. Vertical axis range has been fixed as stated in the lower left of each spectrum. Coded flight name (e.g., EAIR) and record number (e.g., - 1), tape footage, and altitude are annotated above each Ov1 graph. The same three dual-channel records in flight 2 are shown as in Figure 1.

X=10 Hz
Ya=-57.921 dB

EAIR2-31
TAPE 436-445 FT
ALT 11.5 KFT



Fxd Y 125m
Yb=-59.043 dB

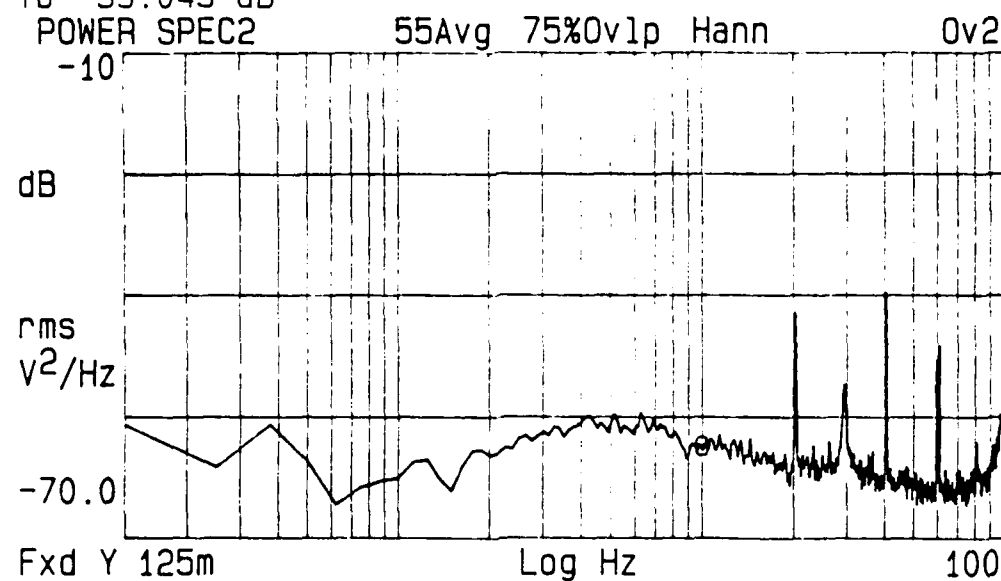
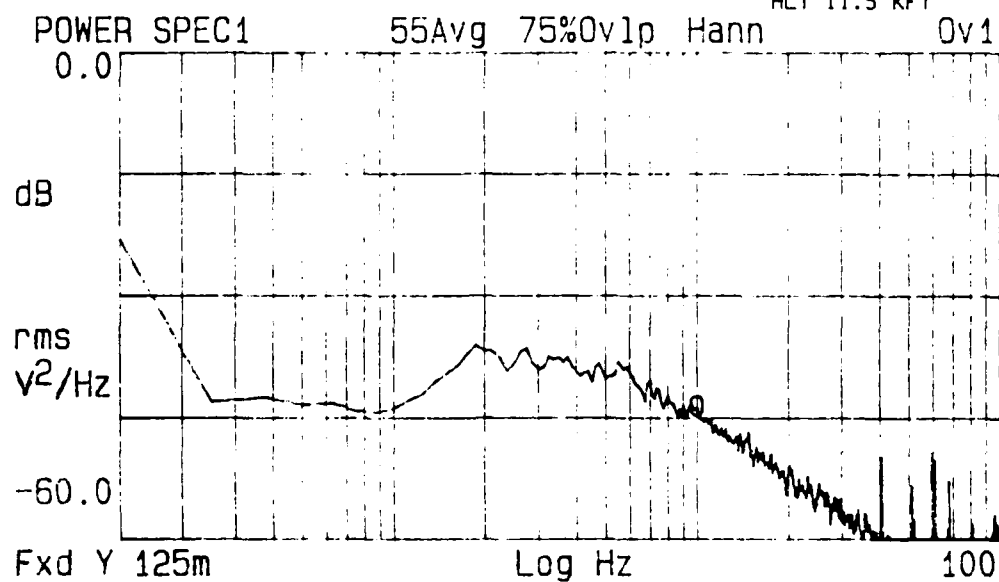


Figure 2. (continued)

X=10 Hz
Ya=-43.891 dB

EAIR2-45
TAPE 573-583 FT
ALT 11.5 KFT



Fxd Y 125m
Yb=-51.657 dB

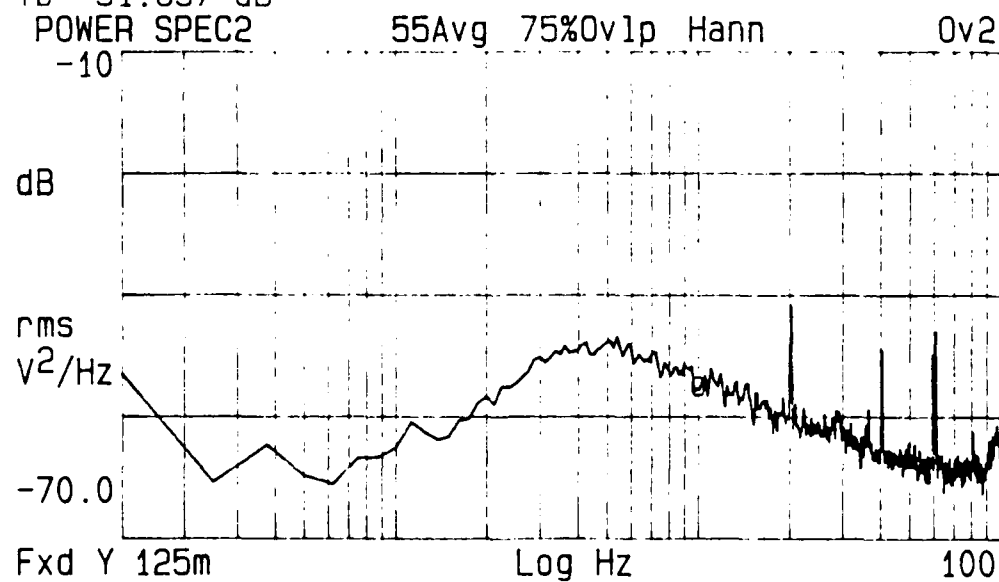


Figure 2. (continued)

CHAPTER 6

ANALYSIS METHODS

6.1 Aircraft Turbulence Data Analysis

An indepth analysis on aircraft instrumentation/experimental error was done by Fairall and Markson (1984). Uncertainty due to measurement error will therefore not be discussed here. However, for this thesis, much effort was put into detailed analysis of the aircraft turbulence data in attempts to improve analysis precision. These processes are described in this chapter.

To quantify goodness-of-fit, a linear regression analysis was performed on the log-log spectral data and percent error was calculated for deviation from $-5/3$ slope. Most spectra exhibited the $-5/3$ dependence out to the broadband noise level of the instruments, $\approx 3 \times 10^{-7} \text{ K}^2_{\text{m}}$ for temperature and $\approx 1 \times 10^{-6} (\text{m/s})^2_{\text{m}}$ for velocity (Fairall and Markson 1985). Because of this background noise level, notable in the high frequency range (over 20 Hz), it was determined that the best fit would be obtained at the lowest frequency possible within the inertial subrange. Unfortunately, the temperature data had been low pass filtered at 2 Hz and the velocity data at 5 Hz. Filters of the type used on the aircraft (Thermo Systems, Inc. model 1057 signal conditioner with TSI model 1051-2 monitor and power supply) were analyzed with white noise input on the signal analyzer. Then a power spectrum ratio of unfiltered noise to filtered noise was calculated (Figures 3a and 3b). This function could then be multiplied point by point to essentially "defilter" the data.

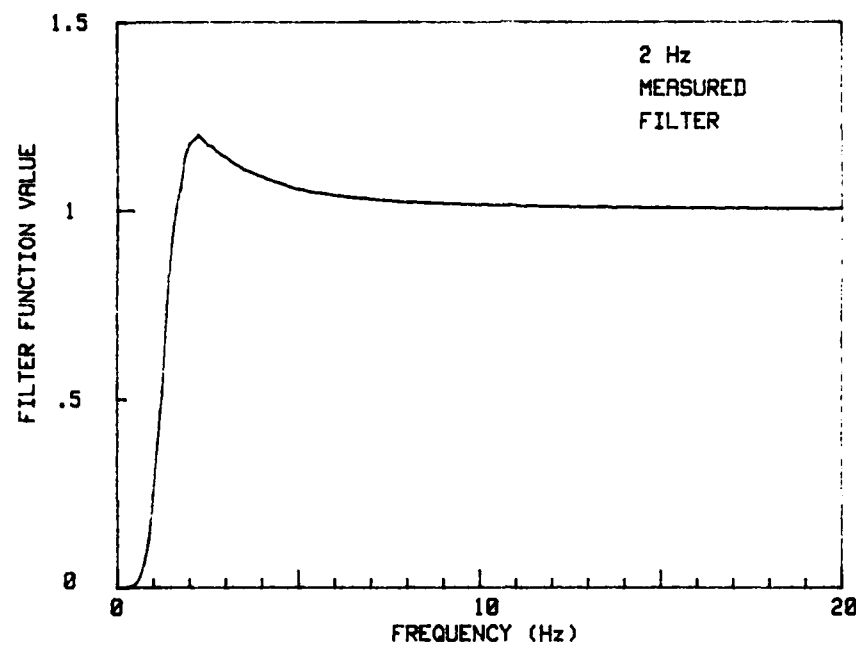


Figure 3a. The measured 2 Hz high pass temperature turbulence channel filter.

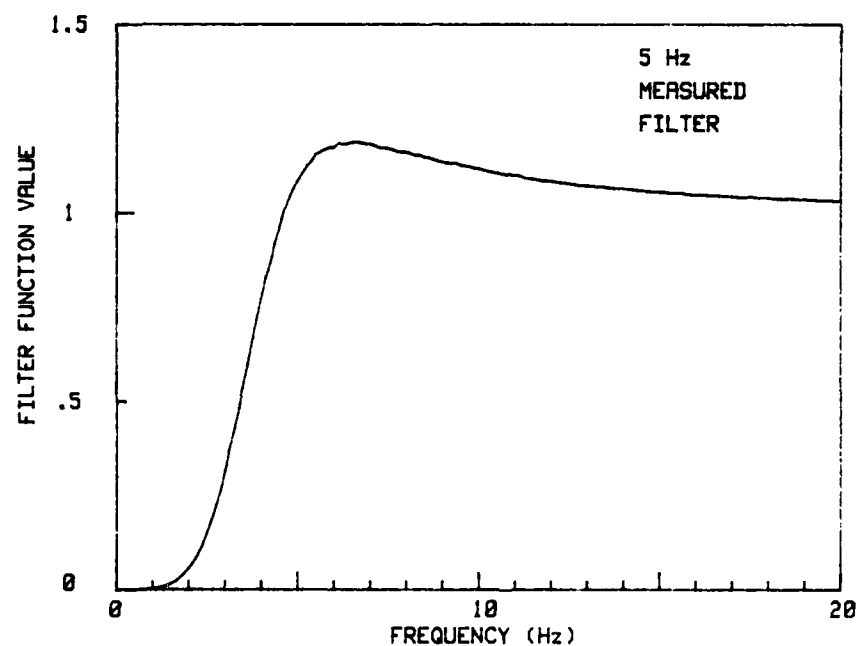


Figure 3b. The measured 5 Hz high pass velocity turbulence channel filter.

Spectral drop-off was still noted in the low frequency end (<1 Hz) of the spectra after this filter function was applied. Several reasons for this drop-off were proposed: a real phenomenon (i.e., the outer scale of the inertial subrange or the production size of the turbulence), a non-linear characteristic of the filter when the signal is log-distributed and not linearly distributed like the white noise, or individual error in the filter (two identical filters were tested and found to have different signatures). Assuming f is 1 Hz and u is 60 m/s, the frozen turbulence theory ($\lambda^{-1} = 2\pi f/u$) gives λ of 10 m as the production scale. For the altitudes flown, this is within an order of magnitude of typical estimates (VanZandt et al. 1981; Gregg 1987; Barat and Bertin 1984). For comparison to the characteristics of the measured filter function, an atmospheric filter function was derived to compensate for non-linear filter effects and any unknown atmospheric effects (e.g., variable production size scale). Several sample spectra from the boundary layer with exceptionally high signal-to-noise ratio and $-5/3$ slope were used to derive a function based on $-5/3$ slope (Figures 4a and 4b).

All spectra were then run through a three pass progressive editing program. If the percent error on a regression fit from 5 to 18 Hz was greater than 20%, the spectrum was rejected on pass 1. Figure 5a again shows records 1, 31, and 45 of flight 2 for pass 1. On the second pass, the atmospheric filter was used to defilter the data from 0.1 to 5.6 Hz (the cutoff frequency where both 2 and 5 Hz filters were approximately equal to one). Figure 5b shows the same three records for pass 2. If percent error was greater than 15% on a second regression fit from 2 to 18 Hz, then the spectrum was run

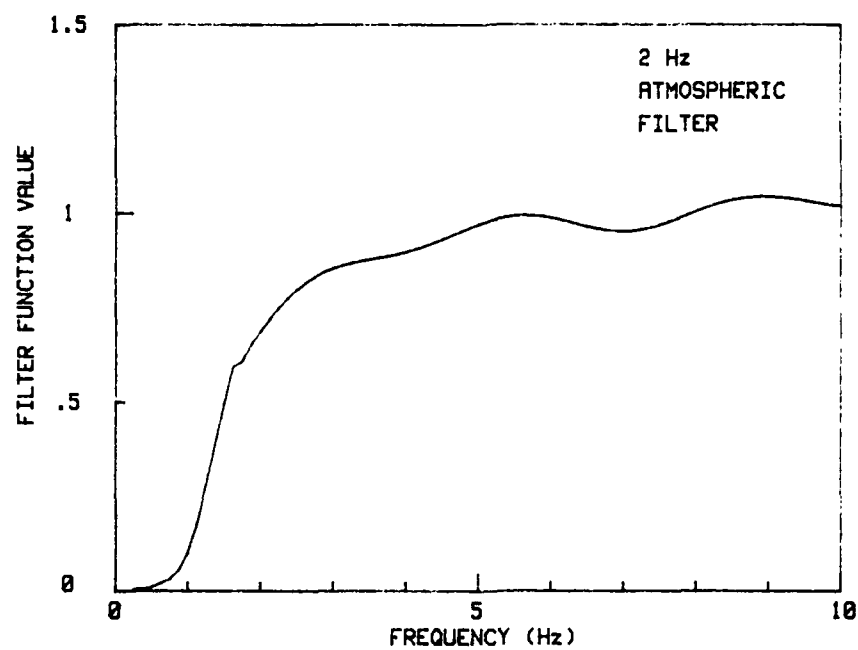


Figure 4a. The derived atmospheric 2 Hz high pass temperature turbulence channel filter.

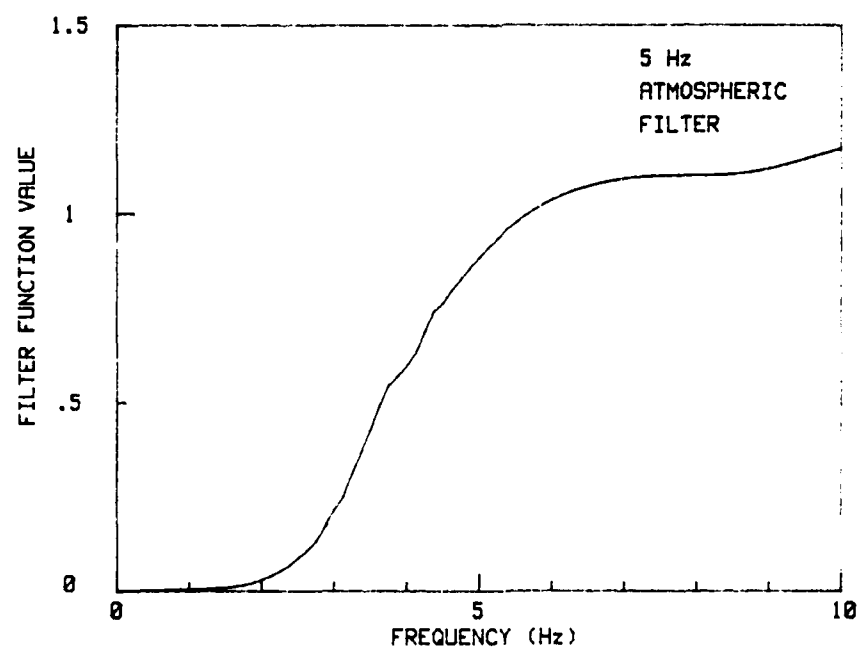


Figure 4b. The derived atmospheric 5 Hz high pass velocity turbulence channel filter.

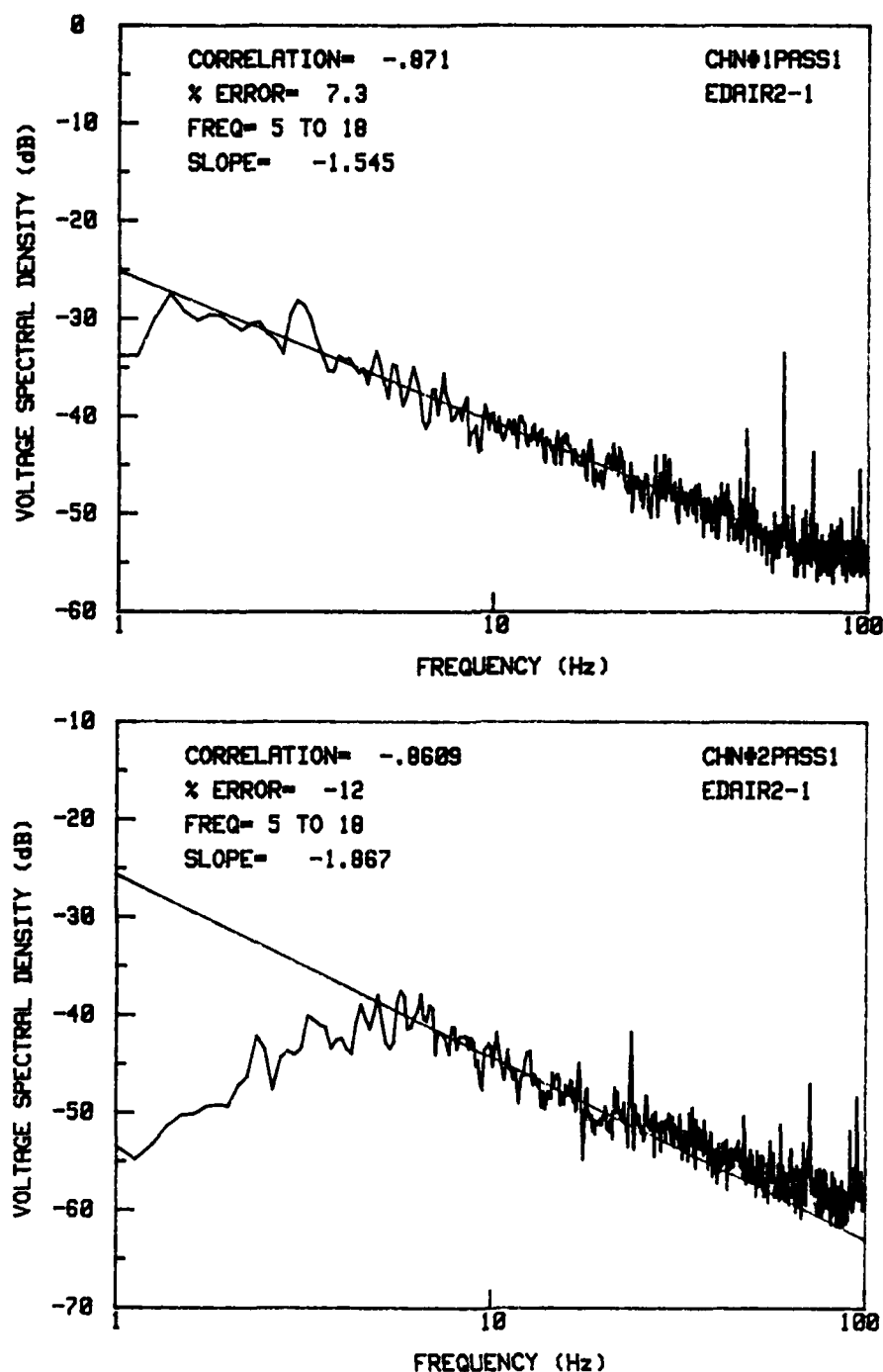


Figure 5a. Voltage variance spectra showing editing procedure. These spectra are filtered spectra derived from the taped data. This represents editing pass 1. Voltage power spectral density (dB) is plotted against frequency (log Hz). For each record, channel 1 (top) is temperature variance and channel 2 (bottom) is velocity variance. Channel number, pass number, and coded flight name and record number are shown interior to each graph. The slanted line represents the regression fit. Regression slope, correlation coefficient, and percent error are given in the upper left corner of each spectrum. The same three dual-channel records in flight 2 are shown as in Figure 1.

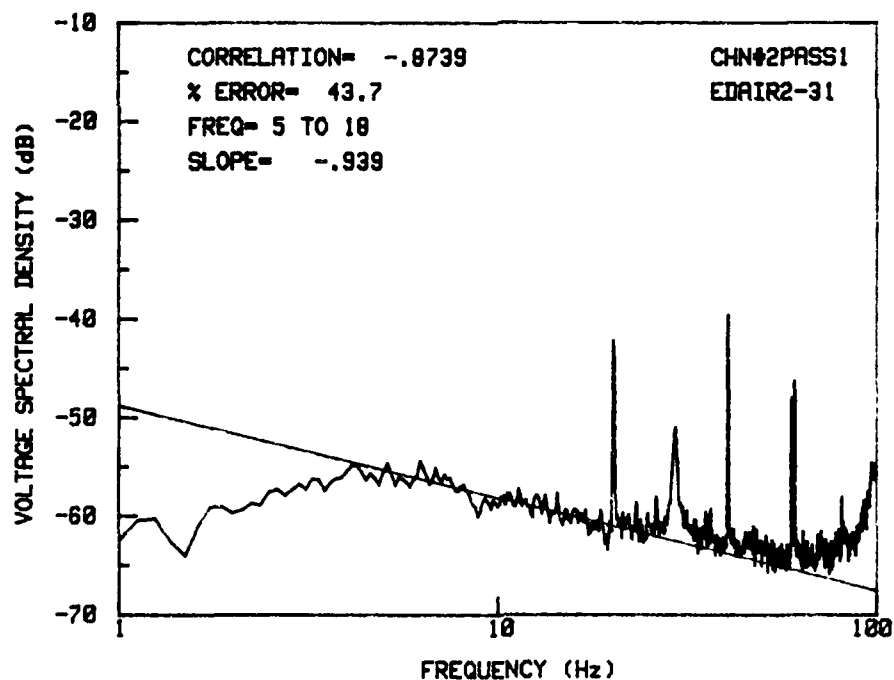
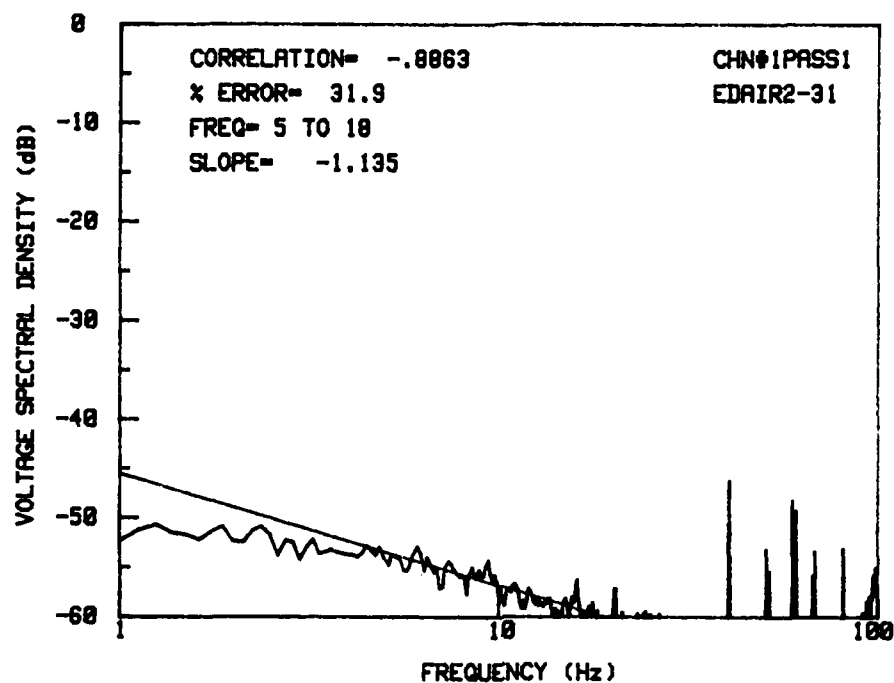


Figure 5a. (continued)

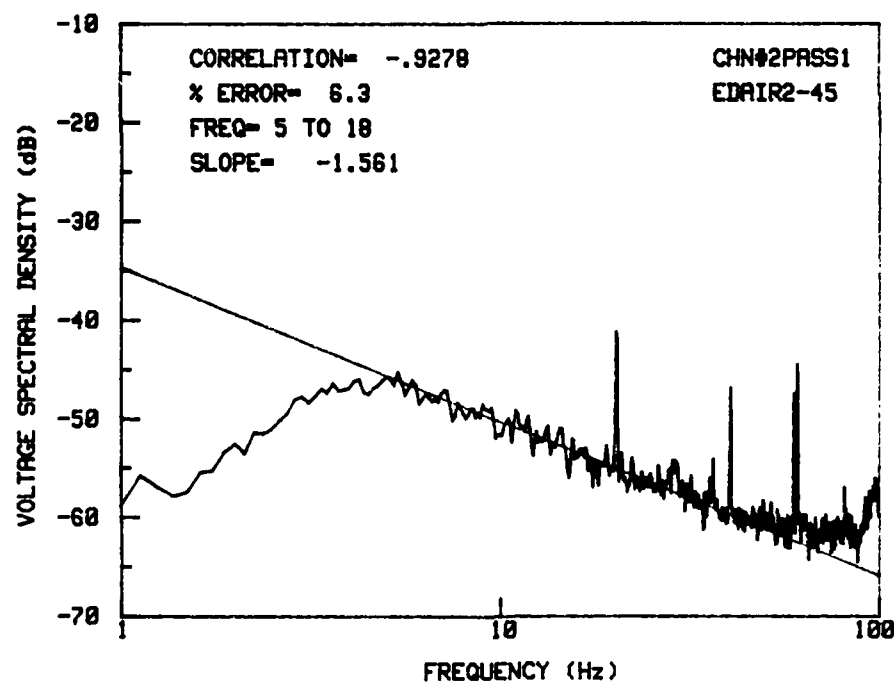
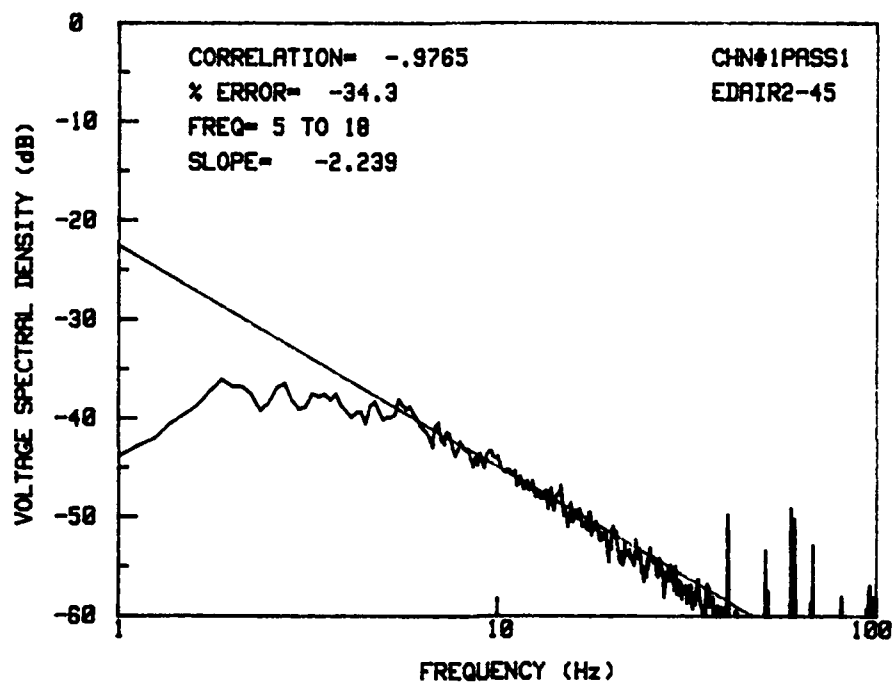


Figure 5a. (continued)

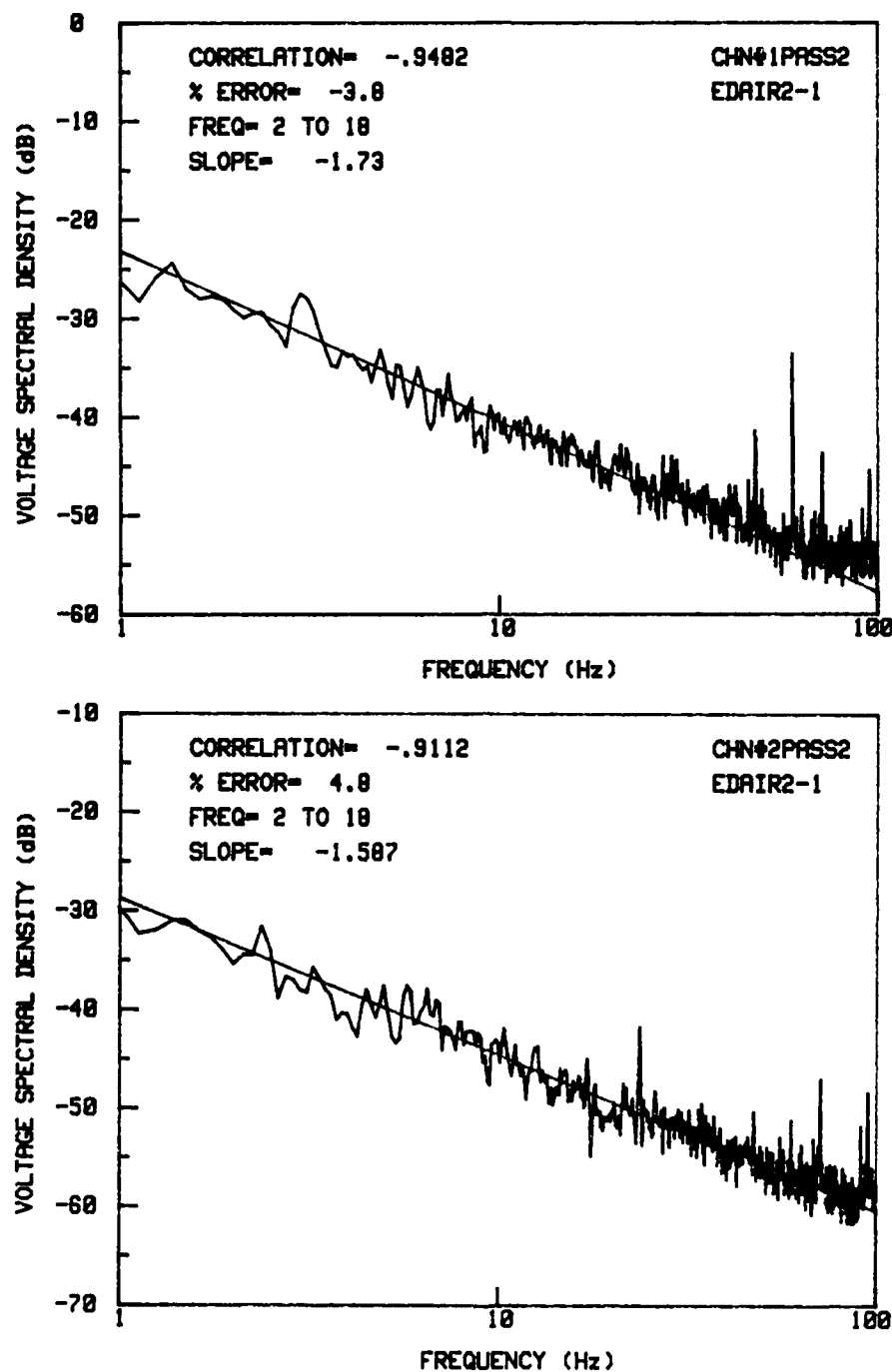


Figure 5b. Voltage variance spectra showing editing procedure. These spectra have been defiltered with the atmospheric filter function. This represents editing pass 2. Voltage power spectral density (dB) is plotted against frequency (log Hz). For each record, channel 1 (top) is temperature variance and channel 2 (bottom) is velocity variance. Channel number, pass number, and coded flight name and record number are shown interior to each graph. The slanted line represents the regression fit. Regression slope, correlation coefficient, and percent error are given in the upper left corner of each spectrum. The same three dual-channel records in flight 2 are shown as in Figure 1.

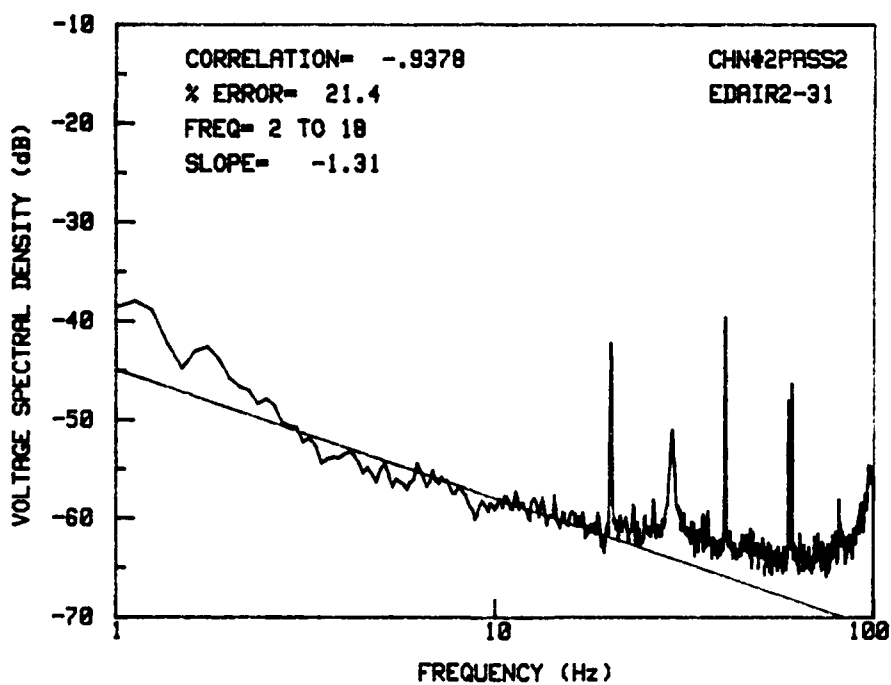
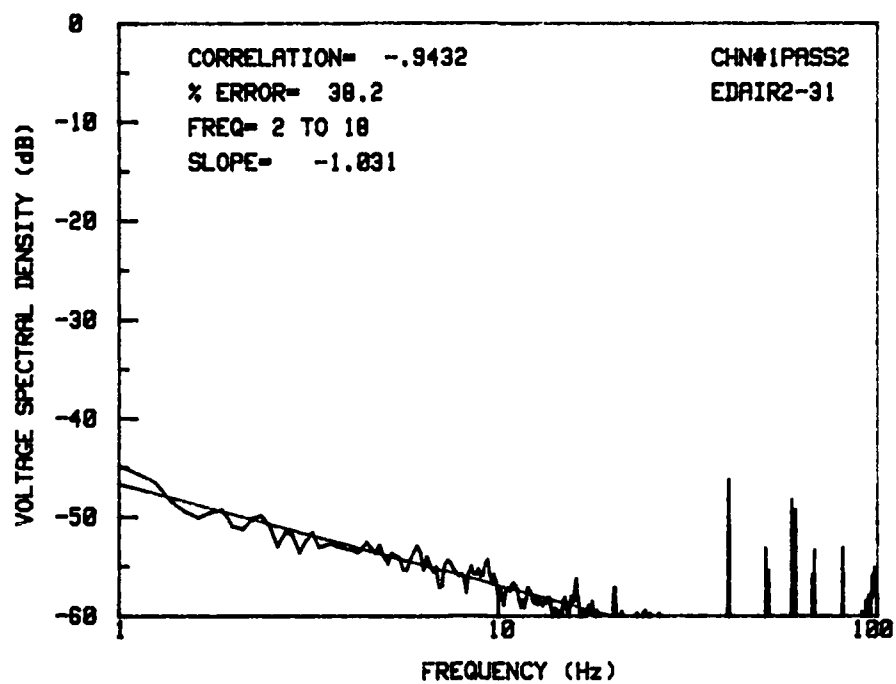


Figure 5b. (continued)

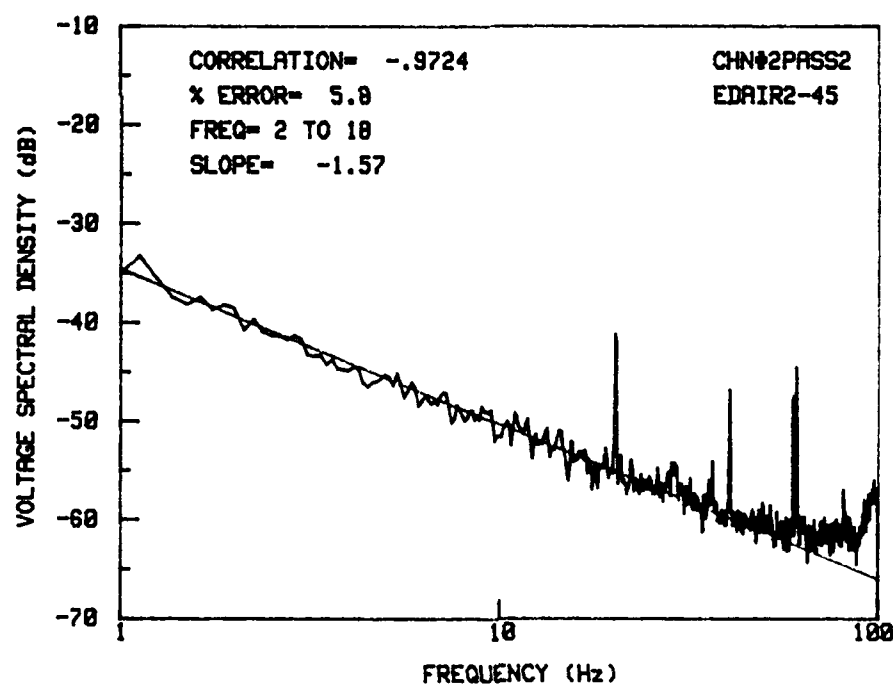
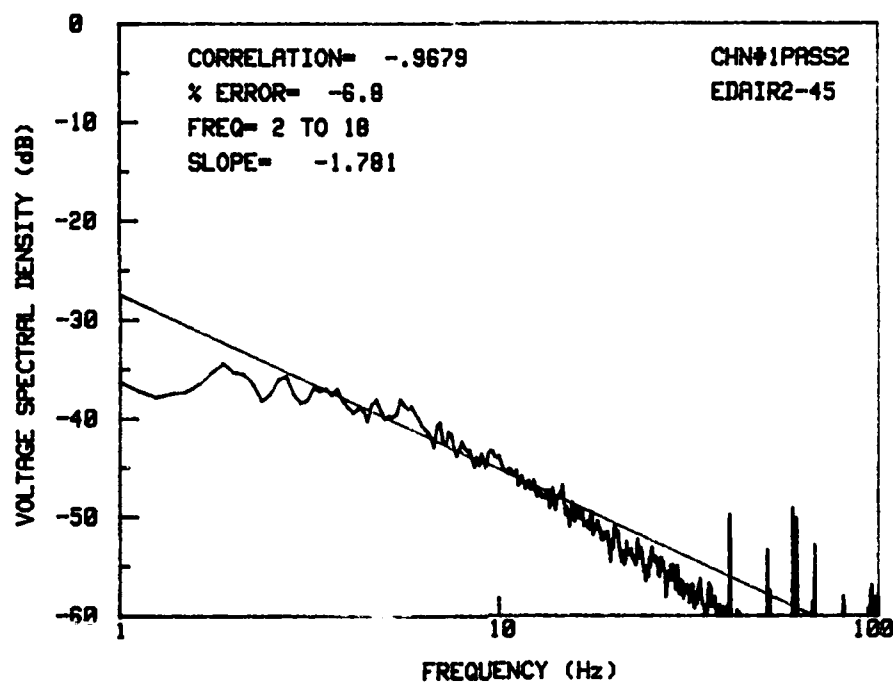


Figure 5b. (continued)

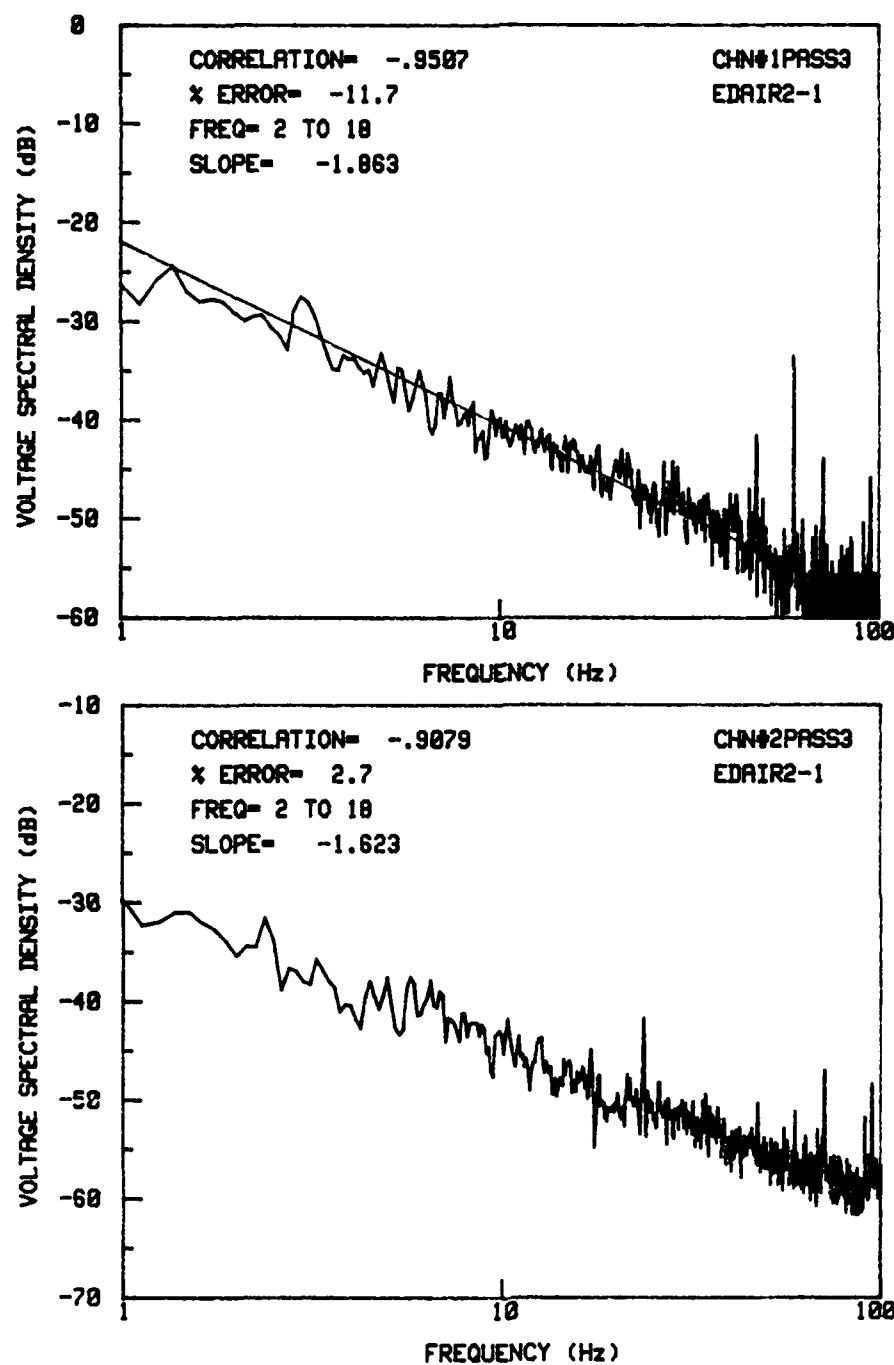


Figure 5c. Voltage variance spectra showing editing procedure. Average noise level has been subtracted from each defiltered spectrum. This represents editing pass 3. Voltage power spectral density (dB) is plotted against frequency (log Hz). For each record, channel 1 (top) is temperature variance and channel 2 (bottom) is velocity variance. Channel number, pass number, and coded flight name and record number are shown interior to each graph. The slanted line represents the regression fit. Regression slope, correlation coefficient, and percent error are given in the upper left corner of each spectrum. The same three dual-channel records in flight 2 are shown as in Figure 1.

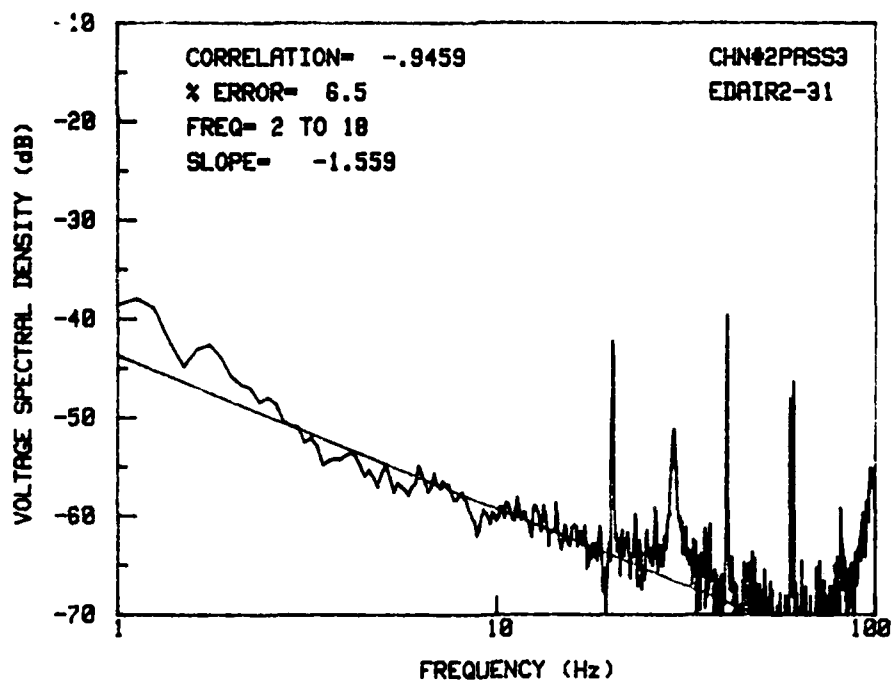
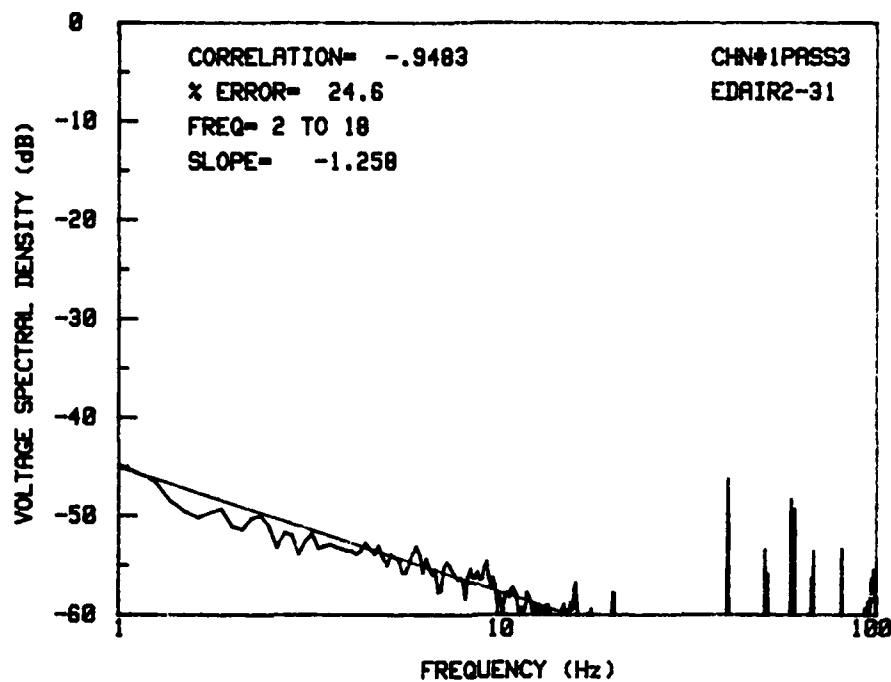


Figure 5c. (continued)

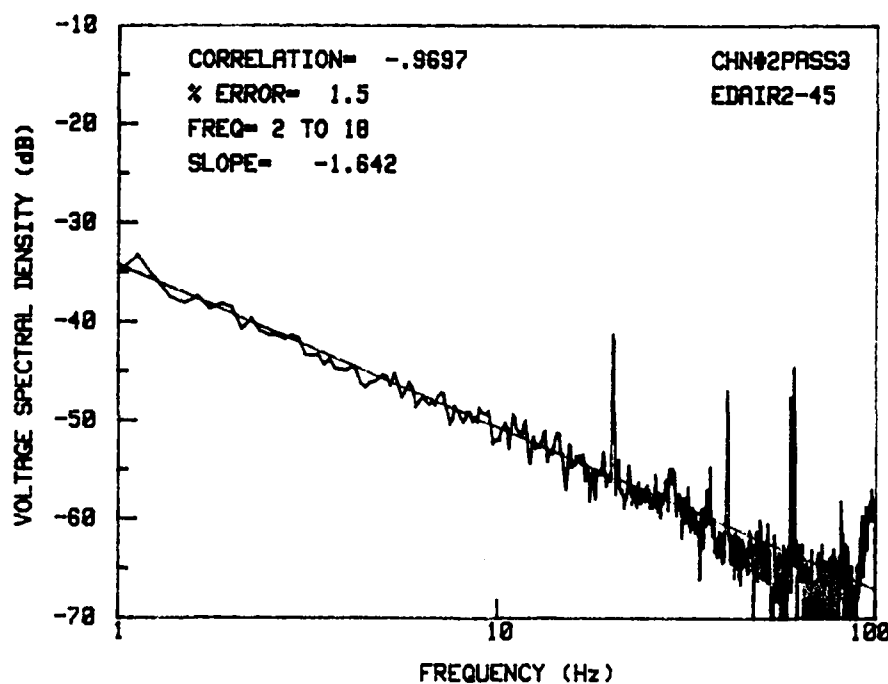
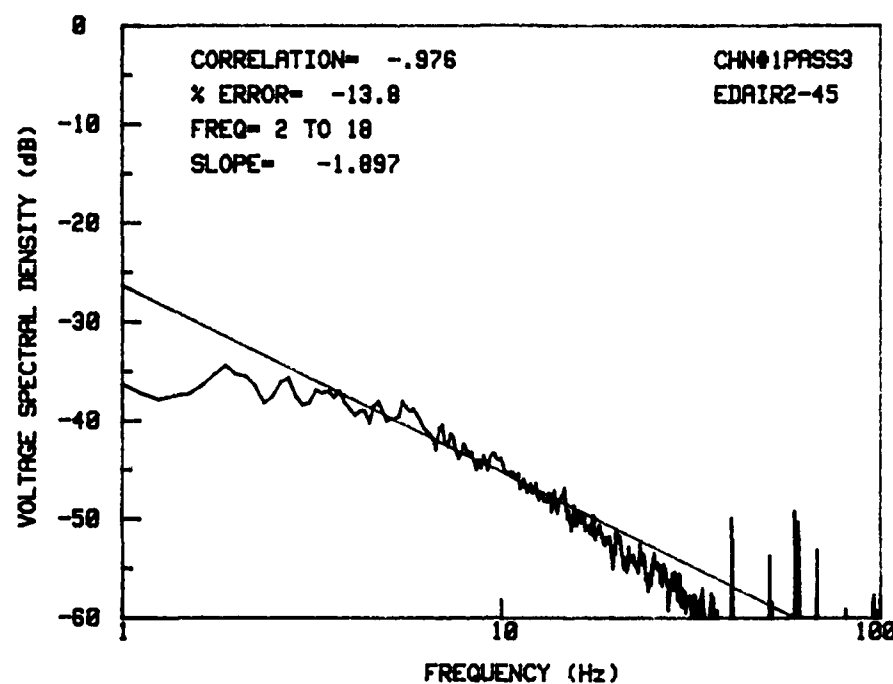


Figure 5c. (continued)

through pass 3. An average noise level was calculated from the twenty lowest spectral density values and subtracted from the entire spectrum. Figure 5c shows the same three records for pass 3. If the percent error on a new regression fit from 2 to 18 Hz was still greater than 15%, the spectrum was rejected on pass 3 and flagged. Spectra accepted on one of the above three passes were coded as "1". Flagged spectra were then manually examined. If a spectrum contained a visible portion of the inertial subrange that was represented by the regression fit, it was coded "2". Spectra with too small a signal-to-noise ratio (no visible inertial subrange) were coded "3". Unreal spectra were coded as "4". These unreal spectra were steeply sloped in log-log space. No theory predicts such a spectrum. Thus, these spectra were thought to be byproducts of measurement error, either overdriving the filter (i.e., amplitude fluctuations so great that filter saturation occurred) or noise distortion (e.g., change of aircraft power setting or a radio transmission). Code 4 spectra were eliminated from the analysis. All other analysis was performed on code 1 and 2 spectra, unless otherwise noted. Table 2 gives a representative breakdown of spectra by editing codes.

Based on the regression analysis, the following formulas were used to derive the spectral density necessary to calculate the structure parameters, C_T^2 and C_u^2 . 'X' was assigned to frequency and 'Y' to Volts²/Hz (spectral density). Using the power-law equation,

$$Y = a X^m \quad (6.1)$$

$$X^{5/3} Y = a X^{(m + 5/3)} \quad (6.2)$$

Table 2.

Representative editing results for each flight and in total. The breakdown of spectra in each pass for code 1 is shown, as well as the number of spectra in the remaining codes.

Temperature Spectra						
<u>Flight</u>	<u>Cold 1 :</u>			<u>Code 2</u>	<u>3</u>	<u>4</u>
	<u>Pass 1</u>	<u>2</u>	<u>3</u>			
2	12	2	12	13	0	9
3	10	4	2	6	0	5
4	12	2	3	5	0	3
6	28	1	10	8	0	0
7I	21	0	1	4	0	0
7II	33	2	1	2	0	0
8	21	0	3	11	0	2
9	19	3	5	5	1	0
10	34	6	5	9	0	0
11I	17	1	7	17	0	0
11II	2	2	3	13	0	0
12	13	2	3	19	0	2

Table 2.
(continued)

Velocity Spectra						
<u>Flight</u>	<u>Code 1</u> :			<u>Code 2</u>	<u>3</u>	<u>4</u>
	<u>Pass 1</u>	<u>2</u>	<u>3</u>			
2	27	4	9	2	5	1
3	21	0	4	1	1	0
4	6	0	0	0	0	19
6	34	0	3	7	1	2
7I	25	0	0	1	0	0
7II	36	0	2	0	0	0
8	28	2	3	2	1	1
9	28	0	3	1	0	1
10	53	1	0	0	0	0
11I	33	0	2	2	0	5
11II	16	0	2	2	0	0
12	21	1	5	2	0	10

TOTALS

Temperature Spectra

<u>Code 1</u> :	<u>Pass 1</u>	<u>2</u>	<u>3</u>	<u>Code 2</u>	<u>3</u>	<u>4</u>
	222	25	55	112	0	21

Velocity Spectra

<u>Code 1</u> :	<u>Pass 1</u>	<u>2</u>	<u>3</u>	<u>Code 2</u>	<u>3</u>	<u>4</u>
	328	8	33	20	8	39

$$Q = X^{5/3} Y \quad (6.3)$$

$$a = Y / X^m \quad (6.4)$$

$$Q = 10^{(\langle \log Y \rangle - m \langle \log X \rangle)} 10^{(m + 5/3) \langle \log X \rangle} \quad (6.5)$$

$$Q = 10^{(\langle \log Y \rangle + 5/3 \langle \log X \rangle)} \quad (6.6)$$

$$Q = 10^{[(\Sigma \log Y)/N + 1.667 (\Sigma \log X)/N]} \quad (6.7)$$

where Q is the spectral density times frequency to the 5/3 and is based on the spectral density and frequency values midrange in the regression fit. Q is a necessary input parameter for the C_T^2 and C_u^2 equations (equations 5.23 and 5.24), calculated from the temperature and velocity turbulence spectra, respectively.

6.2 Mean Aircraft Meteorological Profiles

The aircraft temperature and humidity profiles were digitized at levels corresponding to the profiler high resolution range gate heights. Dewpoint temperature was converted to vapor pressure, e , over water using the following formula (Iribarne and Godson 1981).

$$\log e = -(2937.4 / T) - 4.9283 \log T + 23.5471 \quad (6.8)$$

where e is vapor pressure in mb and T is in Kelvin. Vapor pressure was then converted to specific humidity, q , using the approximation $e \approx (P q)/0.622$. Potential temperature and temperature have the defined relationship

$$\theta = T (1000 \text{ mb}/P)^{0.286} \quad (6.9)$$

with pressure from the standard atmosphere relationship

$$P = P_0 e^{-(z/8)} \quad (6.10)$$

where P_0 is 1013.2 mb, altitude z is in km and scale height H is ≈ 8 km (Iribarne and Godson 1981; Wallace and Hobbs 1977). Aircraft potential temperature profiles are shown for all flights in Figure 6. Aircraft specific humidity profiles for only the PSU flights are shown in Figure 7.

6.3 Other Data Sources

Profiler data was logged at one hour intervals denoted by the GMT time (zulu time, "z") at the end of the average period. Height is given in m, wind speed in m/s, direction in degrees, and C_n^2 (radar) in $m^{-2/3}$ (Mike Moss, letter to author, July 1987; Mike Moss, letter to author, November 1987). Radar wind profiles for the PSU flights are shown in Figure 8.

AFGL thermosonde data was available at 20 m resolution. The following information was available for each level: altitude (km), pressure (mb), temperature ($^{\circ}C$), relative humidity (%), C_n^2 ($m^{-2/3}$), wind speed (m/s), and direction (degrees) (Robert Beland, letter to William Syrett, September 1986). AFGL thermosonde potential temperature profiles corresponding to aircraft flights are shown in Figure 9. Corresponding AFGL thermosonde specific humidity, mean wind, and calculated raw C_n^2 profiles are shown in Figures 10, 11, and 12, respectively.

AFGL scintillometer data was provided as seven-level profiles with C_n^2 in $m^{-2/3}$, and height (corrected for zenith angle) in km

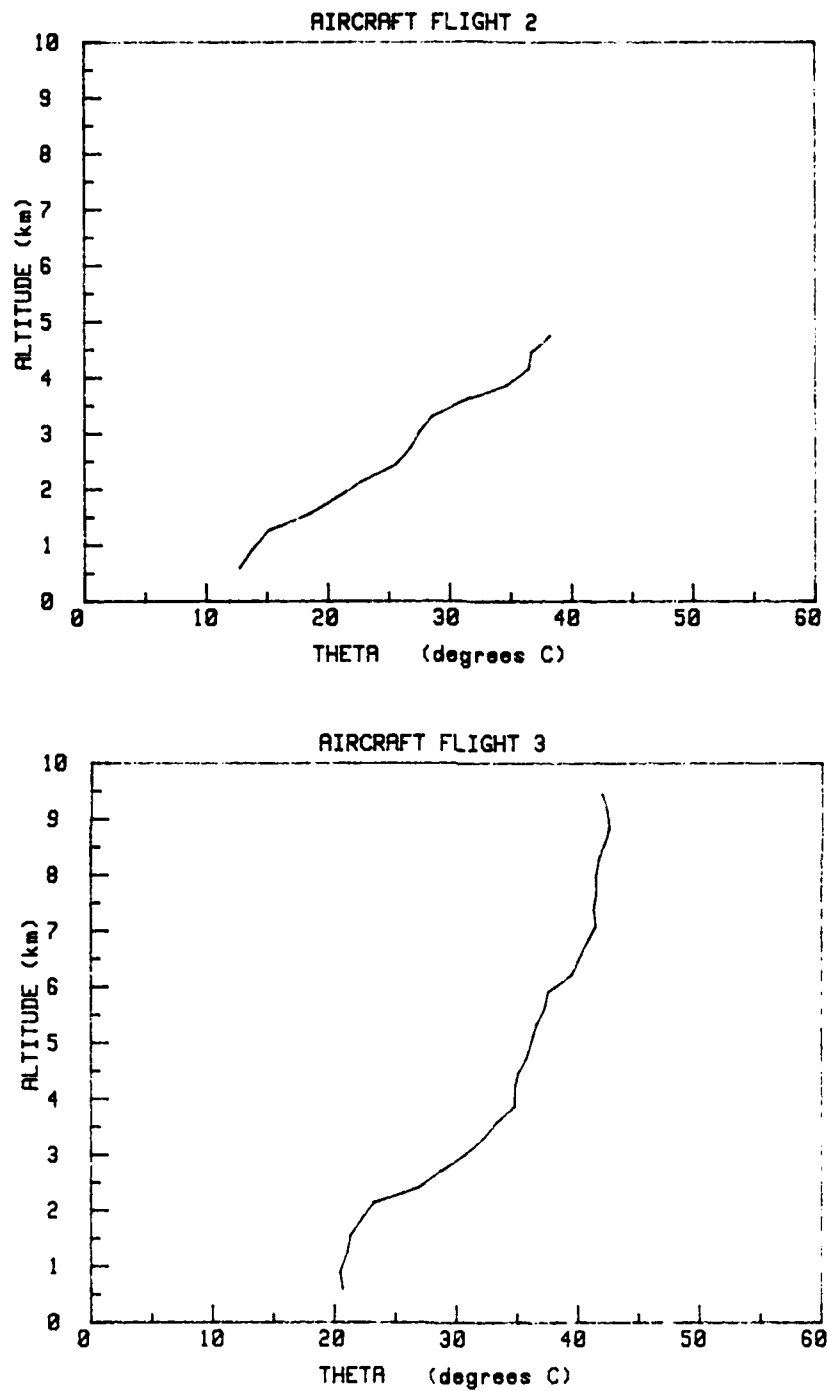


Figure 6. Potential temperature (theta) vertical profiles as measured by aircraft instrumentation. Altitude is MSL. Flights 2-12 are shown (labeled above each graph).

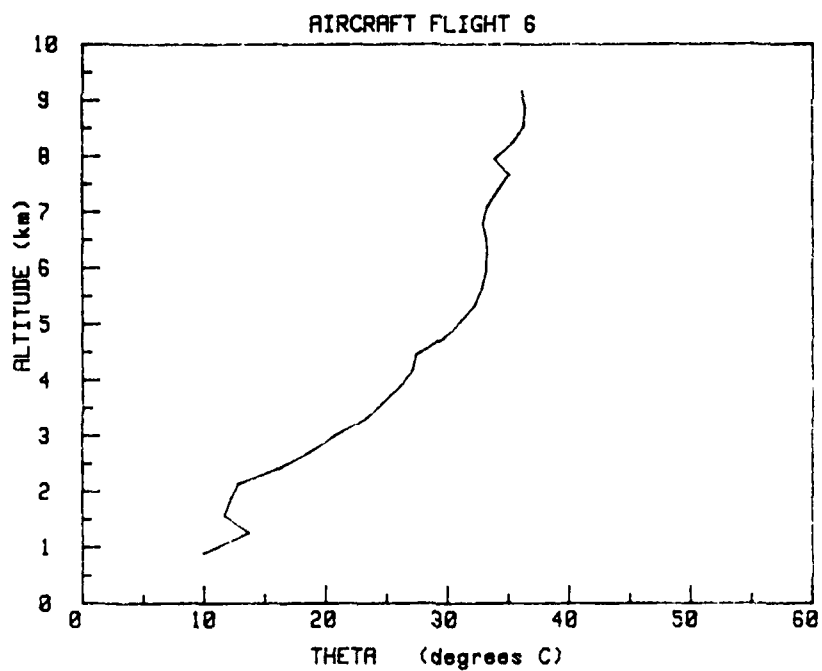
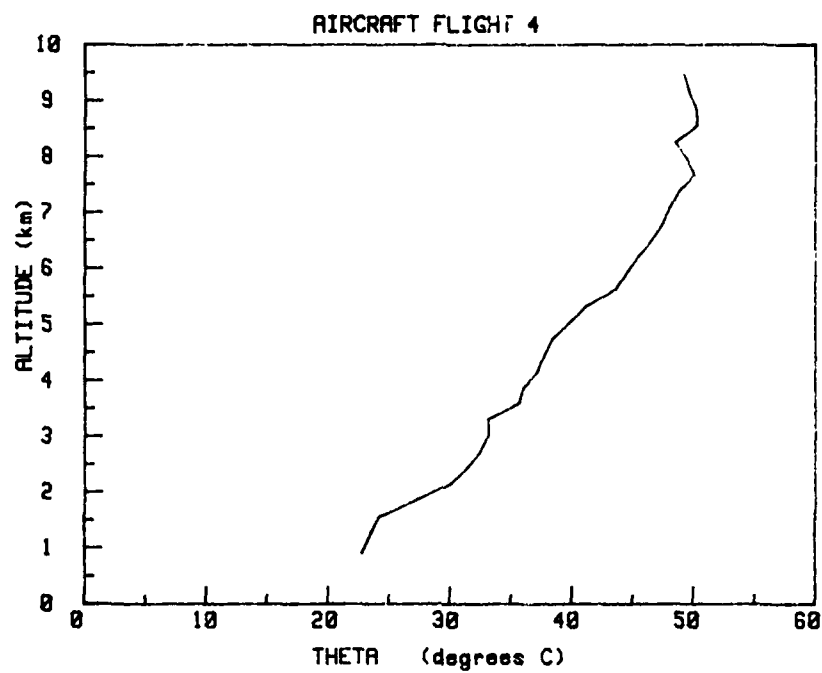


Figure 6. (continued)

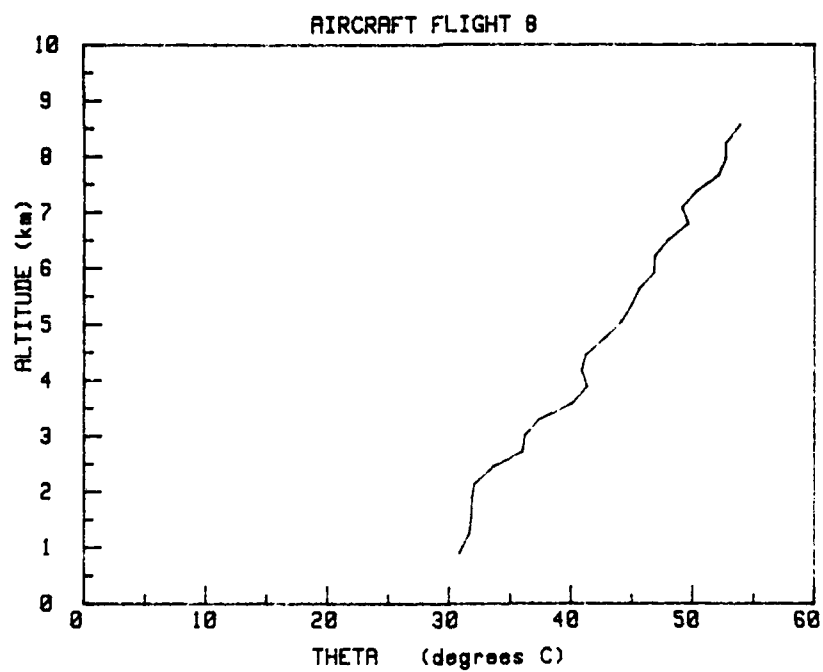
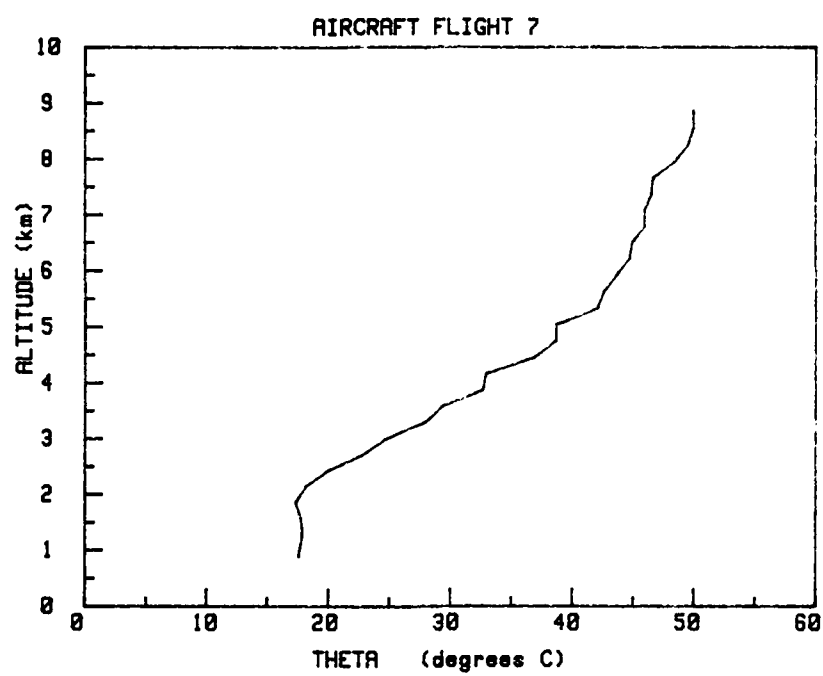


Figure 6. (continued)

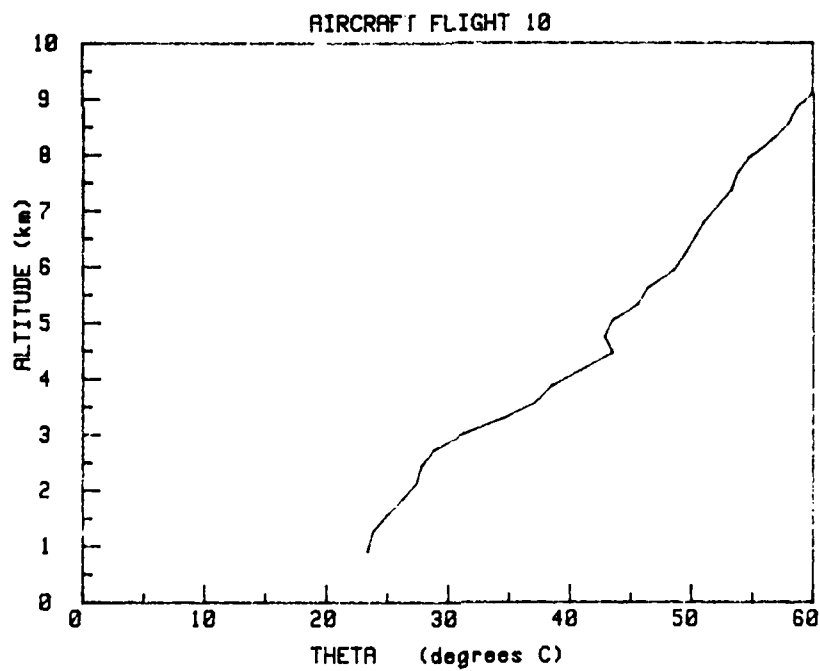
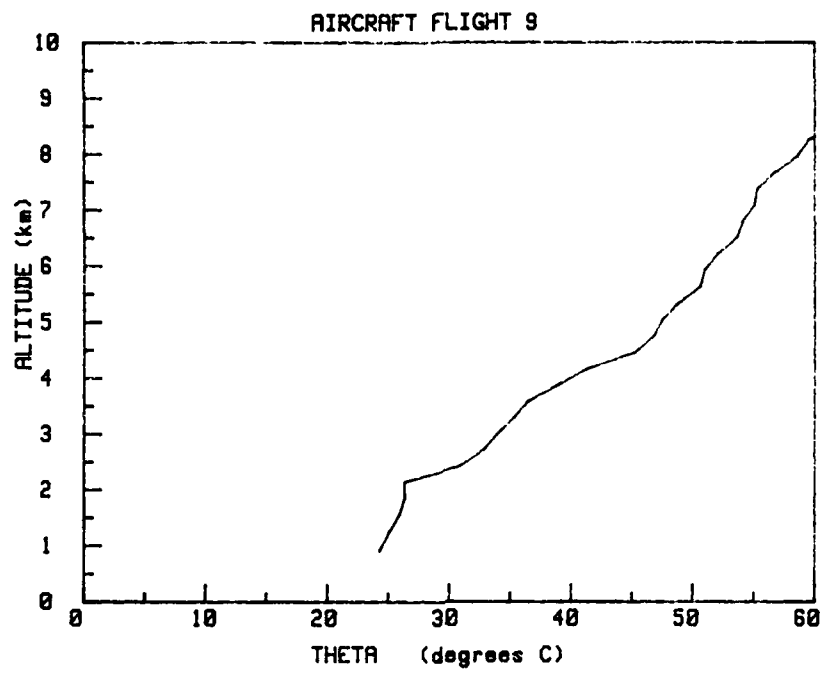


Figure 6. (continued)

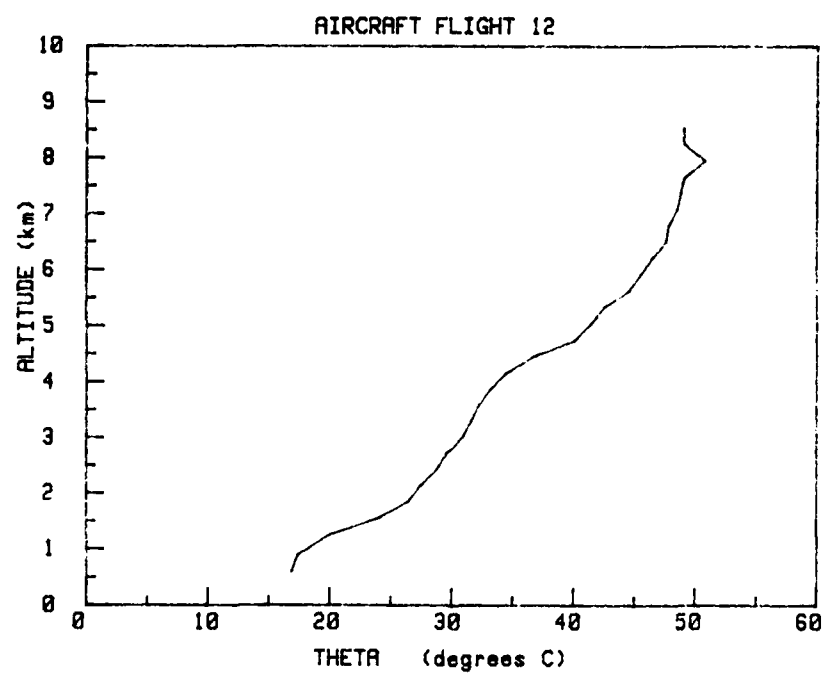
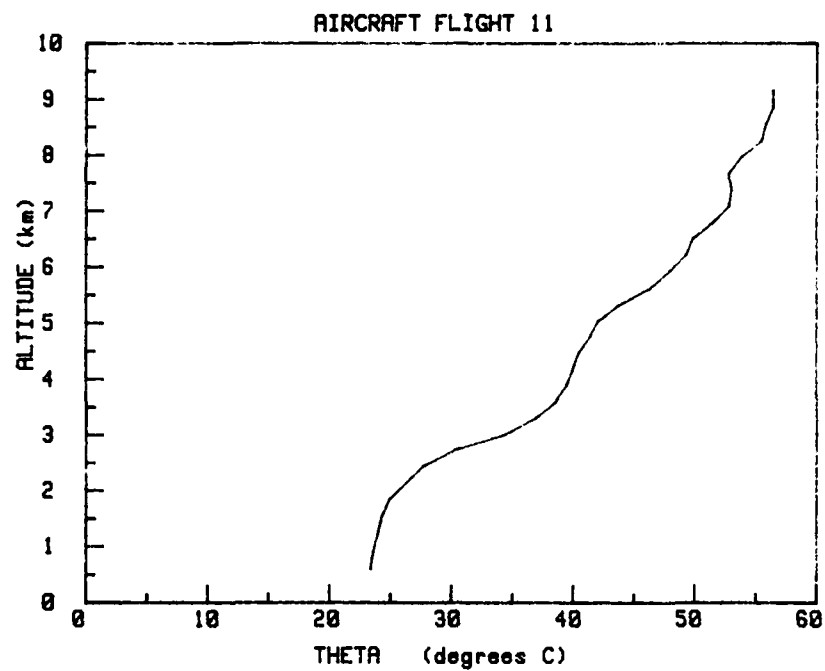


Figure 6. (continued)

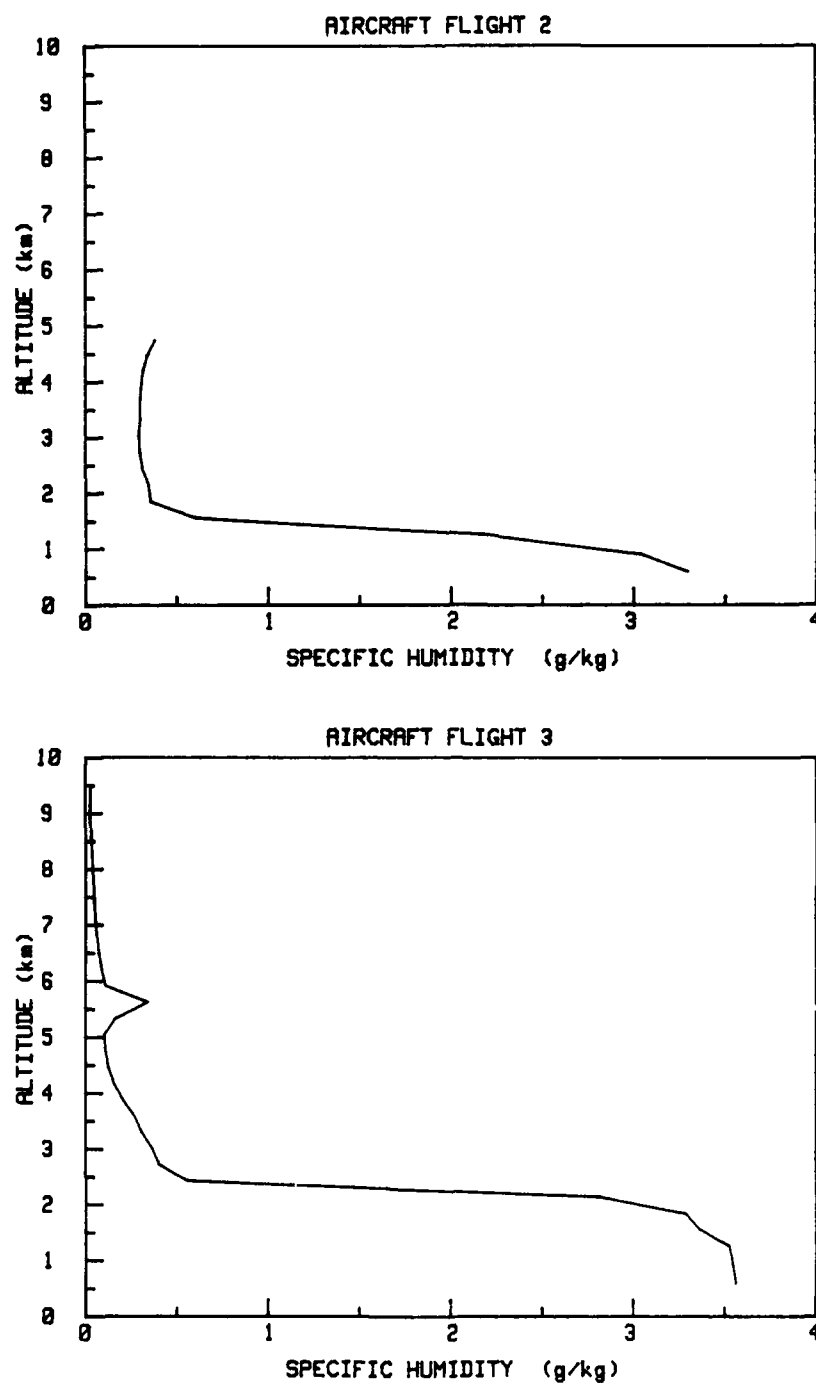


Figure 7. Specific humidity vertical profiles as measured by aircraft instrumentation. Altitude is MSL. Only flights during which the PSU profiler operated are shown, Flights 2-8 (labeled above each graph).

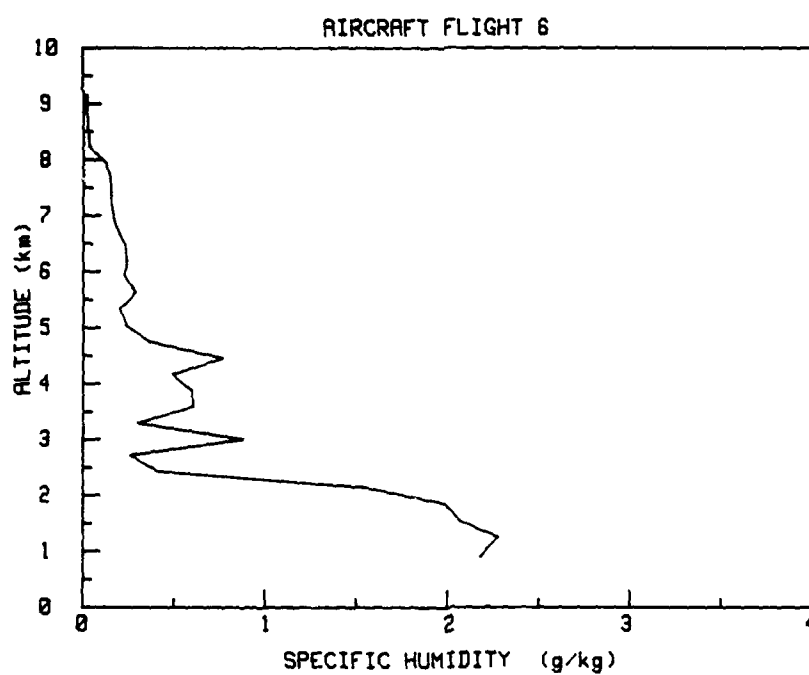
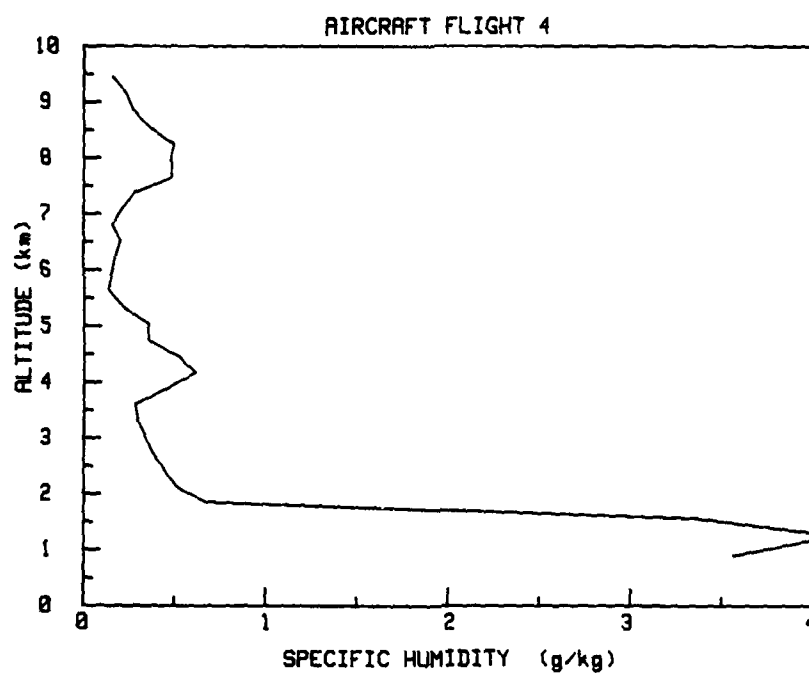


Figure 7. (continued)

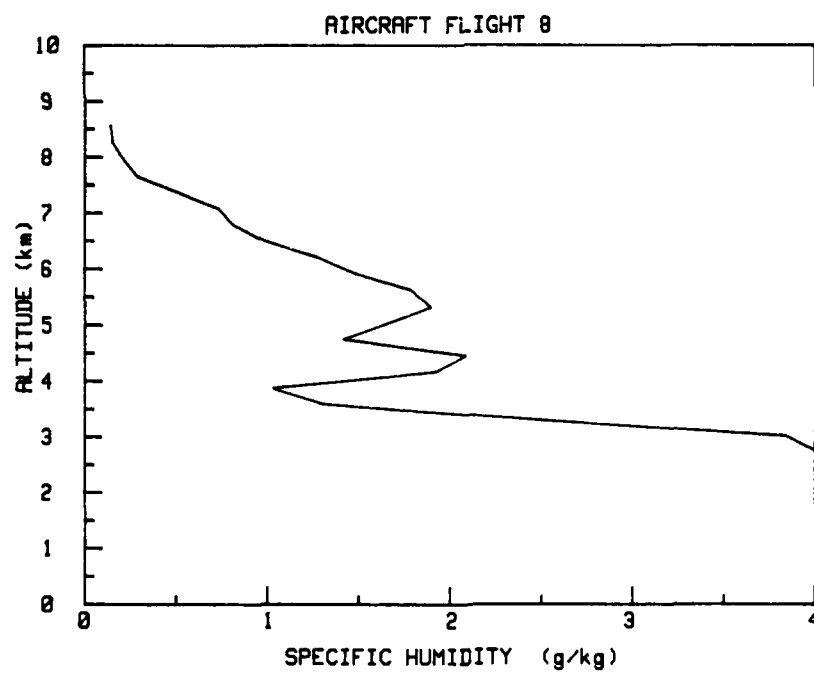
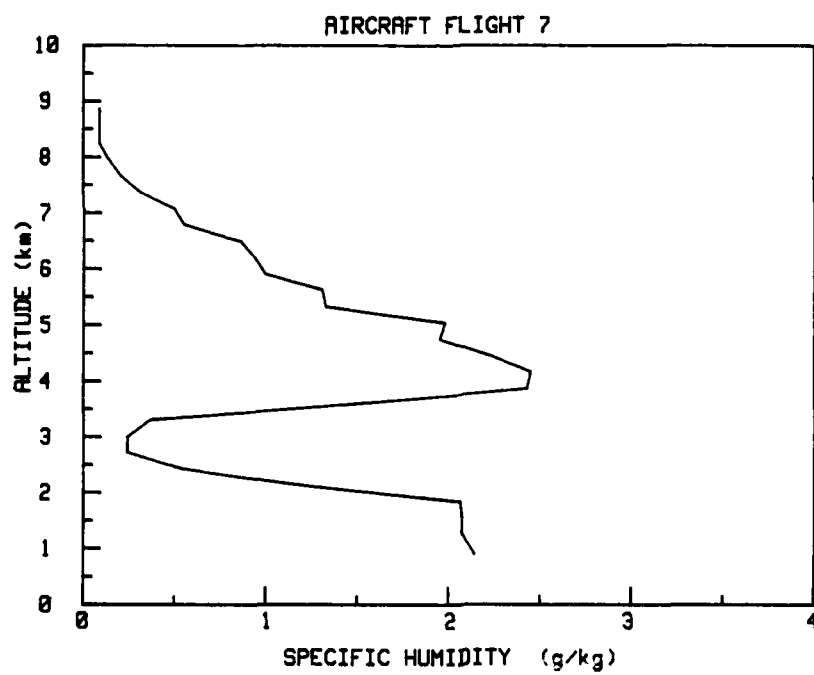


Figure 7. (continued)

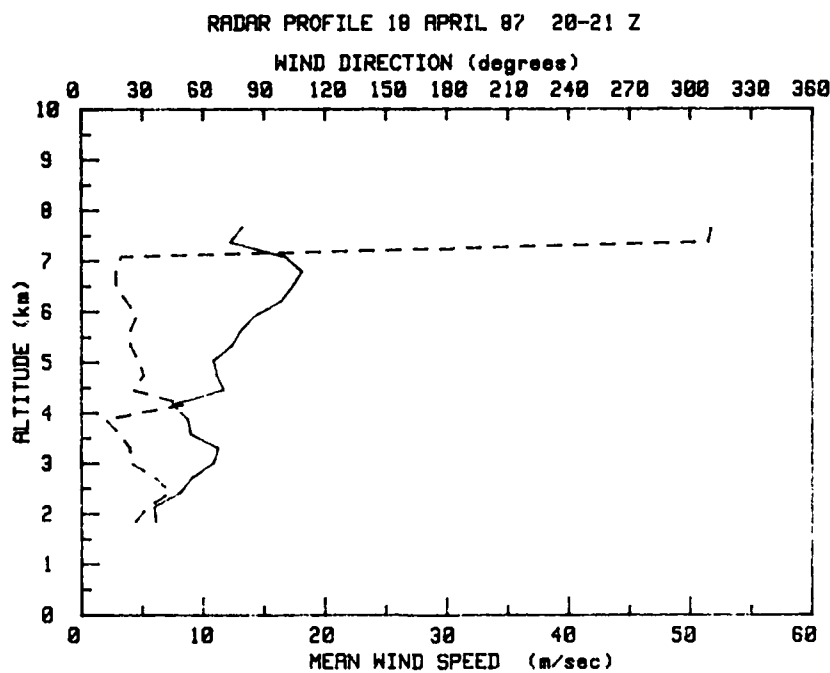
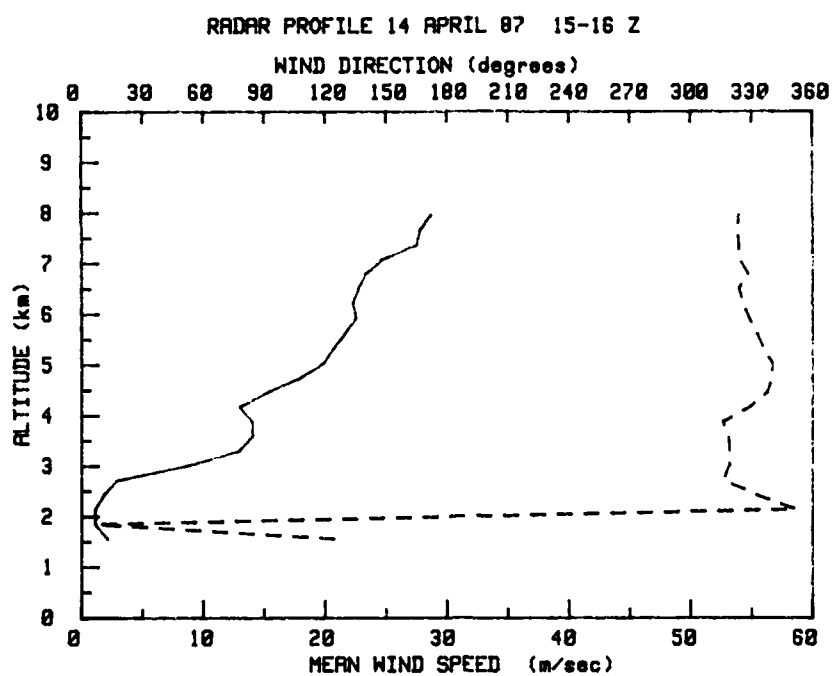


Figure 8. Mean wind speed (solid line) and direction (broken line) as measured by the profiler. Date and the hour interval averaged are given above each graph. Altitude is MSL.

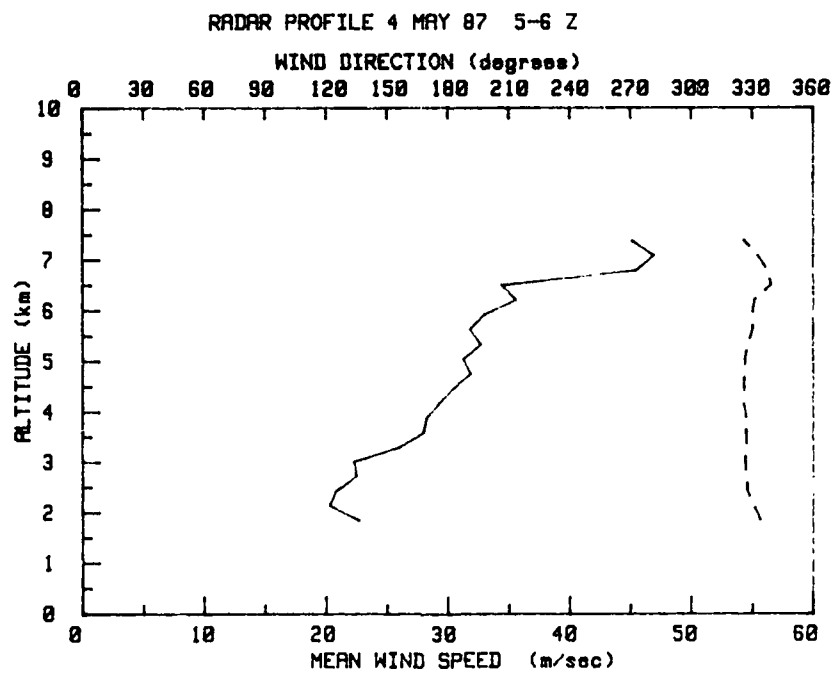
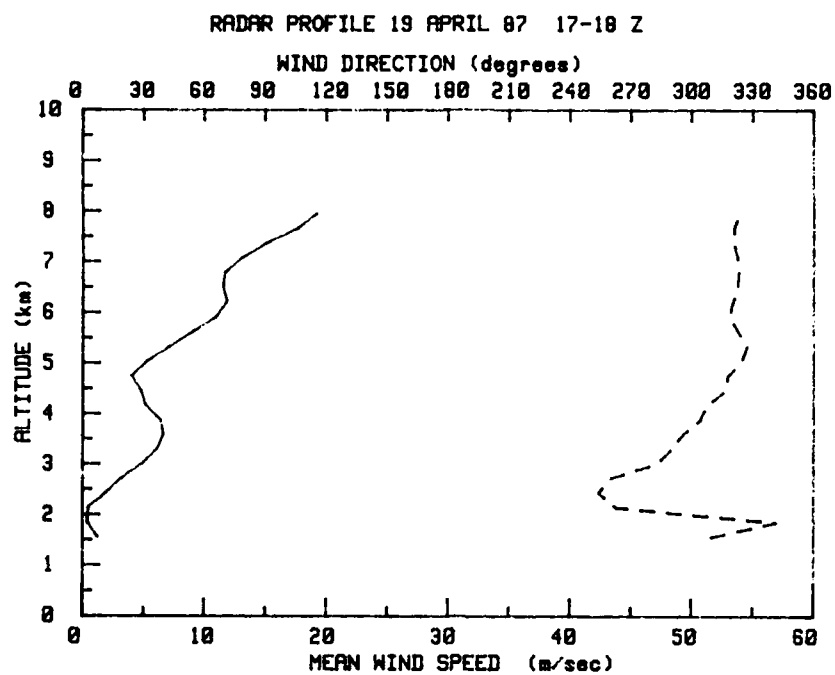


Figure 8. (continued)

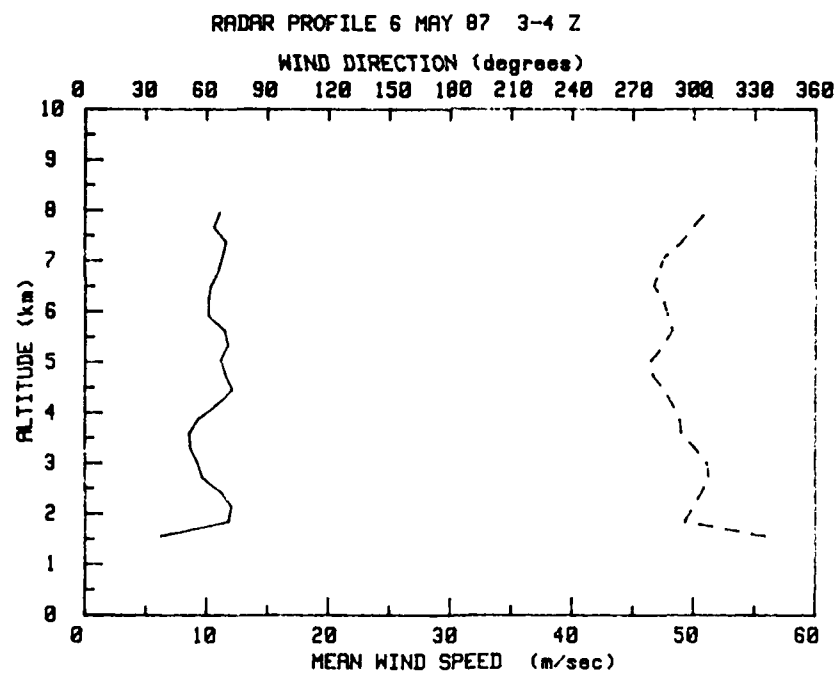
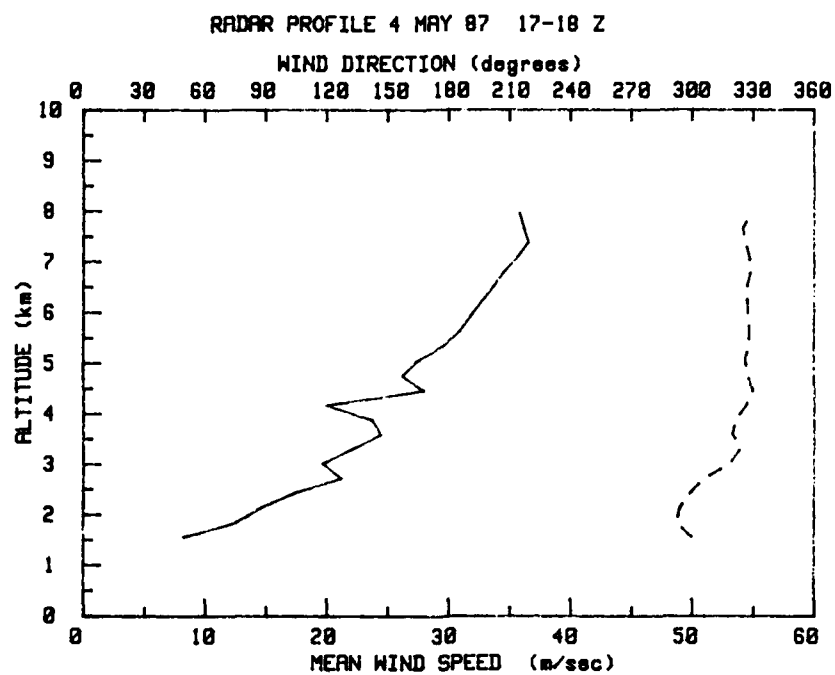


Figure 8. (continued)

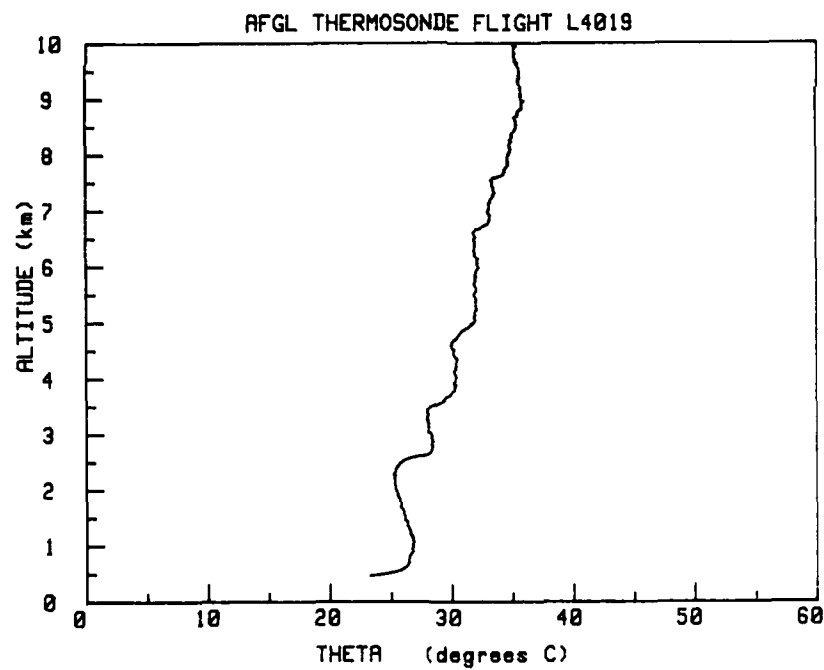
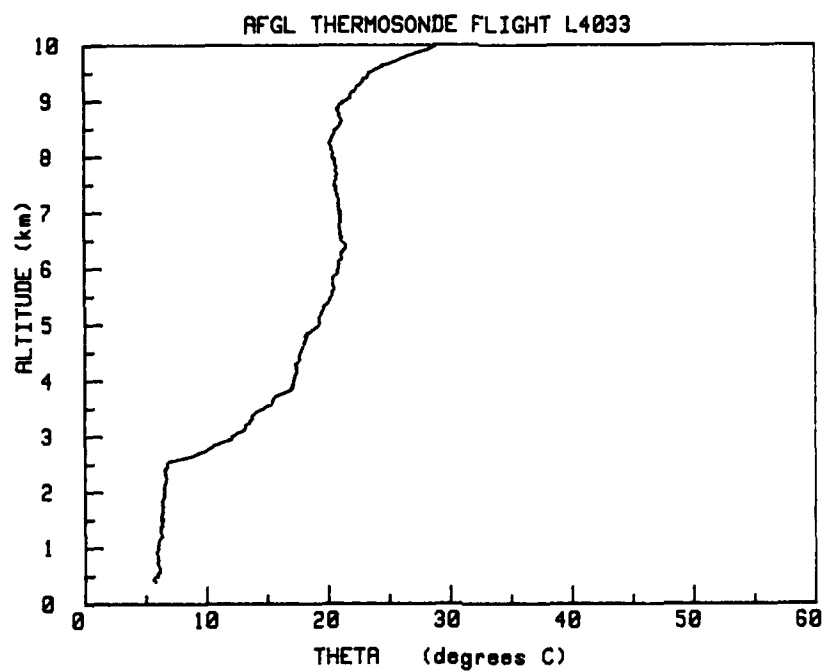


Figure 9. AFGL thermosonde-measured potential temperature vertical profiles correlating to aircraft flights. Altitude is MSL. Thermosonde flight number is given above each graph.

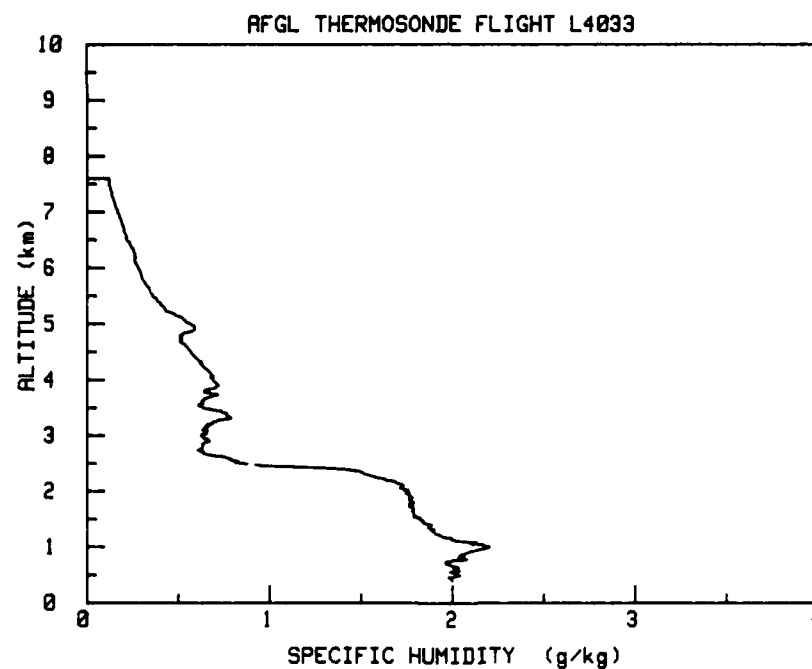
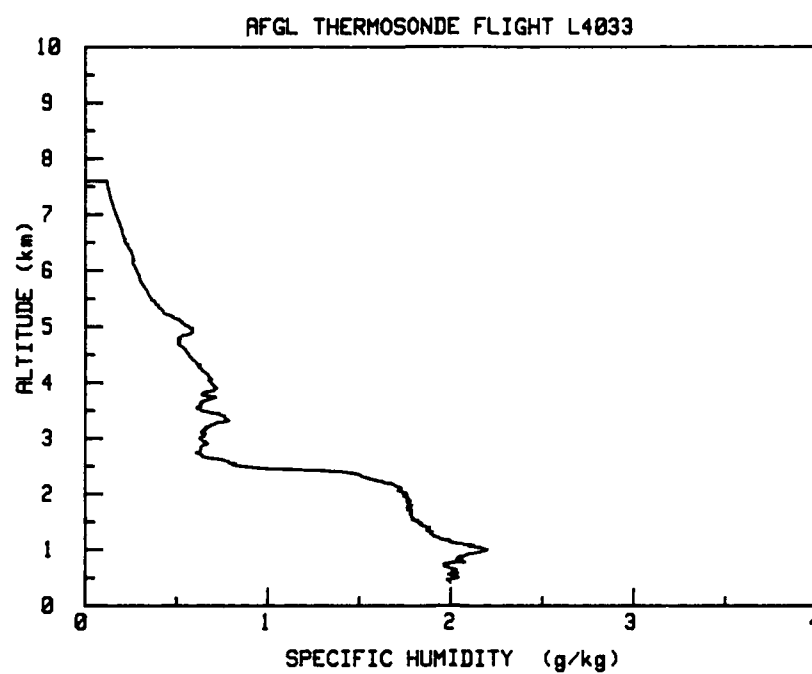


Figure 10. AFGL thermosonde-measured specific humidity vertical profiles correlating to aircraft flights. Altitude is MSL. Thermosonde flight number is given above each graph.

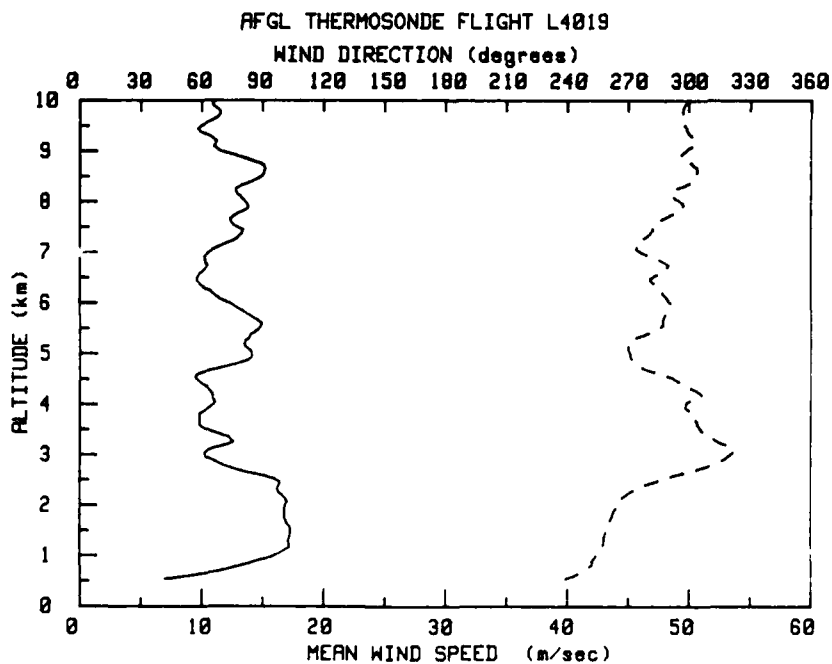
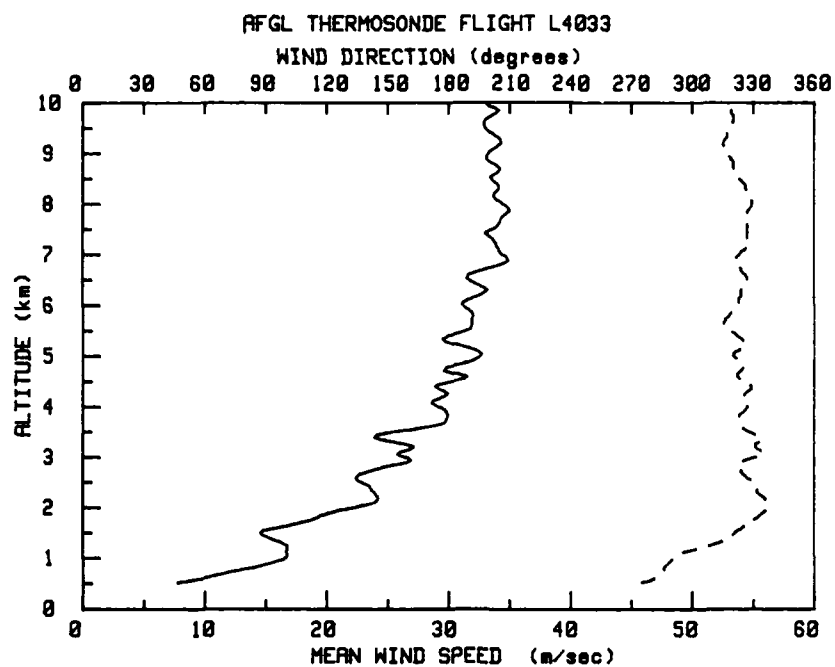


Figure 11. AFGL thermosonde-measured vertical profiles of mean wind speed (solid line) and direction (broken line). Altitude is MSL. Thermosonde flight number is given above each graph.

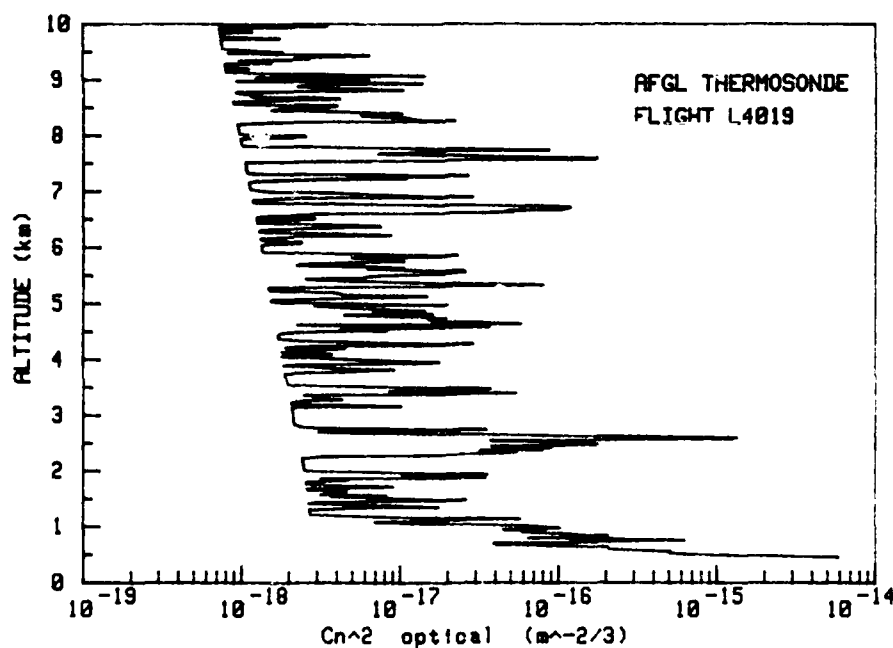
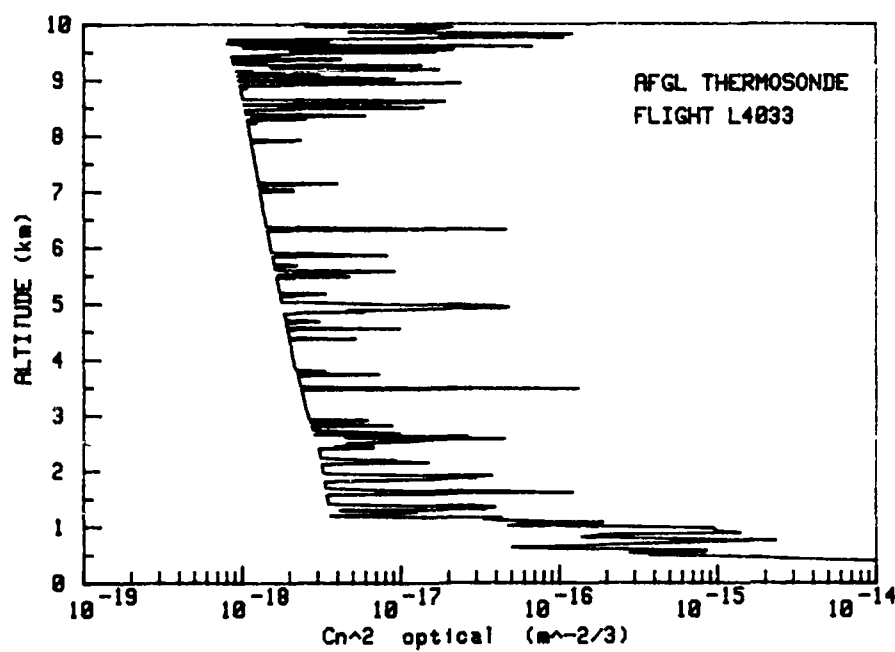


Figure 12. AFGL thermosonde-calculated vertical profiles of raw C_n^2 -optical based on measured C_T^2 . Altitude is MSL.

Thermosonde flight number is given interior to each graph.

(Murphy and Battles 1986). AFGL scintillometer profiles corresponding to aircraft flights are shown in Figure 13.

RADC scintillometer data was provided as seven-level profiles with C_n^2 in $m^{-2/3}$ at the standard kernel levels (AGL altitude assuming zenith angle of zero) (Donald Stebbins, letter to author, September 1986). Only one data run corresponded to the aircraft flight times. It is shown in Figure 14.

NPS r_o scintillometer data was provided as r_o in cm as a function of zulu time (Donald Walters, telephone conversation, November 1987). Data taken during aircraft flight was limited to one night, 4 May 1986. The average value of r_o during this time segment, 0400-0540 Z, was 5 cm.

AFWL isoplanometer data was unavailable for use in this comparison.

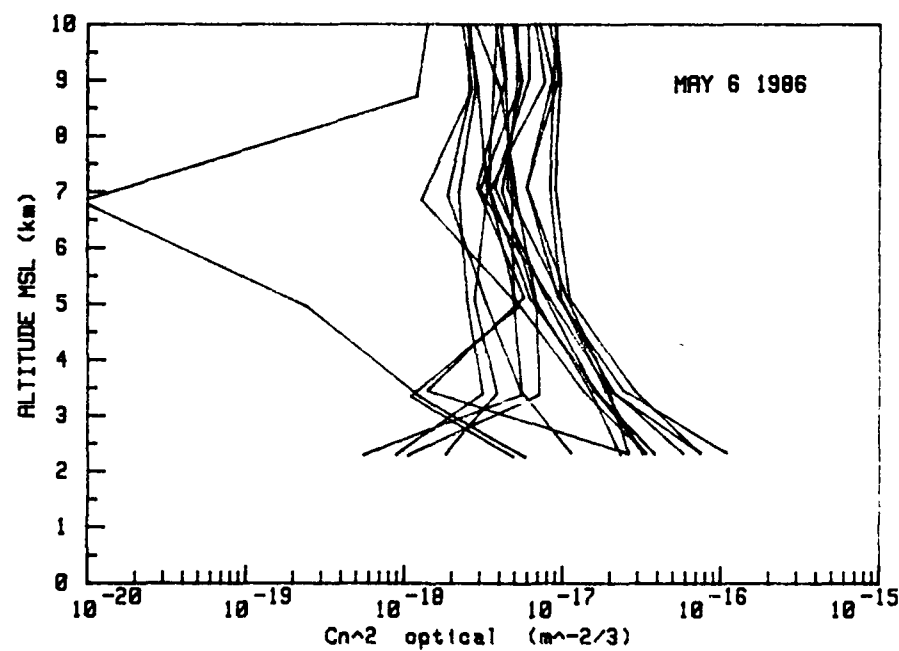
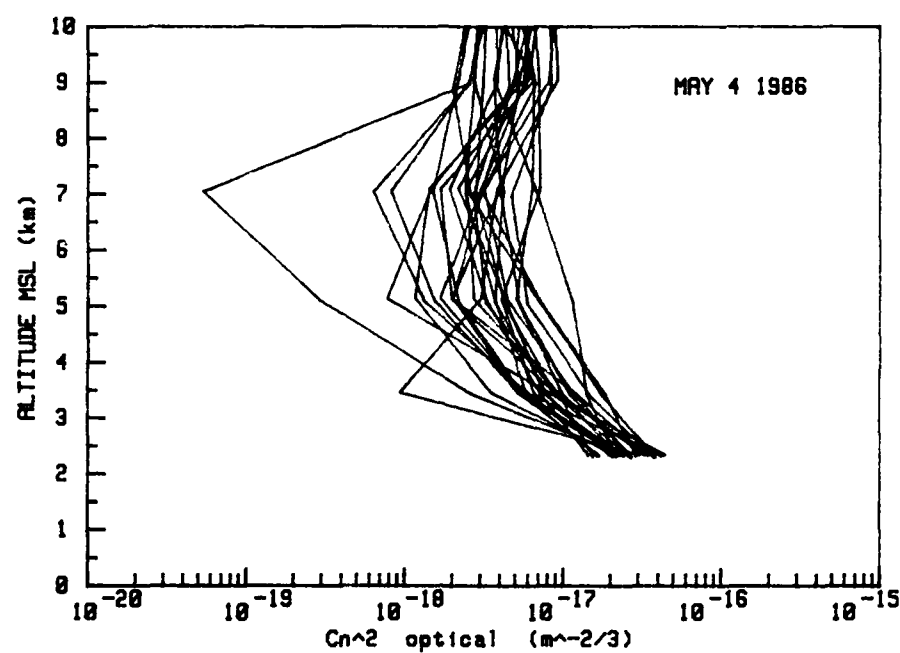


Figure 13. AFGL scintillometer-measured vertical profiles of C_n^2 -optical taken during the aircraft flight time period. Altitude AGL has been adjusted to MSL. Date is given interior to each graph.

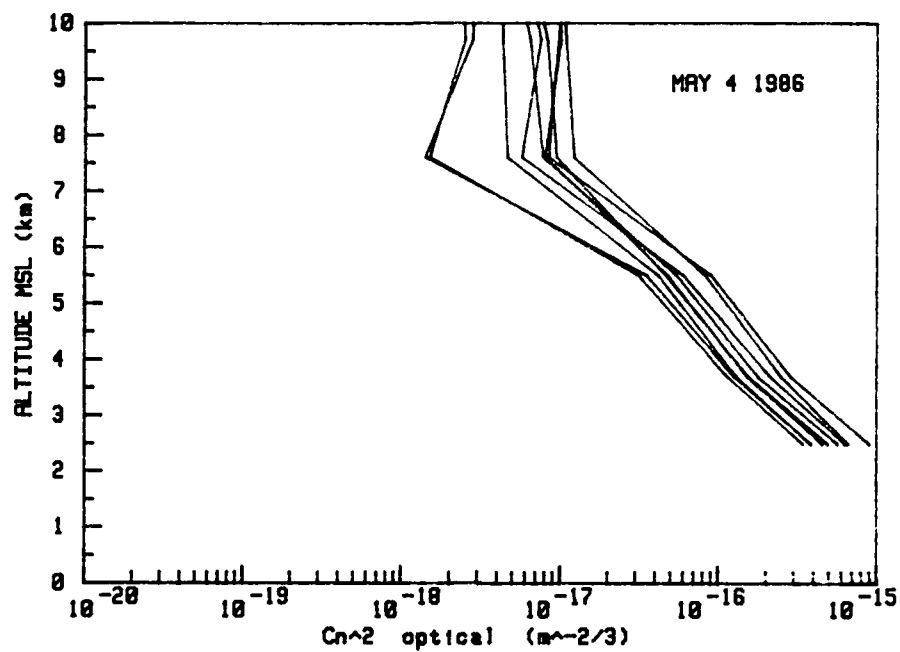


Figure 14. RADC scintillometer-measured vertical profiles of C_n^2 -optical taken during the aircraft flight time period. Altitude AGL has been adjusted to MSL. Date is given interior to the graph.

CHAPTER 7

RESULTS AND DISCUSSION

7.1 Analysis of C_T^2/C_u^2

The vertical profiles of C_u^2 and C_T^2 calculated from the aircraft data show strong correlation for flights 2, 6(ascent and descent), 8(ascent and descent), 9(ascent), 10(descent), 11, and 12 (Figure 15). The other flights also show some correlation, but not at all levels. Correlation of higher values of these turbulence parameters indicates regions of the atmosphere that contain turbulent layers (Ottersten 1969). C_T^2 and C_n^2 are directly correlated at all levels for all flights, as is to be expected since C_n^2 is a function of C_T^2 .

A rough estimate of boundary layer height can be determined by spectral signal-to-noise ratio for these profiles, since the signal is much stronger in the turbulent boundary layer. For this purpose spectra were examined in detail manually. Table 3 gives an estimate of PBL height for each flight. If C_T^2 versus C_u^2 is graphed (for values above the boundary layer where the TKE and variance budget approximations discussed in Chapter 3 are valid), a power-law relation is evident (Figures 16 and 17). This ratio is proportional to Richardson number and temperature gradient (right hand side of equation 3.28). All flights except 6(ascent and descent), 7(descent), and 11(ascent) show distinct sloped correlations. All flights were plotted simultaneously and a regression analysis was done to determine slope and goodness-of-fit (Figure 18). The plot of flight 6 had high scatter. Removal of this flight decreased the scatter and thus

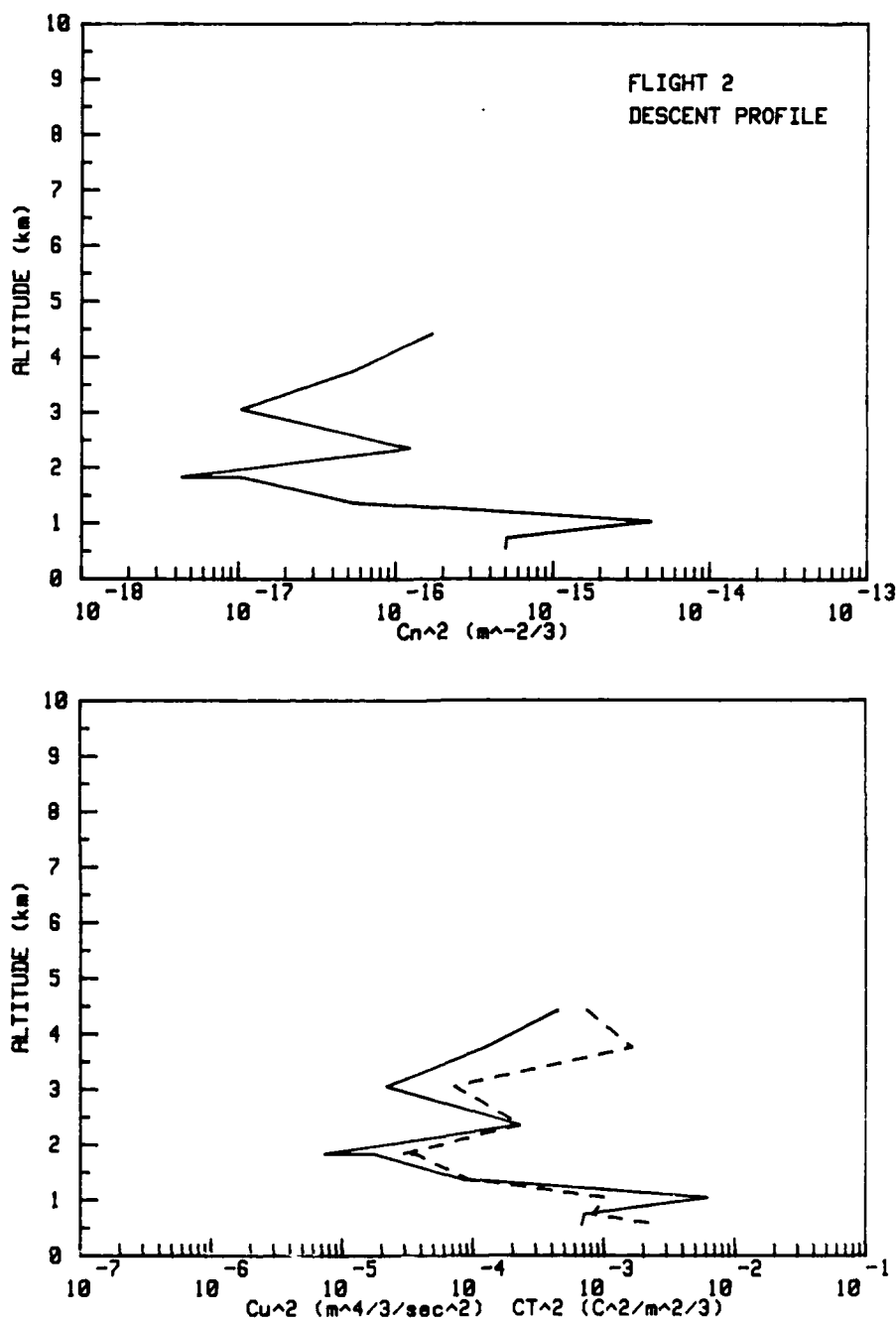


Figure 15. Vertical profiles of C_n^2 , C_T^2 , and C_u^2 . The top graph shows the C_n^2 profile calculated from the C_T^2 profile. C_T^2 (solid line) and C_u^2 (broken line) are shown on the bottom graph versus MSL altitude. These values were calculated from the aircraft spectral data. The flight number and ascent/descent designation for the profile is given interior to the top graph. Dual graphs are shown for flights 2-12.

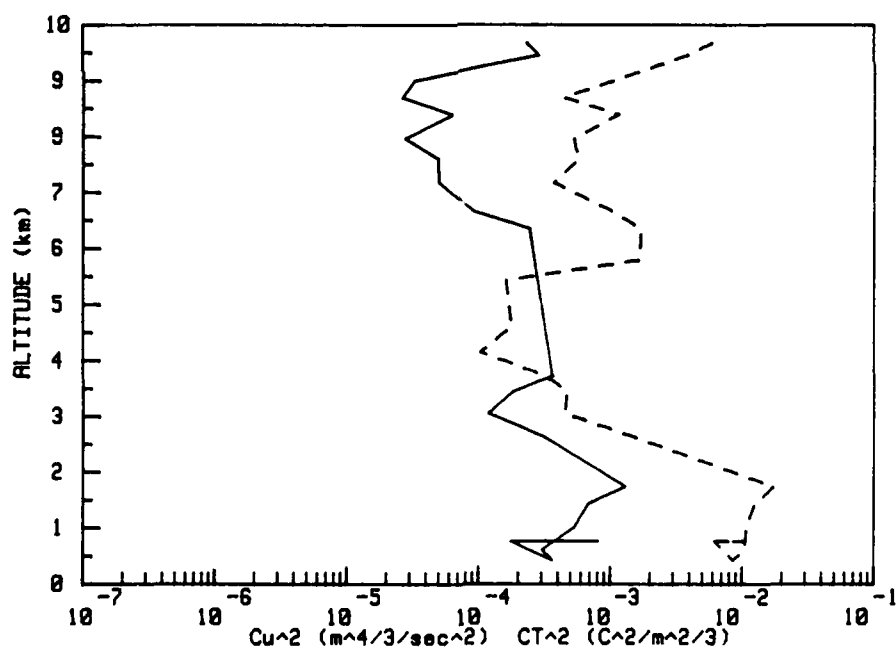
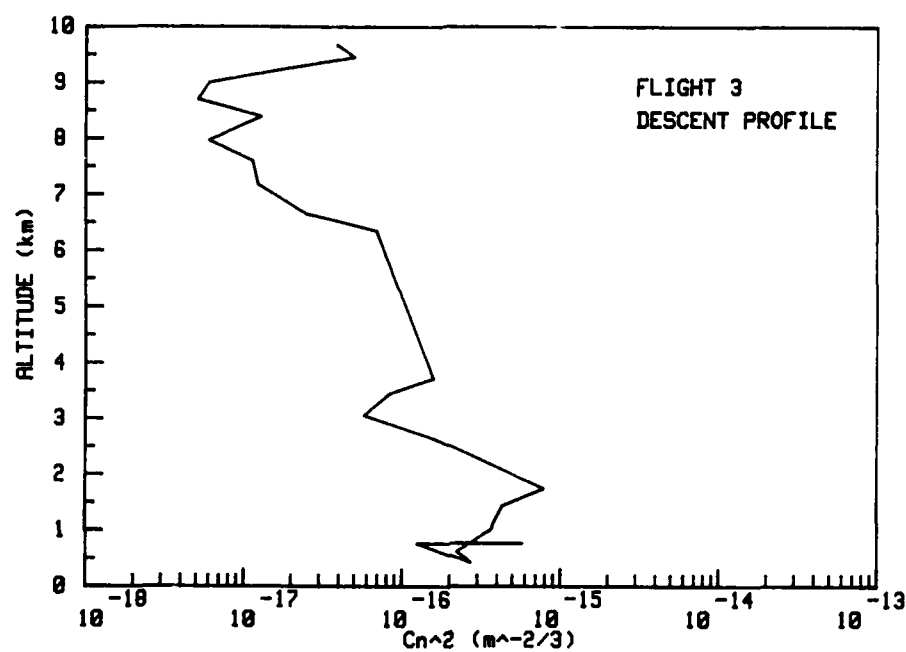


Figure 15. (continued)

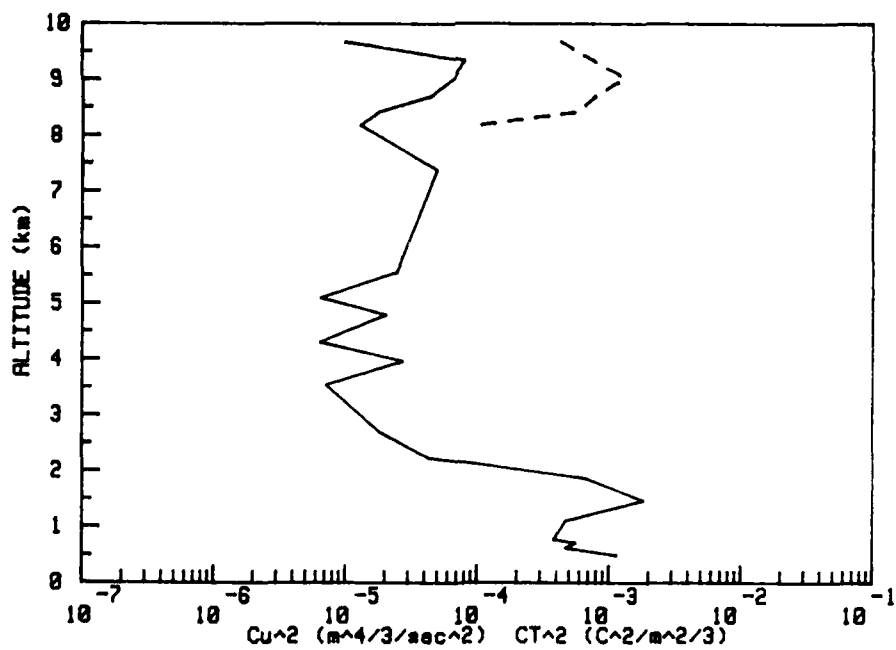
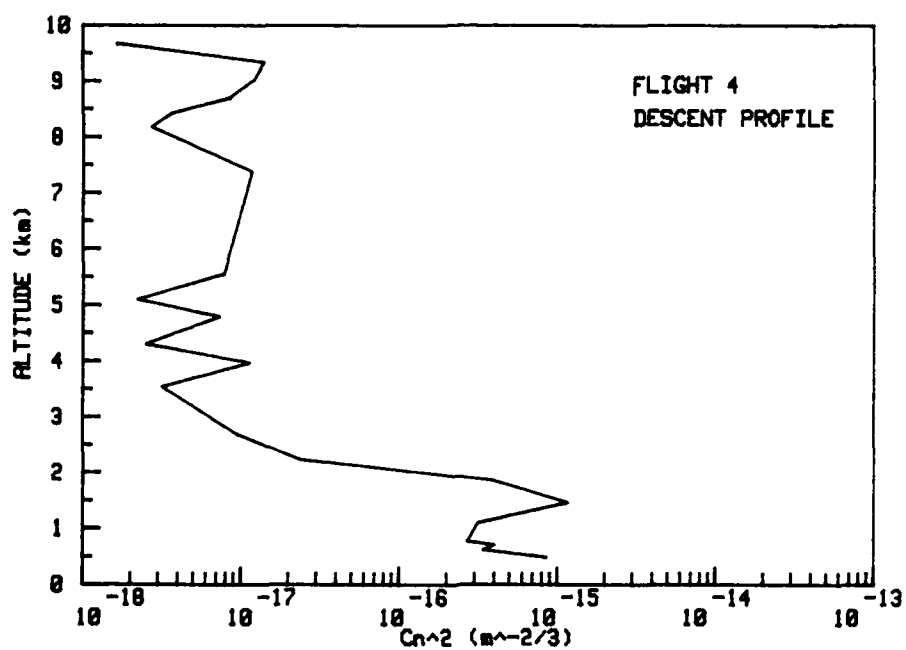


Figure 15. (continued)

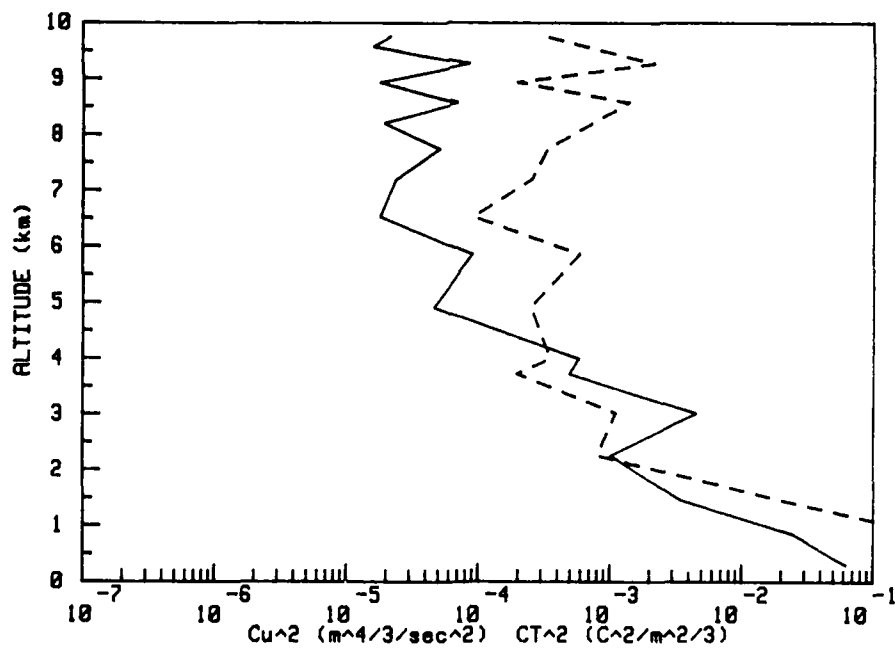
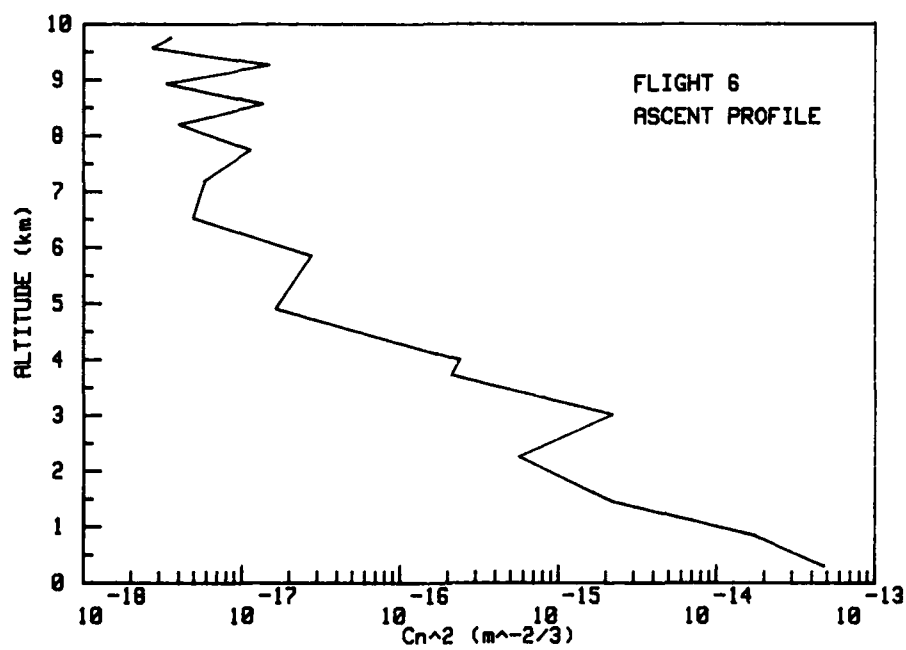


Figure 15. (continued)

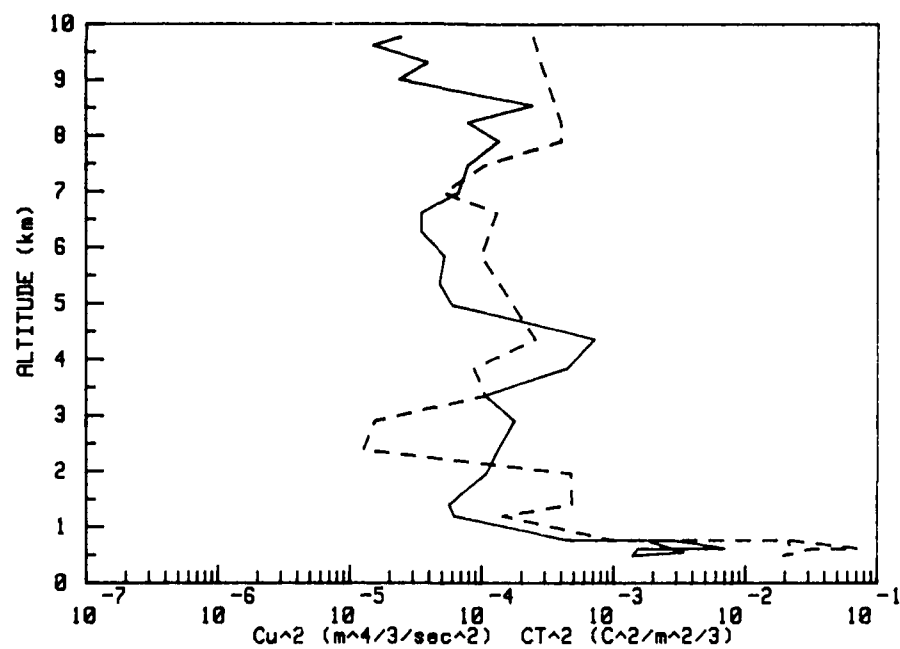
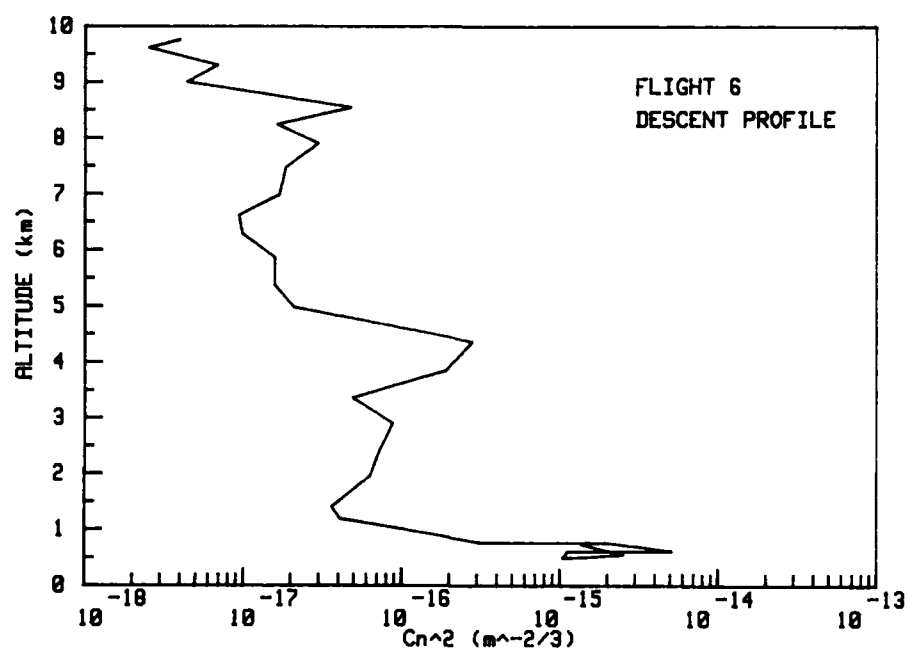


Figure 15. (continued)

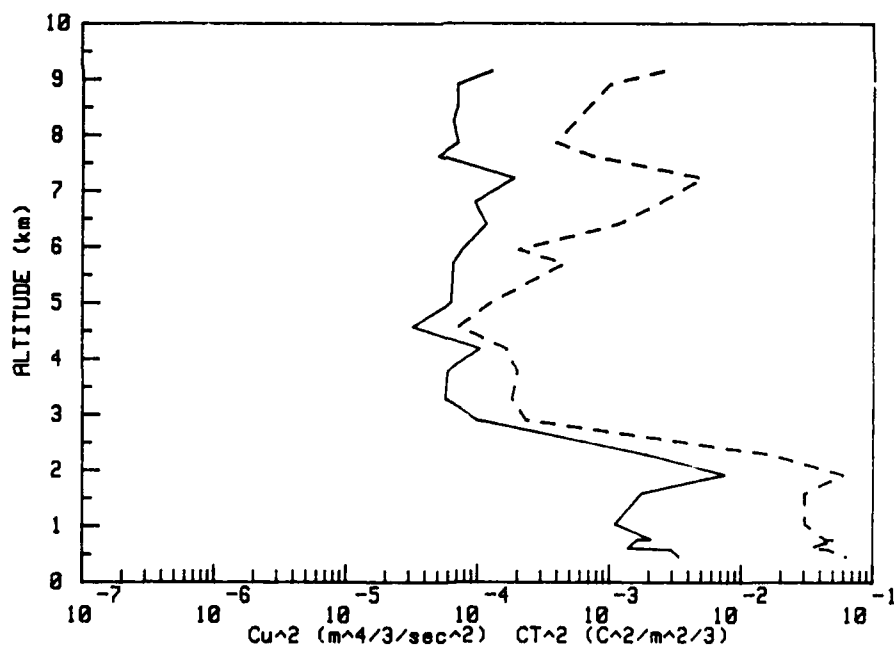
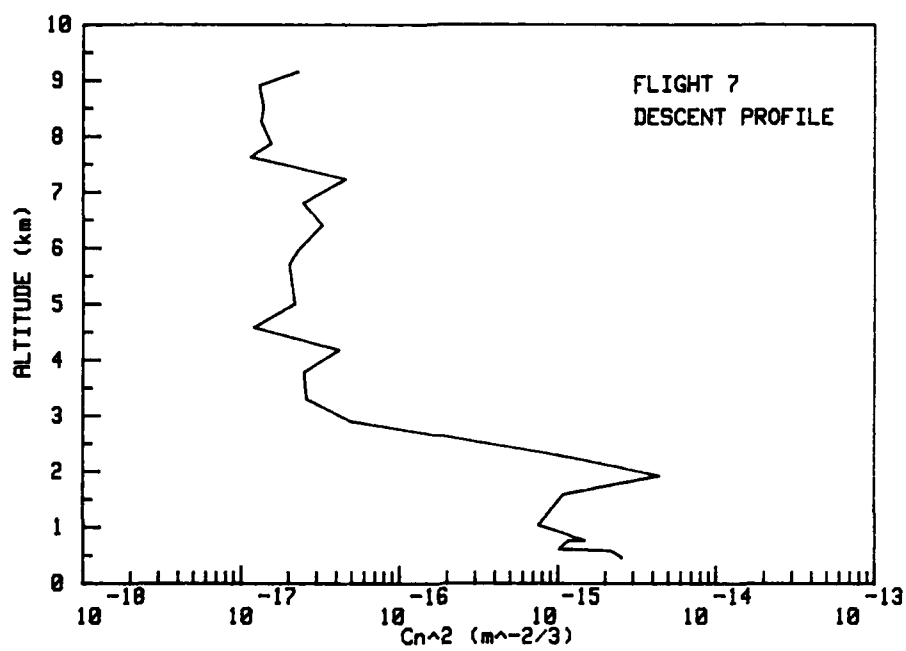


Figure 15. (continued)

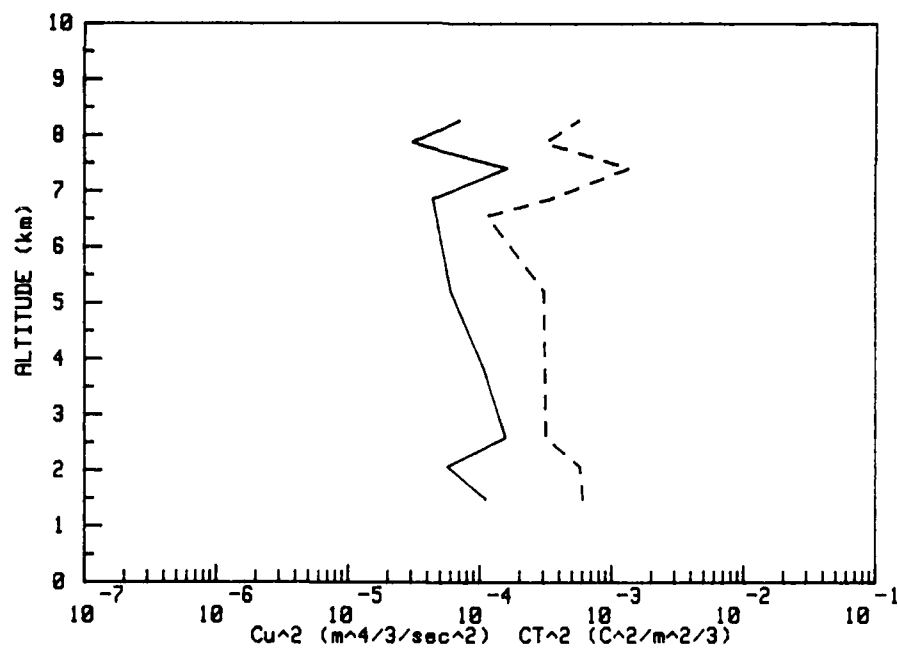
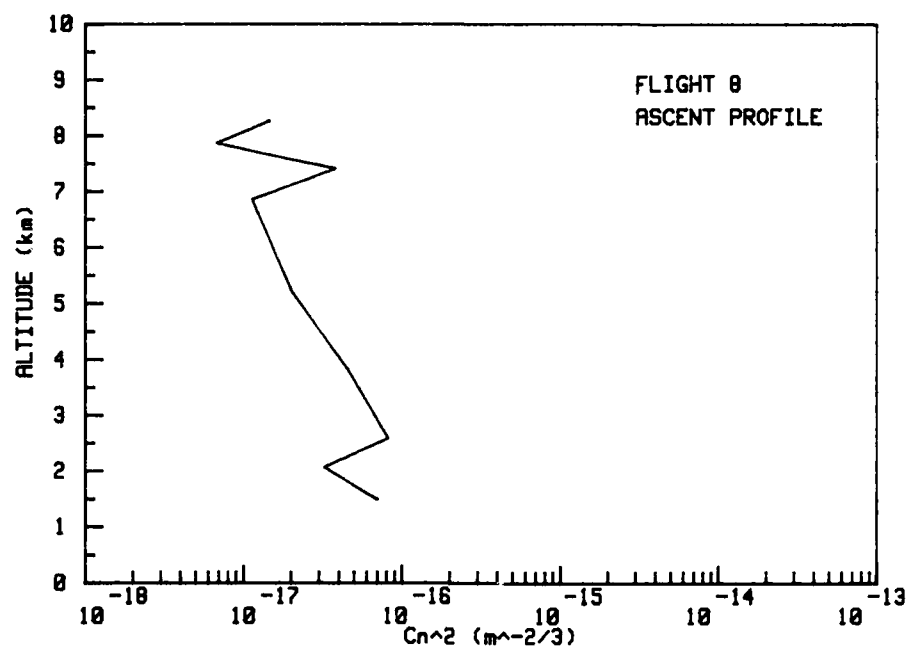


Figure 15. (continued)

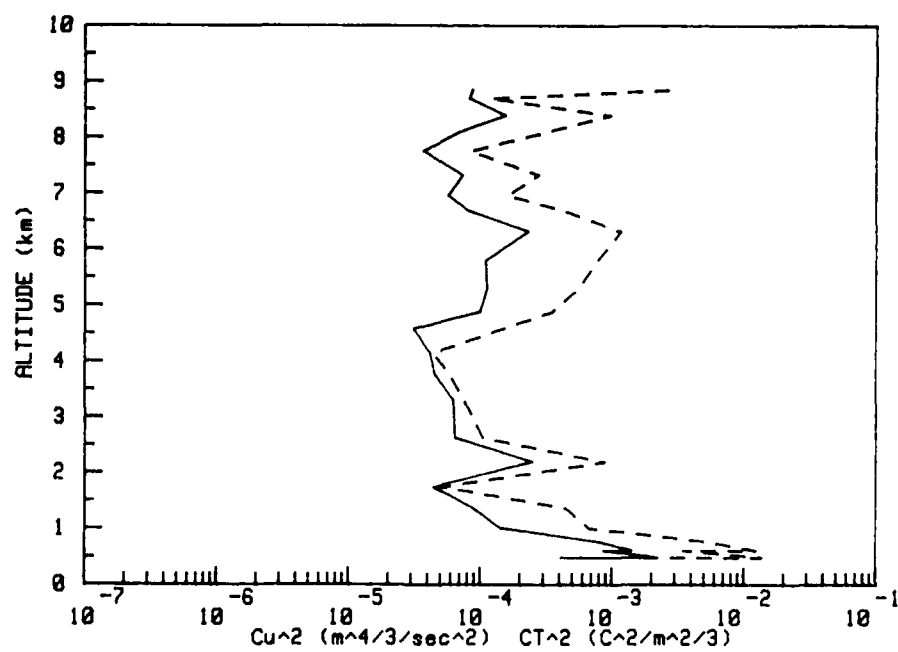
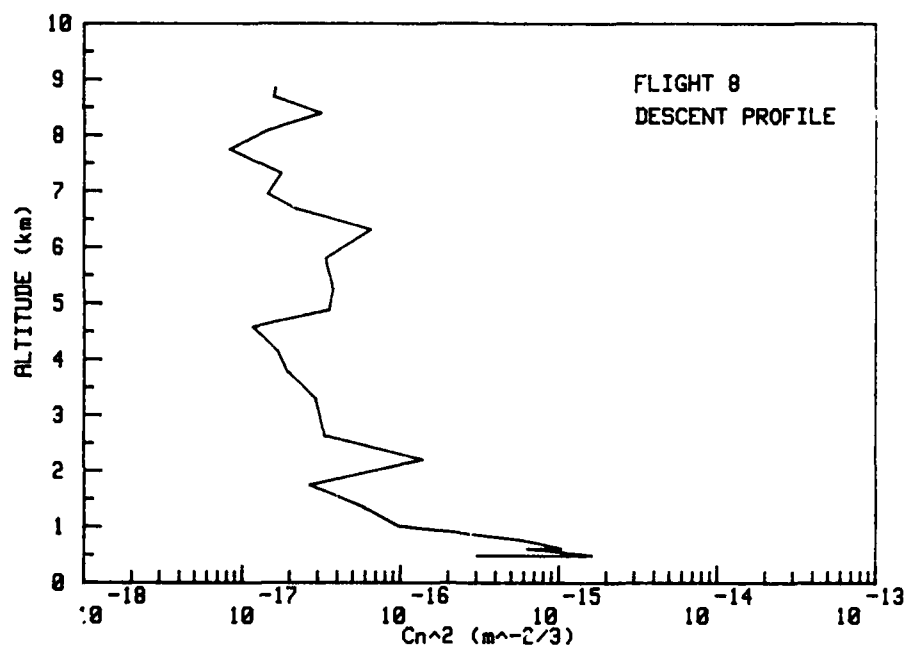


Figure 15. (continued)

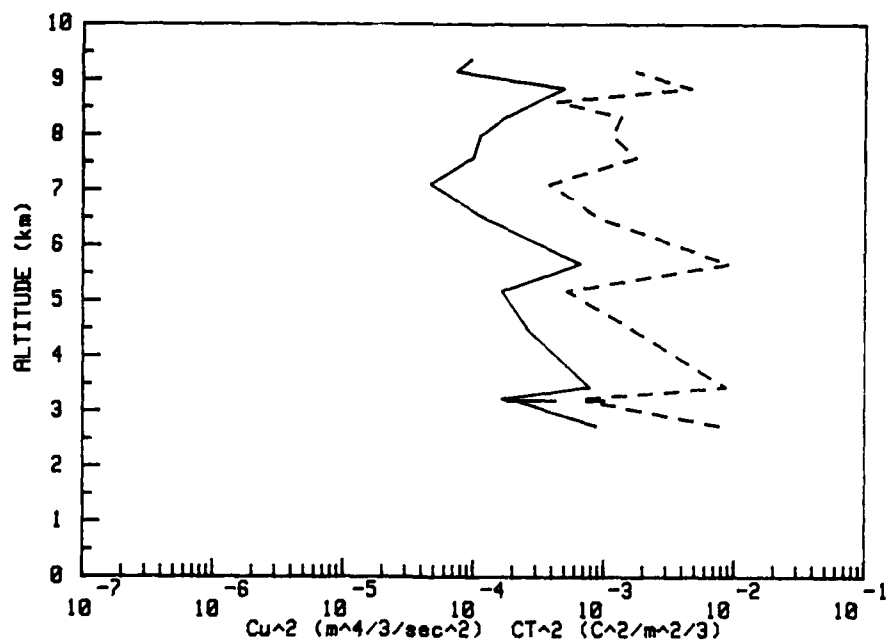
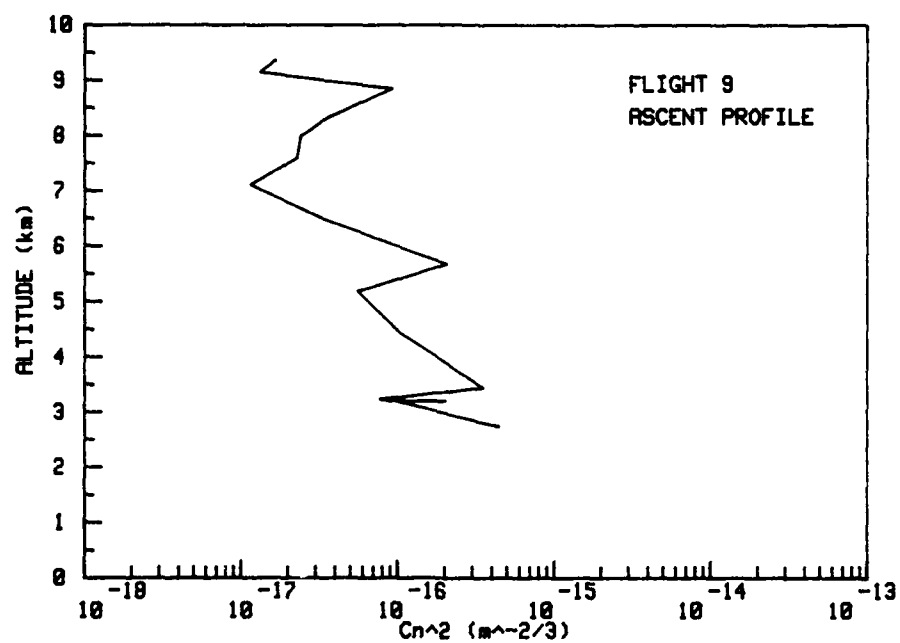


Figure 15. (continued)

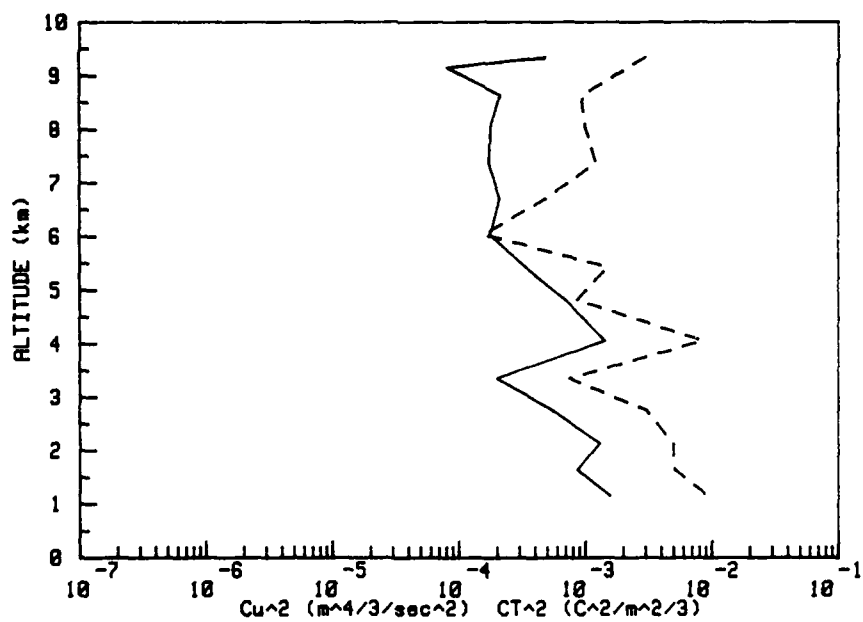
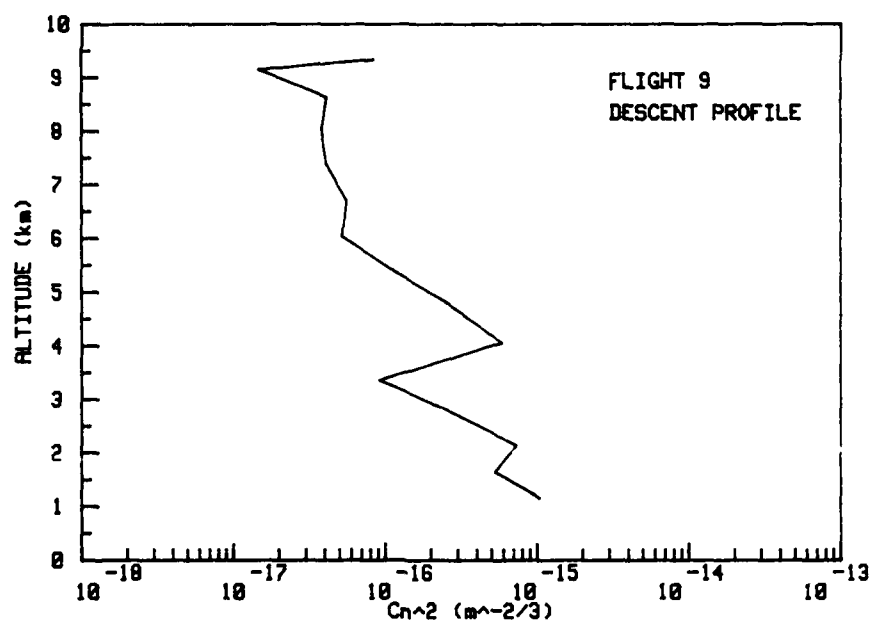


Figure 15. (continued)

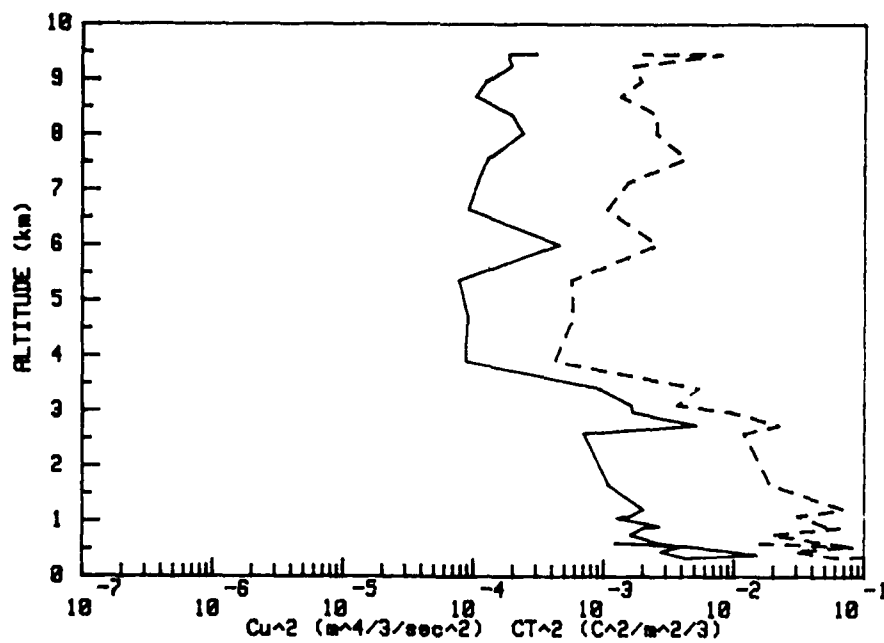
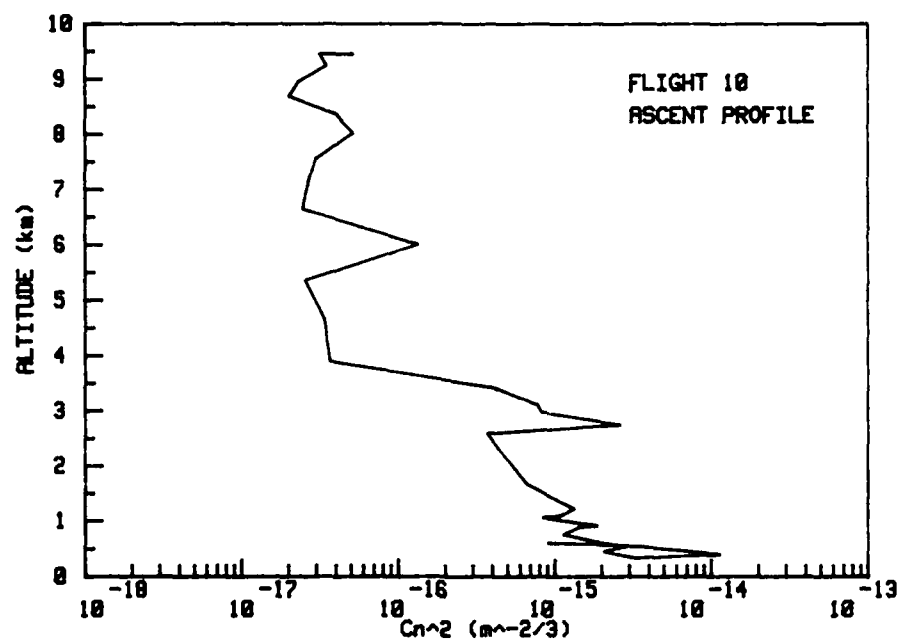


Figure 15. (continued)

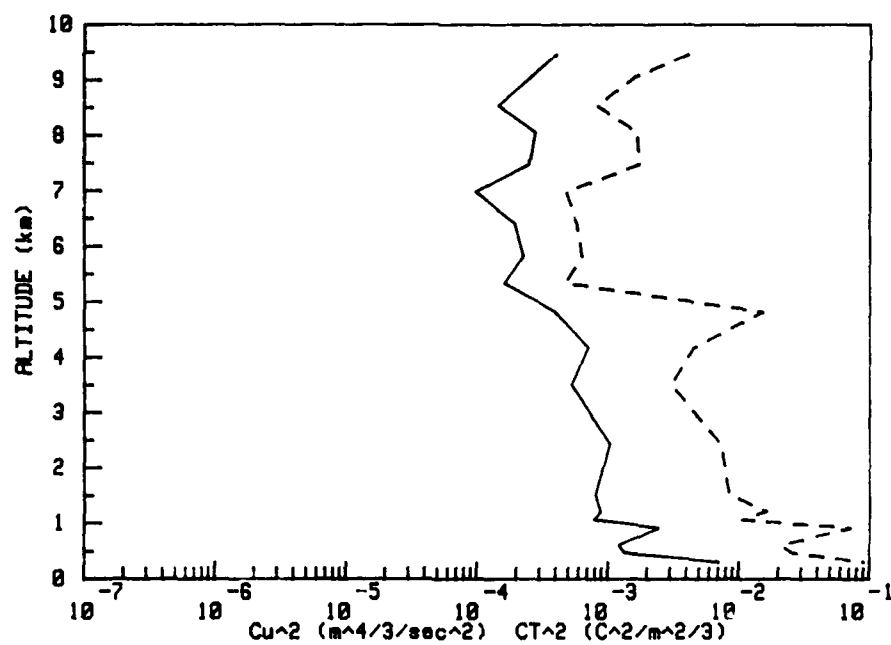
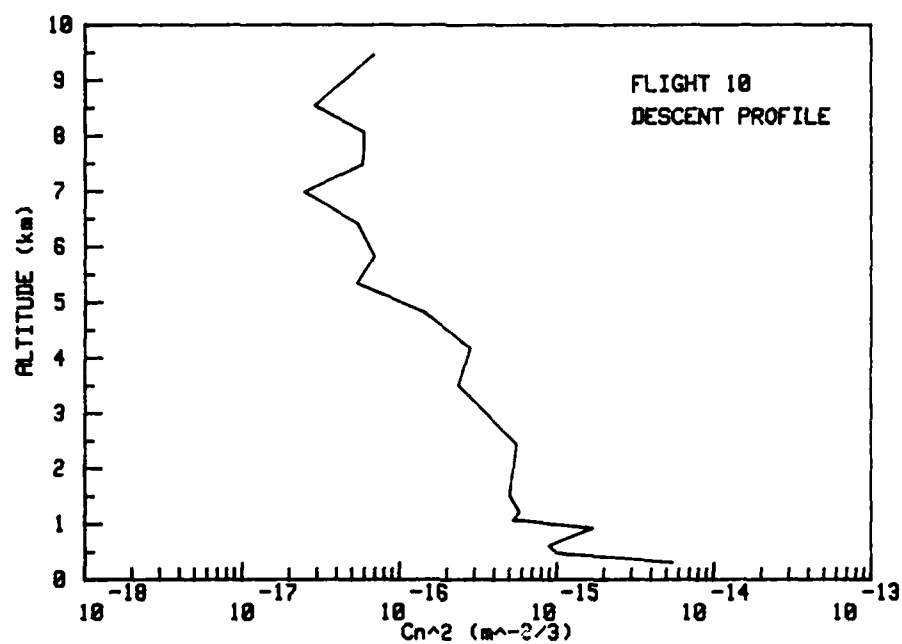


Figure 15. (continued)

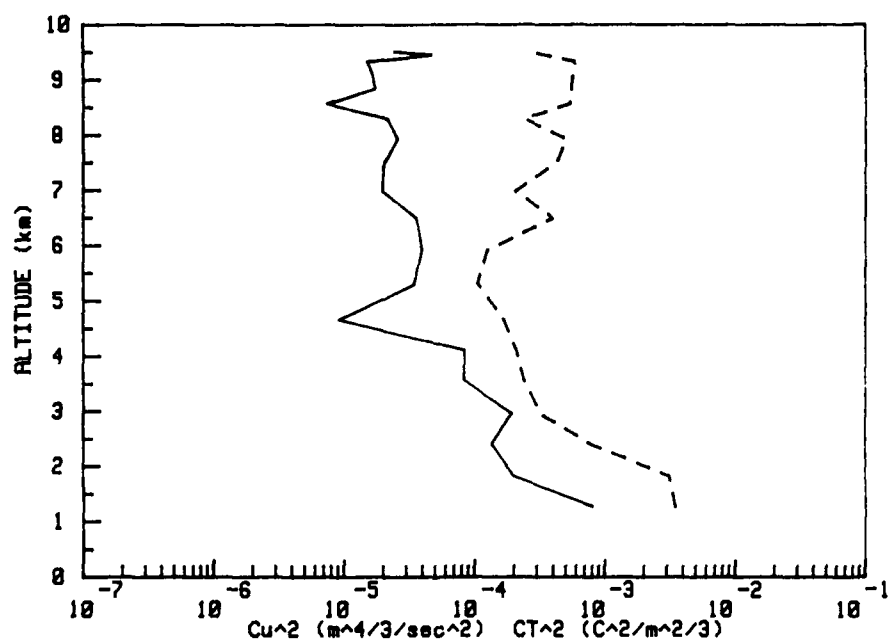
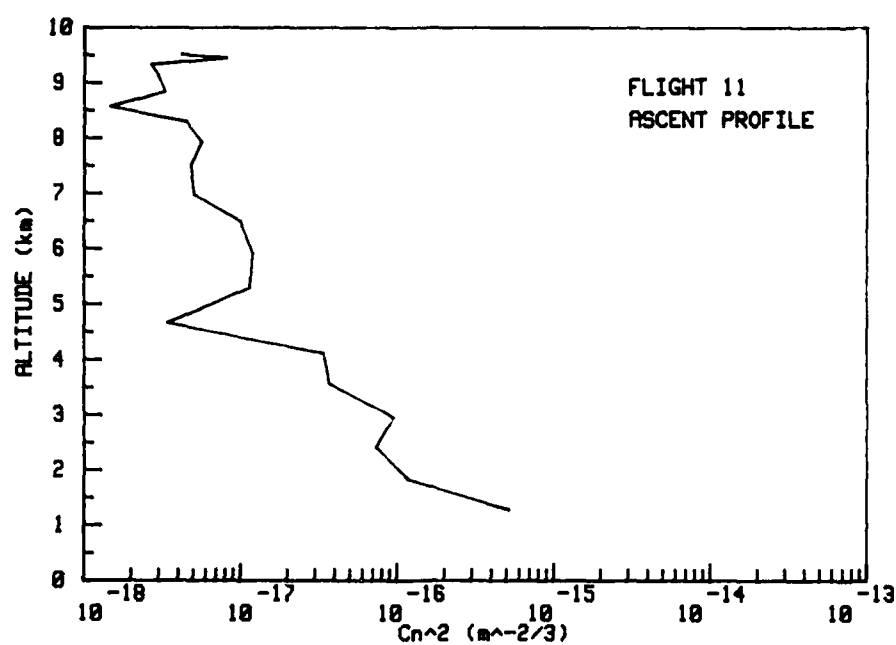


Figure 15. (continued)

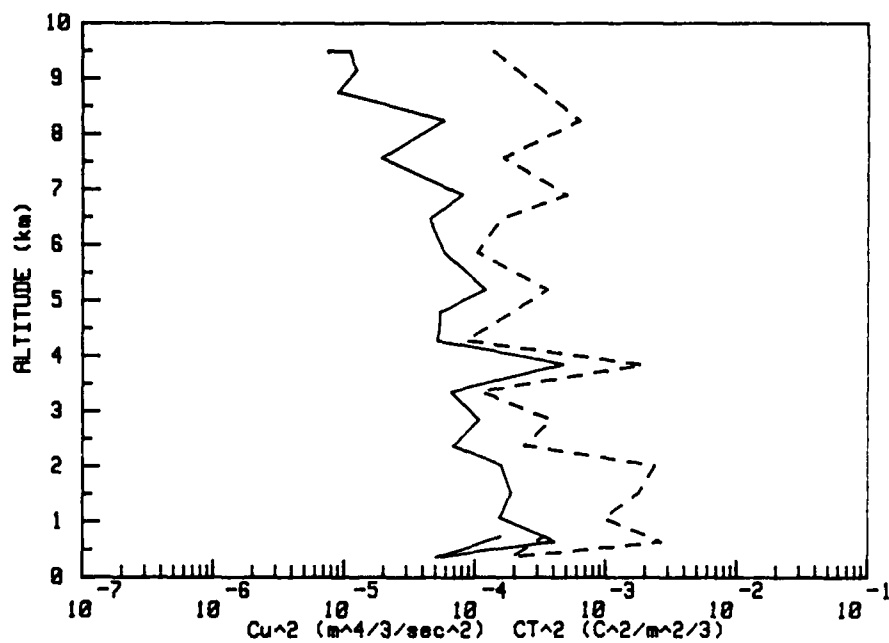
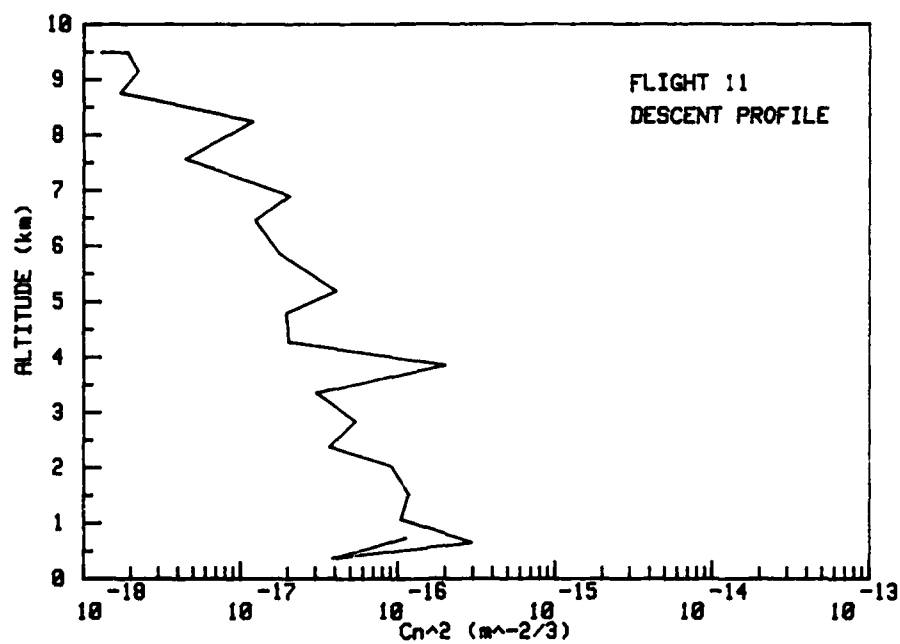


Figure 15. (continued)

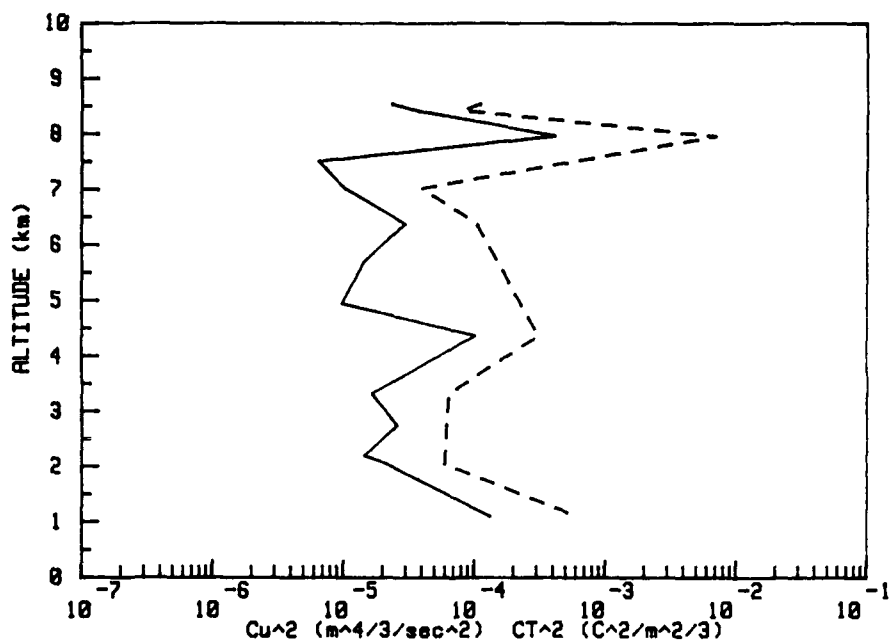
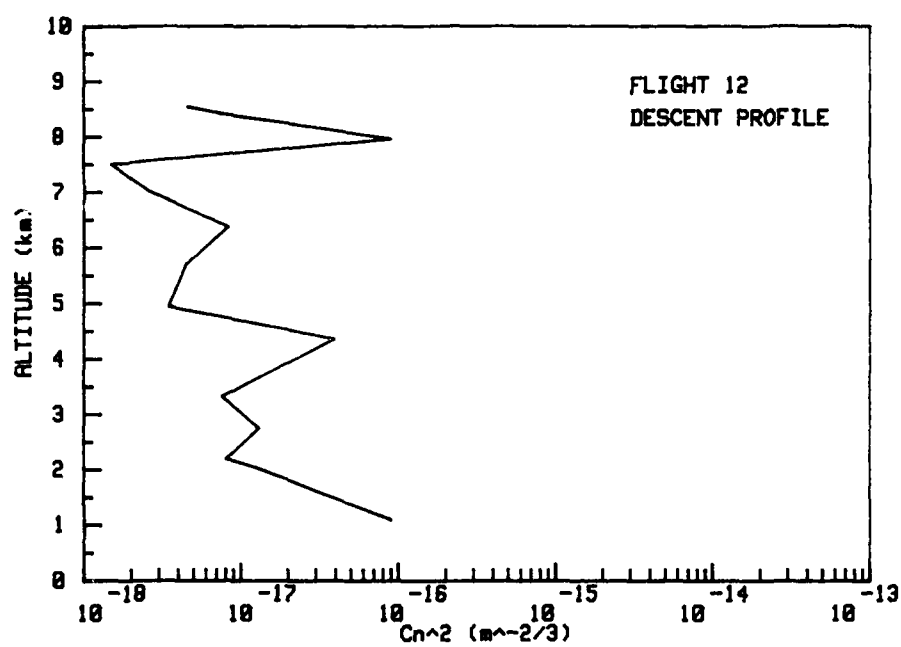


Figure 15. (continued)

Table 3.
Estimates of the height of the PBL based on the strength of the
signal-to-noise ratio exhibited in the spectra.

<u>Flight</u>	PBL Height (<u>MSL</u> <u>km</u>)
2	1.3
3	2.3
4	1.5
6	2.2
7	2.2
8	2.4
9	2.2
10	2.8
11	2
12	1

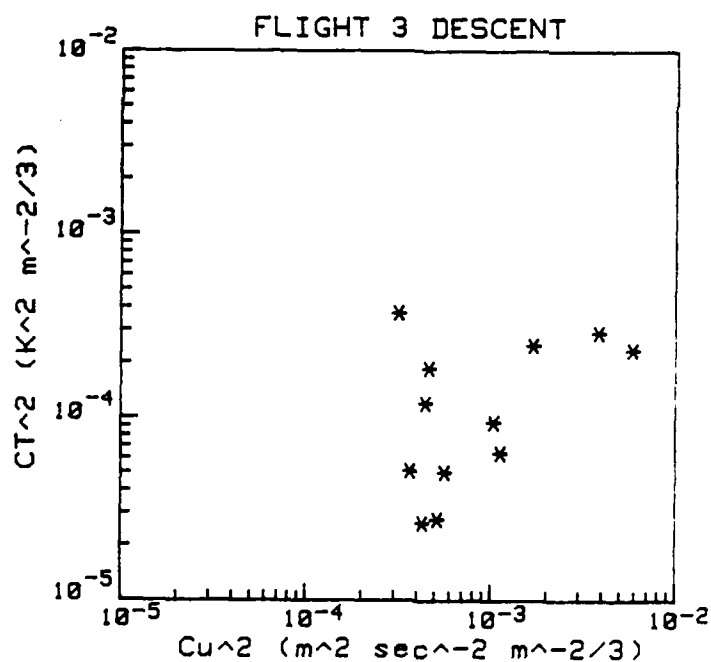
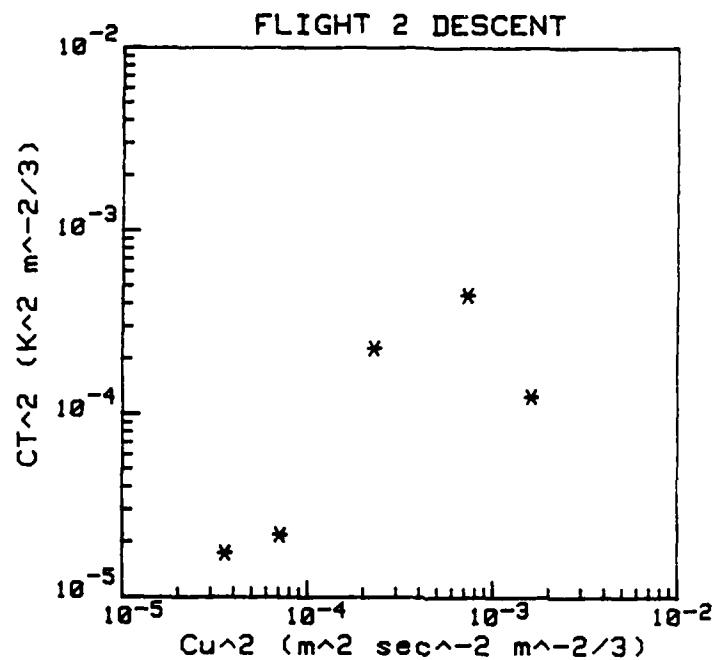


Figure 16. A comparison for each vertical flight of C_T^2 versus C_u^2 for spectra above the PBL. Flights 2-12 are shown (labeled above each graph).

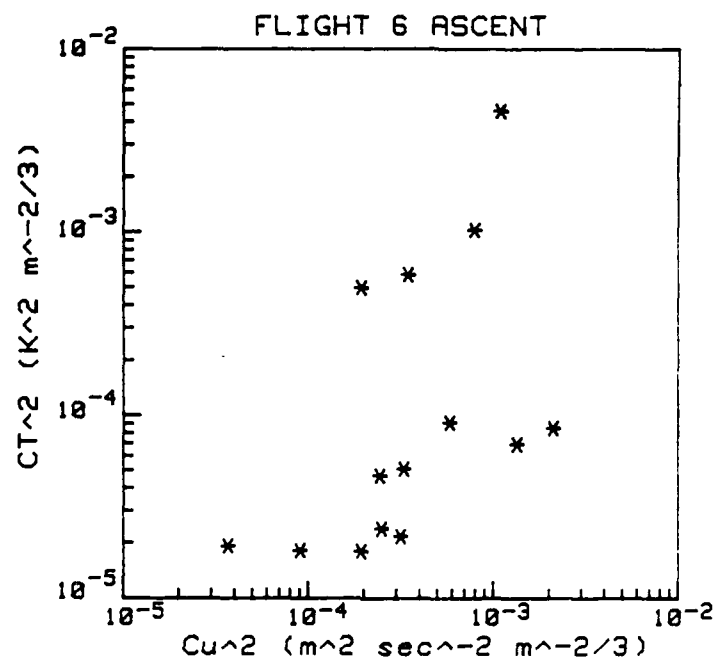
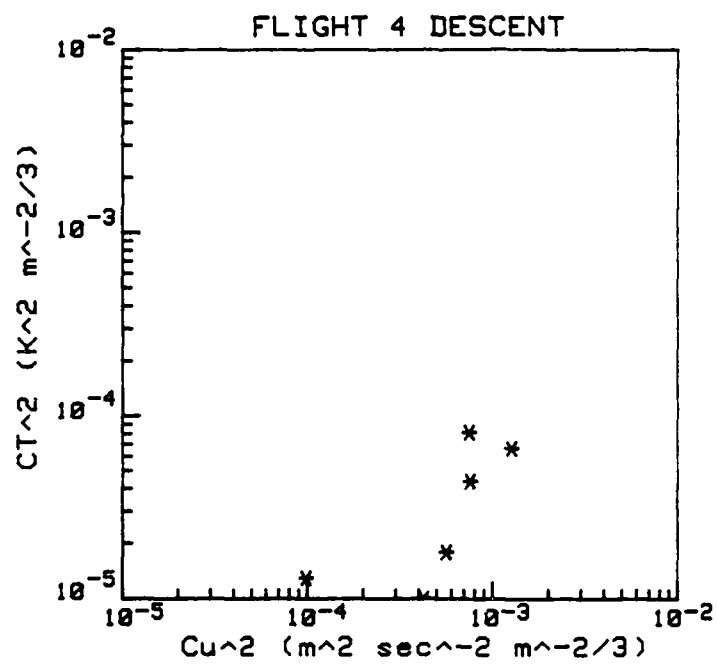


Figure 16. (continued)

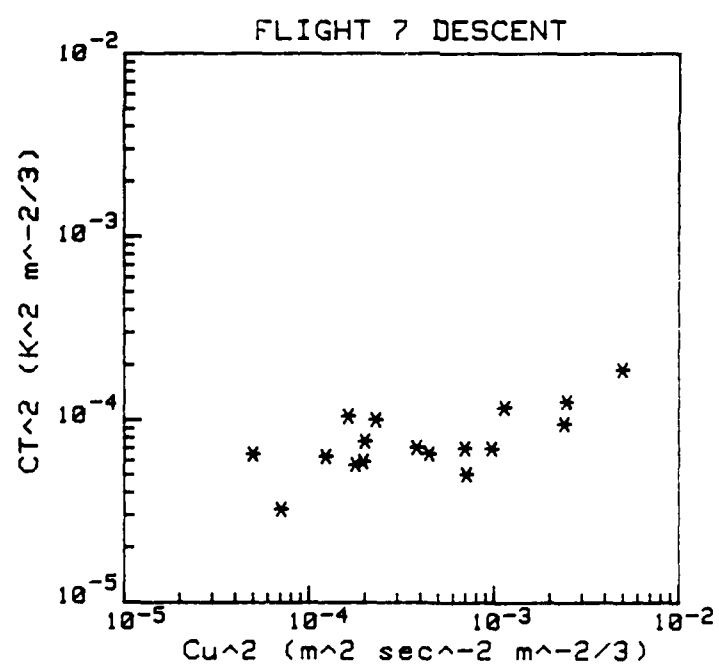
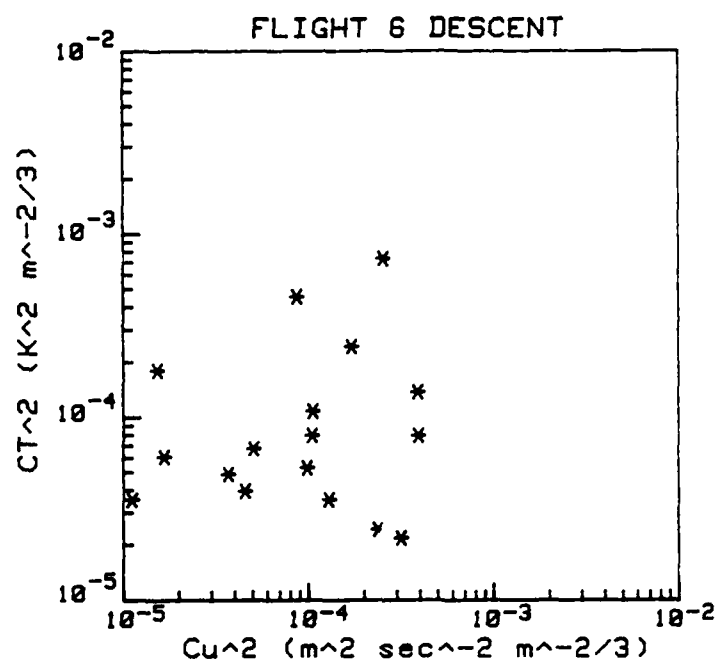


Figure 16. (continued)

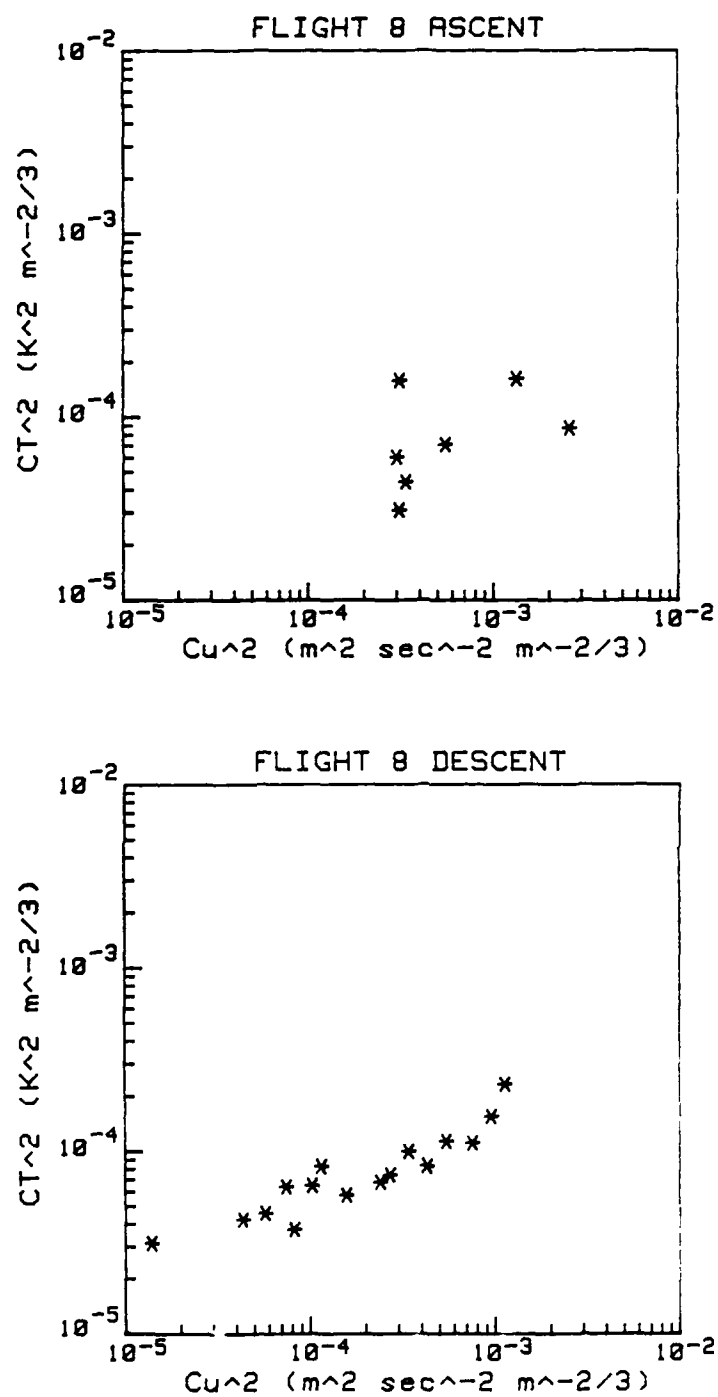


Figure 16. (continued)

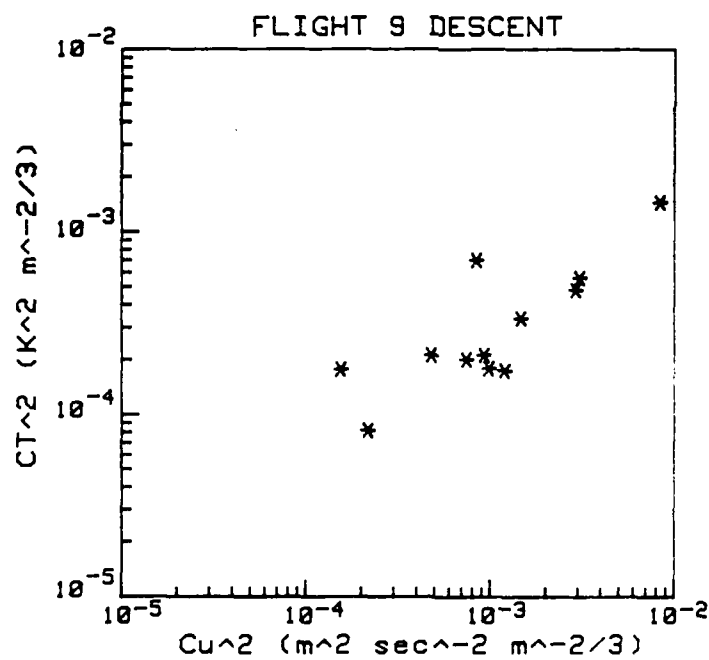
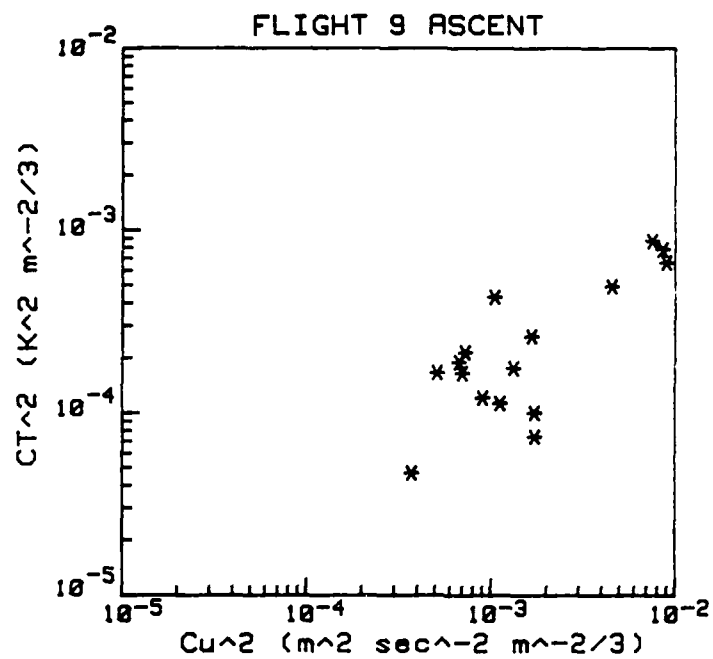


Figure 16. (continued)

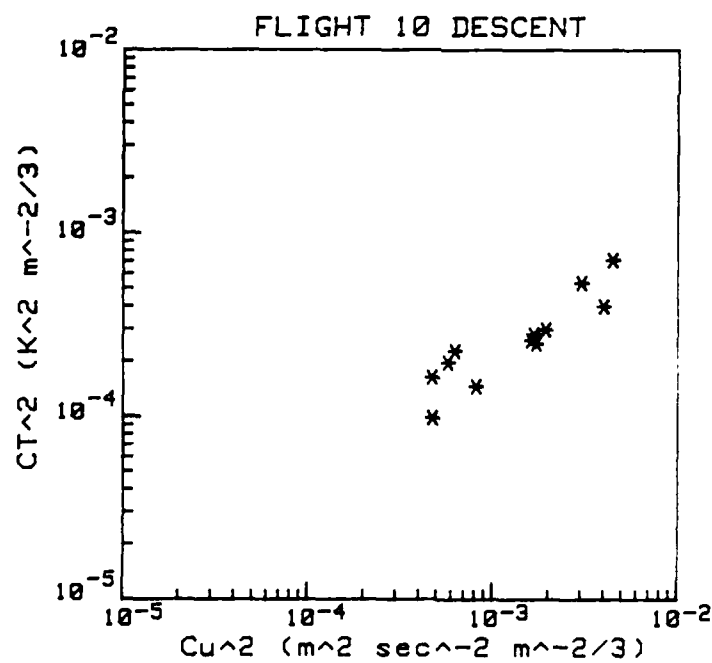
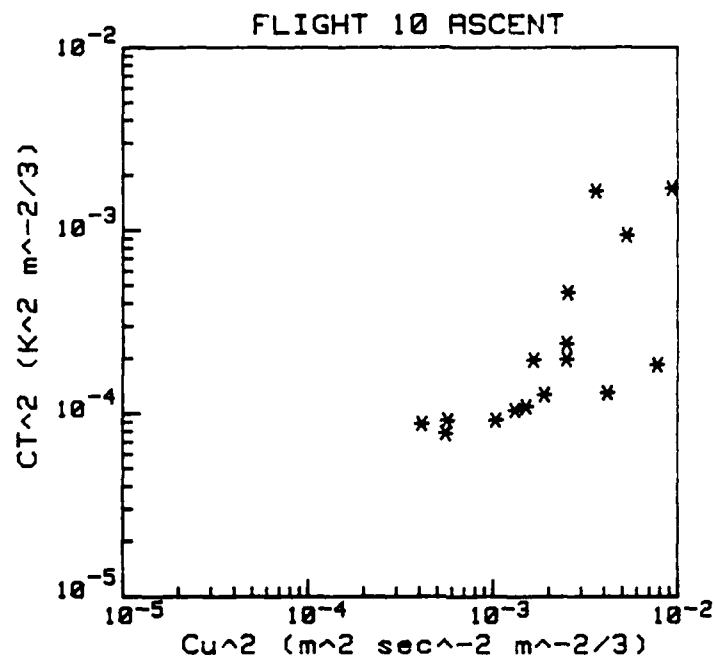


Figure 16. (continued)

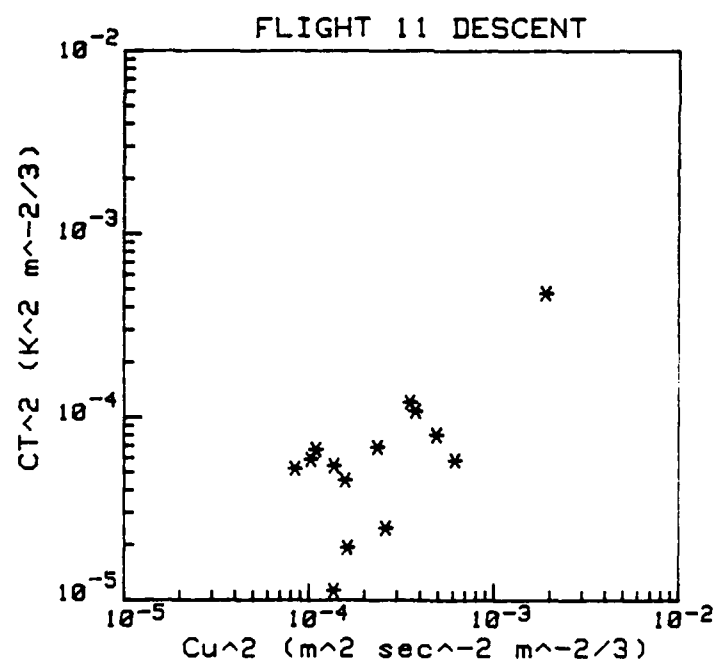
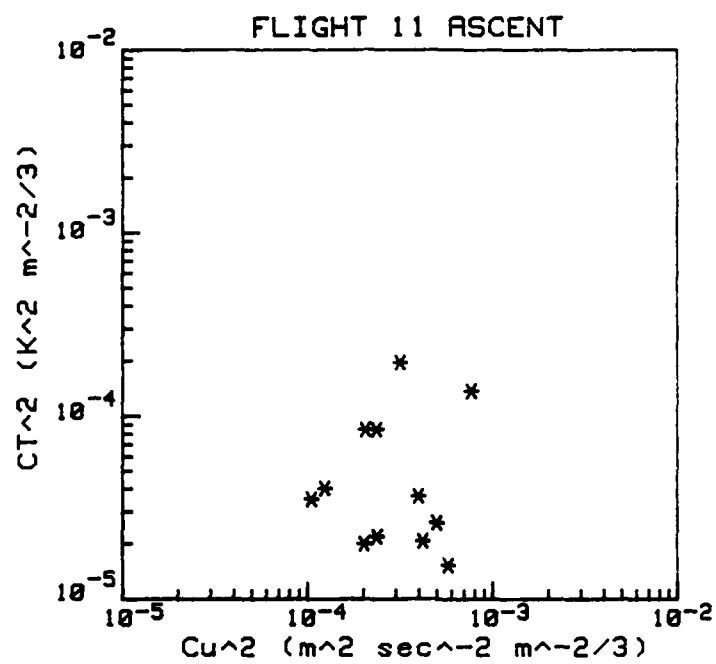


Figure 16. (continued)

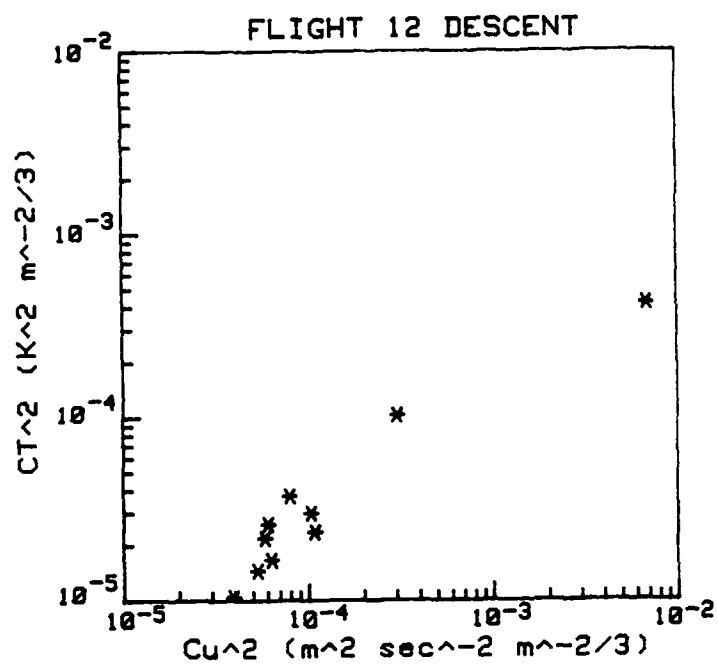


Figure 16. (continued)

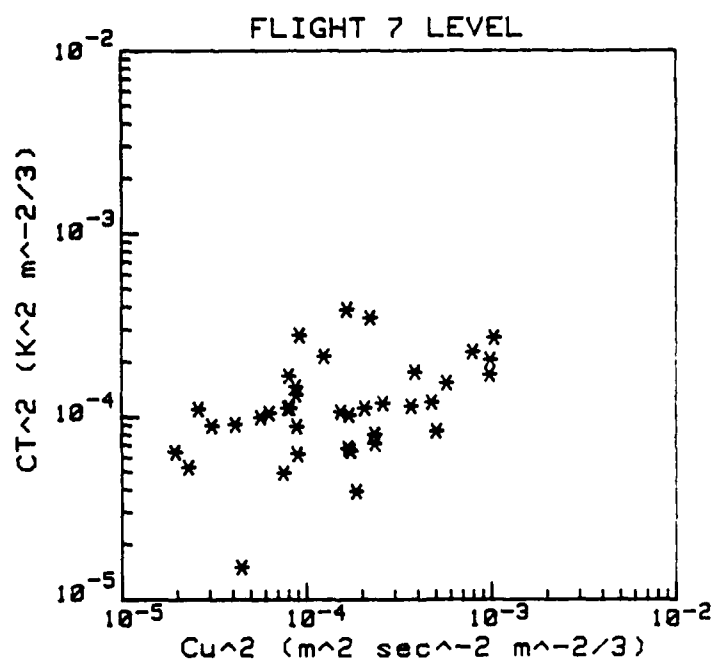
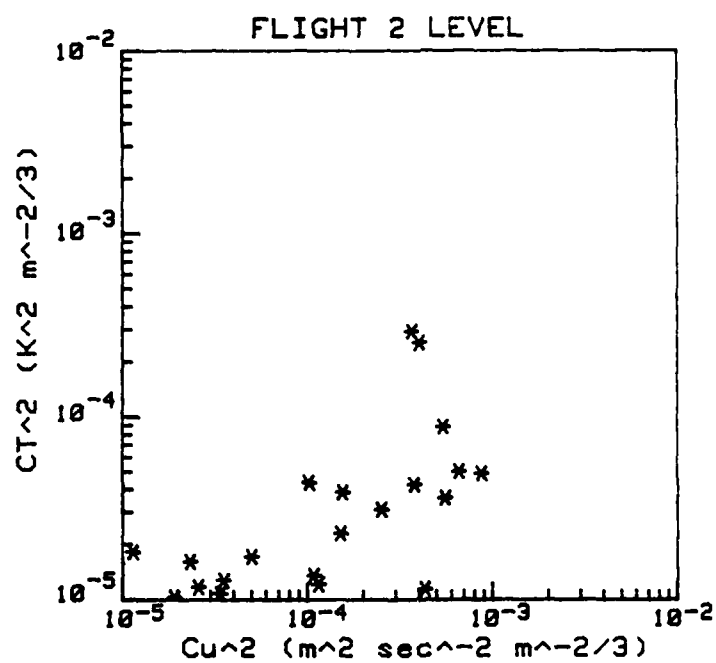


Figure 17. A comparison for each level flight of C_T^2 versus C_u^2 for spectra above the PBL. Flights 2, 7, 11, and 12 are shown (labeled above each graph).

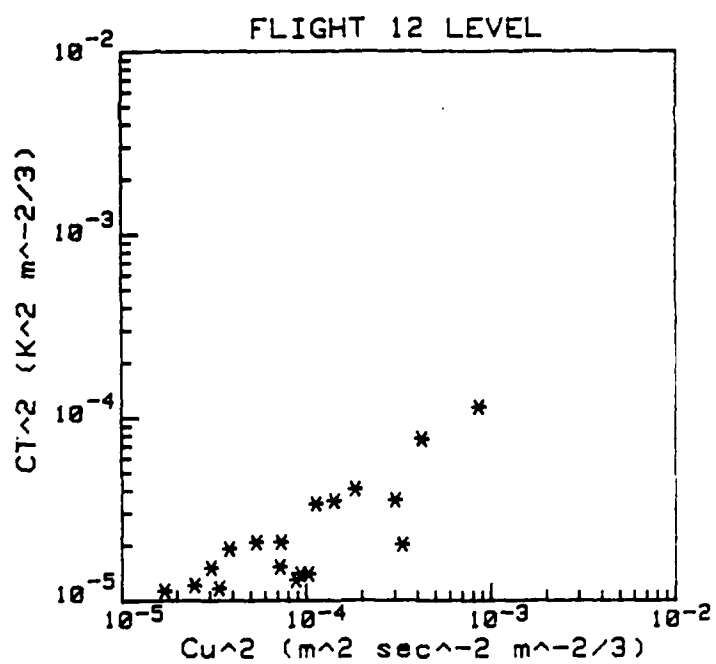
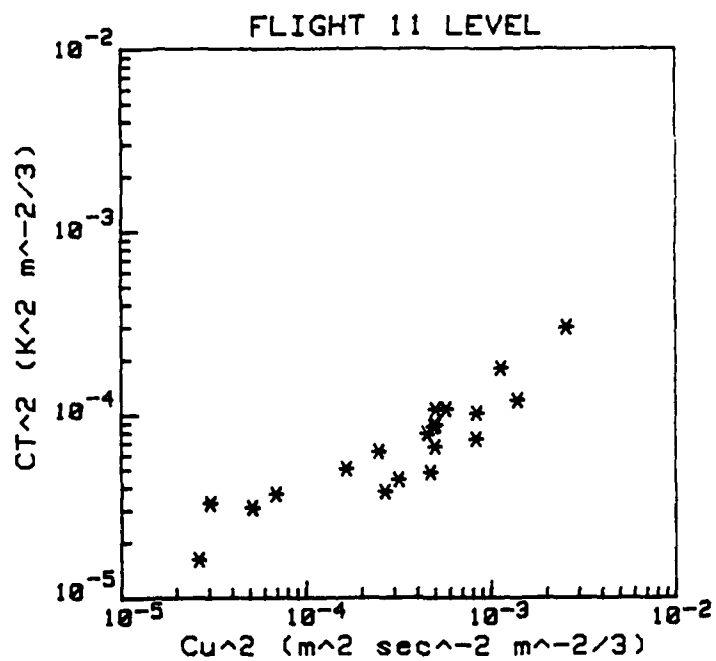


Figure 17. (continued)

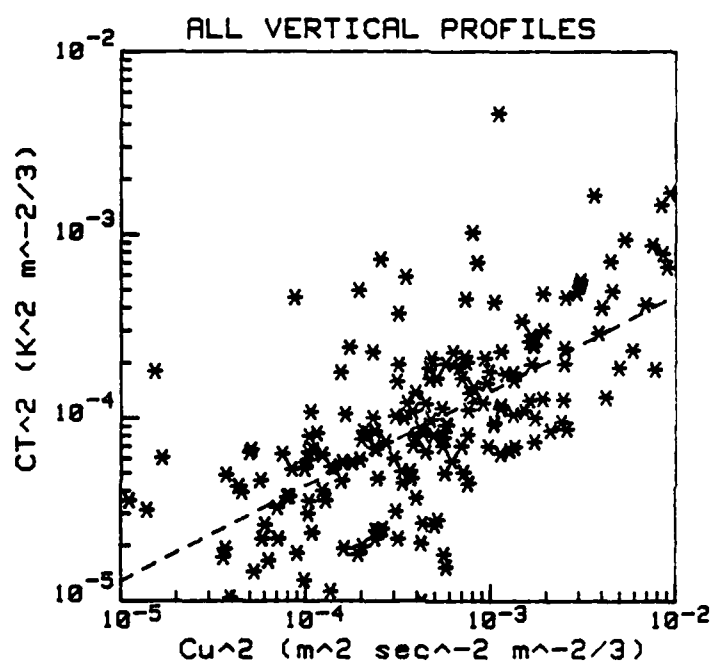
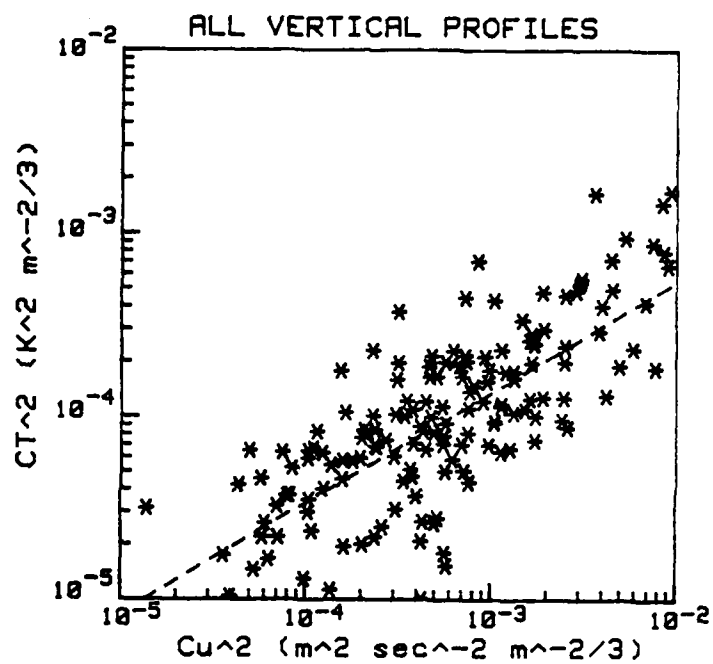


Figure 18. A composite comparison of C_T^2 versus C_u^2 for all vertical profiles. The broken line represents a regression analysis. Slope and correlation coefficient are given below each graph.



Excluding flight 6
Slope = .605
Correlation Coefficient = .749

Figure 18. (continued)

increased correlation of the entire data base (Figure 18). The slope for all the vertical profiles was close to 3/5. Correlation and slope for all the level flights showed approximately the same scatter (correlation) and slope as the vertical profiles (Figure 19).

In Figure 20, C_T^2 was plotted versus C_u^2 multiplied by

$$\theta/g (\partial\theta/\partial z) = T/g (\partial T/\partial z + \Gamma) \quad (7.1)$$

for all vertical flights (having associated temperature profiles). Again, flight 6 had high scatter and flight 7 showed little slope. A combined plot of all flights showed slightly higher correlation without flight 6 and again roughly a slope of 3/5 (Figure 20). This ratio corresponds to values of $1.6 R_i/(P_r - R_i)$ that range from 0.3 for high values of C_T^2 to as much as 10 for low values of C_T^2 .

As an additional comparison, $C_T^2 / (C_u^2 \theta/g \partial\theta/\partial z)$ was plotted against a turbulence activity parameter (Gregg 1987), $\epsilon/\nu N$ (Figure 21). N was calculated as $g \partial \ln \theta / \partial z$ from a polynomial fit to the aircraft potential temperature profile. The formula used to derive kinematic viscosity was taken from the U. S. Standard Atmosphere Supplements, 1966 (Environmental Science Services Administration et al. 1966).

$$\mu = (\beta T^{3/2}) / (T + S) \quad (7.2)$$

where μ is the dynamic viscosity, $\beta = 1.458E-6 \text{ kg sec}^{-1} \text{ m}^{-1} \text{ K}^{-1/2}$, and $S = 110.4 \text{ Kelvin}$. Kinematic viscosity, ν , equals μ/ρ . Density was calculated as $\rho = \rho_0 \exp(-Z/8 \text{ km})$ where ρ_0 is 1.225 kg m^{-3} . T was taken from the aircraft profiles. C_T^2 , C_u^2 , ϵ , and N

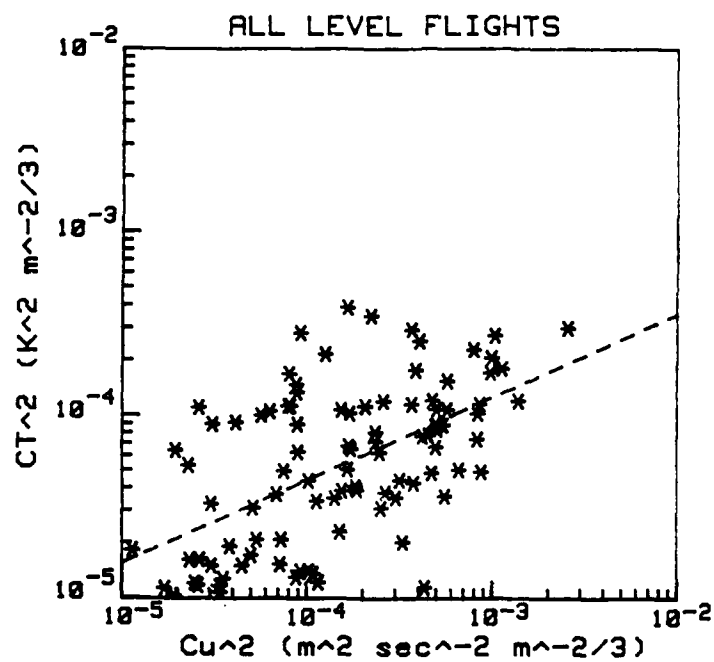
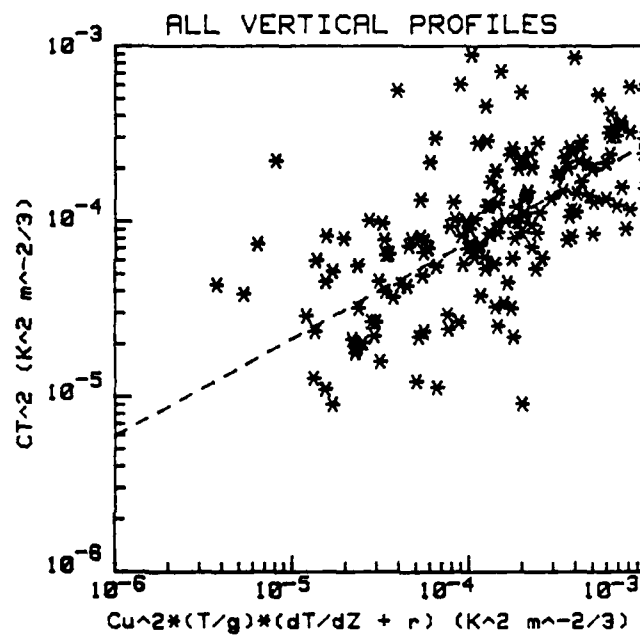
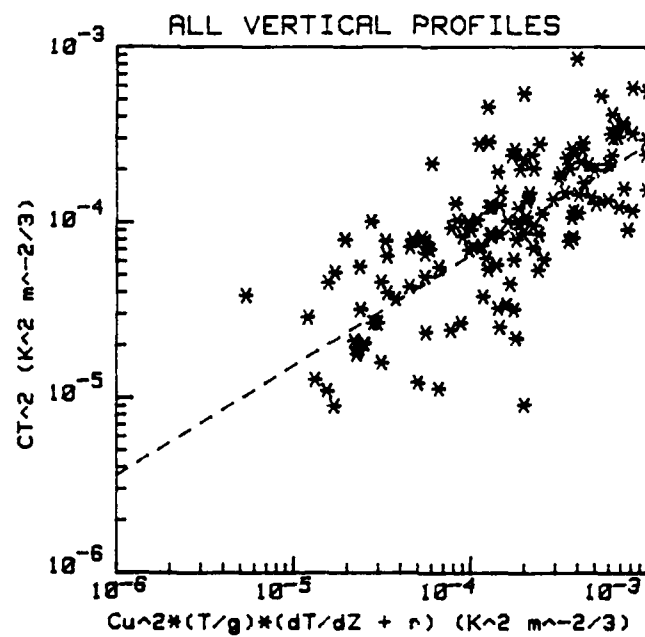


Figure 19. A composite comparison of C_T^2 versus C_u^2 for all level profiles. The broken line represents a regression analysis. Slope and correlation coefficient are given below each graph.



Slope = .554
Correlation Coefficient = .703

Figure 20. A composite comparison of C_T^2 versus C_u^2 normalized by the expression $[T/g (\partial T/\partial z + \Gamma)]$. The broken line represents a regression analysis. Slope and correlation coefficient are given below each graph.



Excluding flight 6
 Slope = .630
 Correlation Coefficient = .797

Figure 20. (continued)

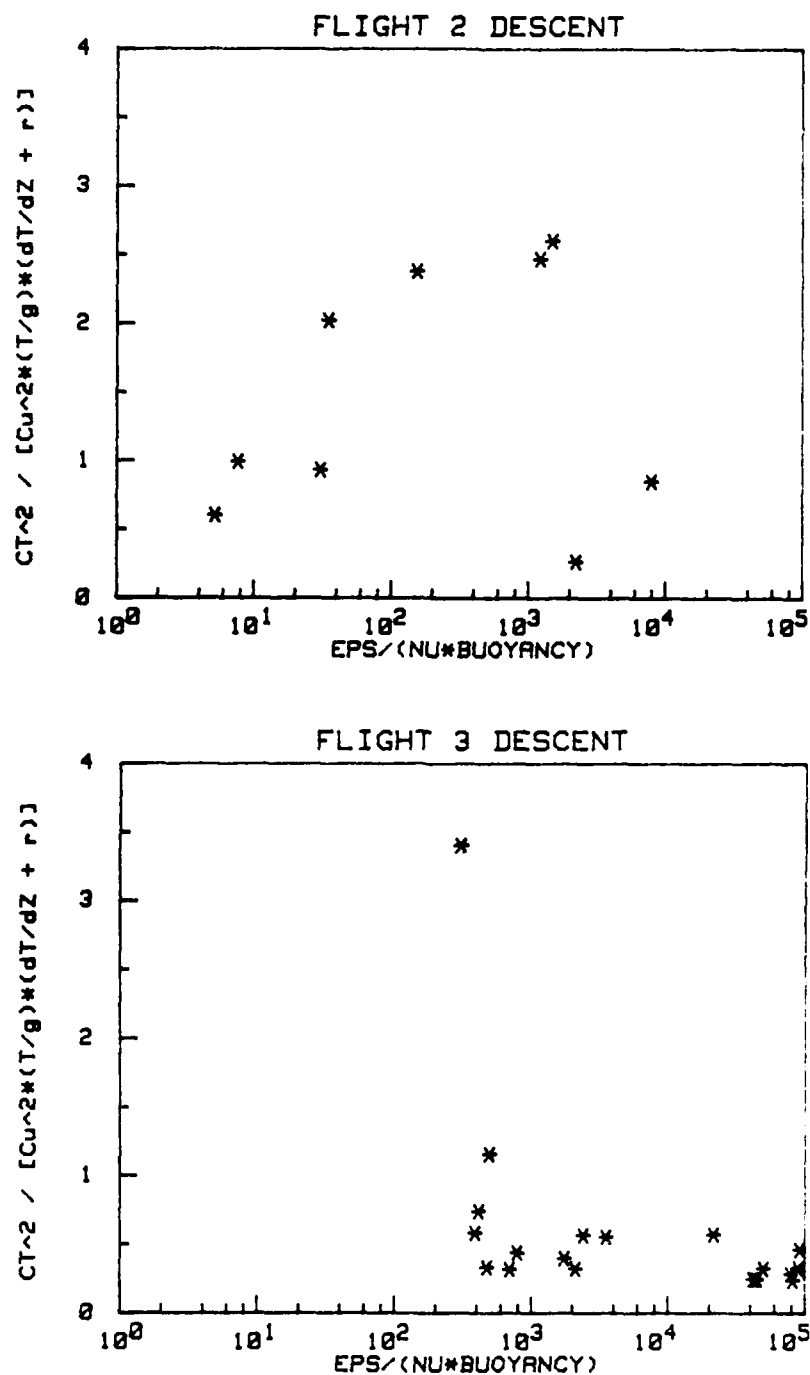


Figure 21. Comparison for each vertical profile of C_t^2 divided by C_u^2 normalized as in Figure 20 versus a turbulent activity parameter, $\epsilon/(\nu N)$. Flights 2-12 are shown (labeled above each graph).

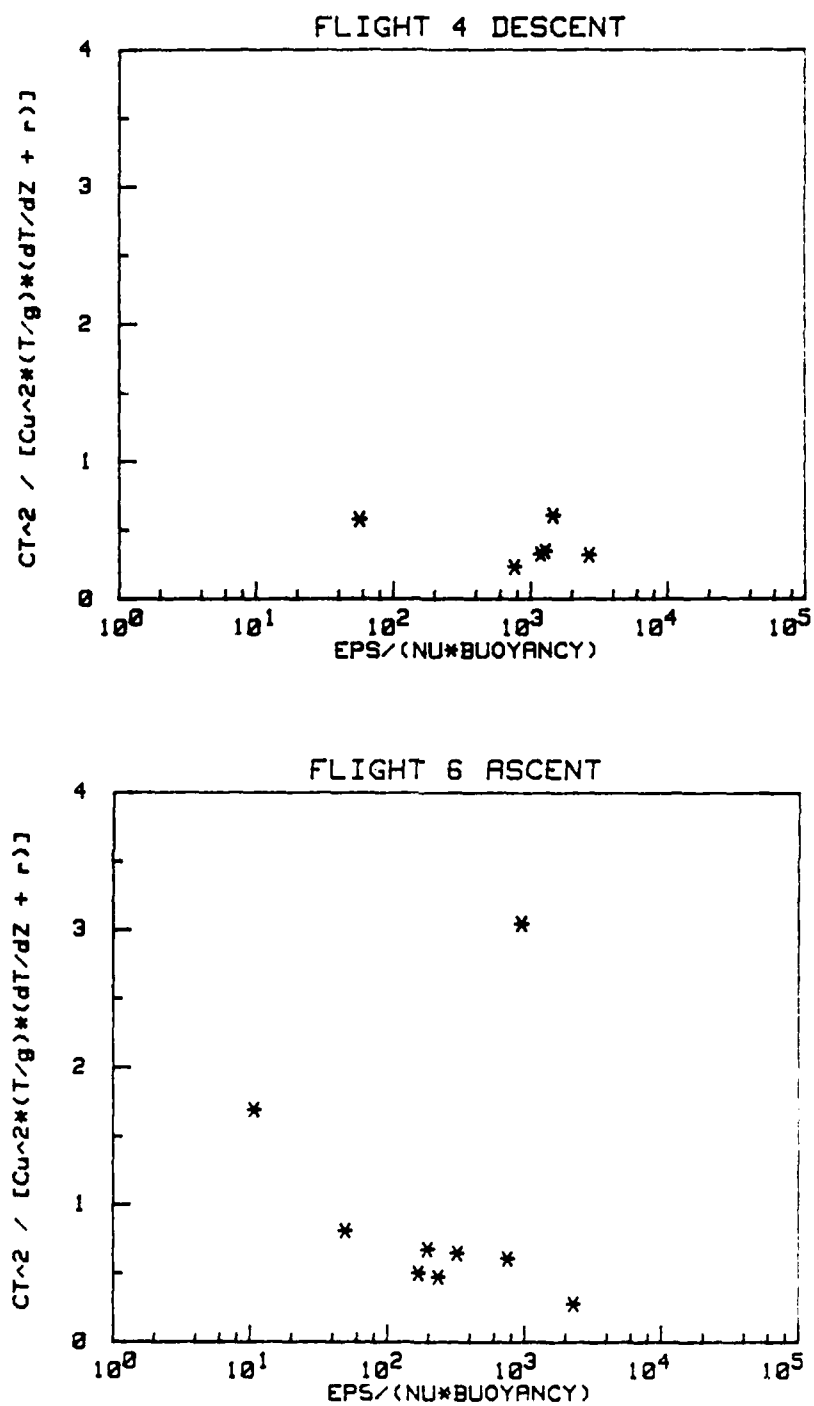


Figure 21. (continued)

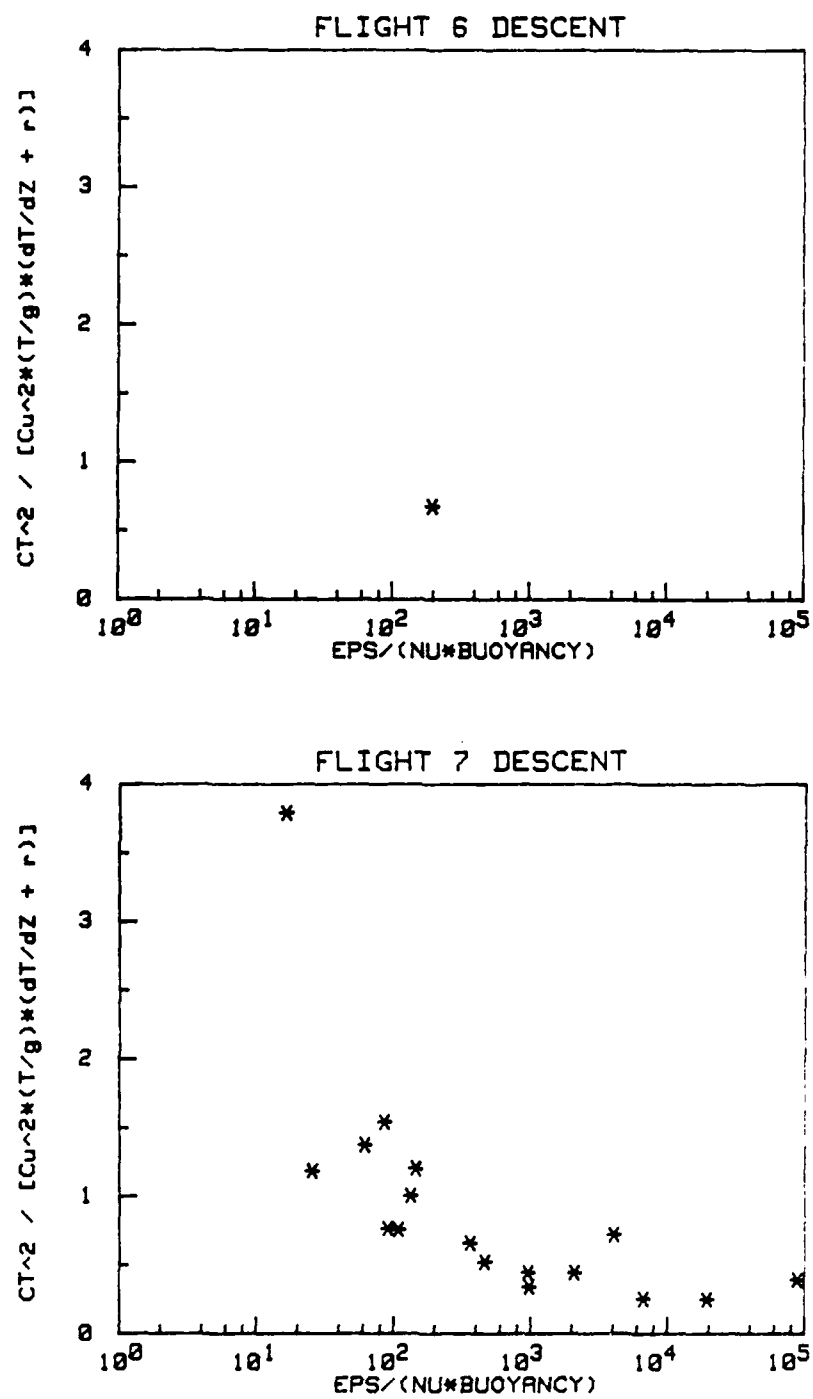


Figure 21. (continued)

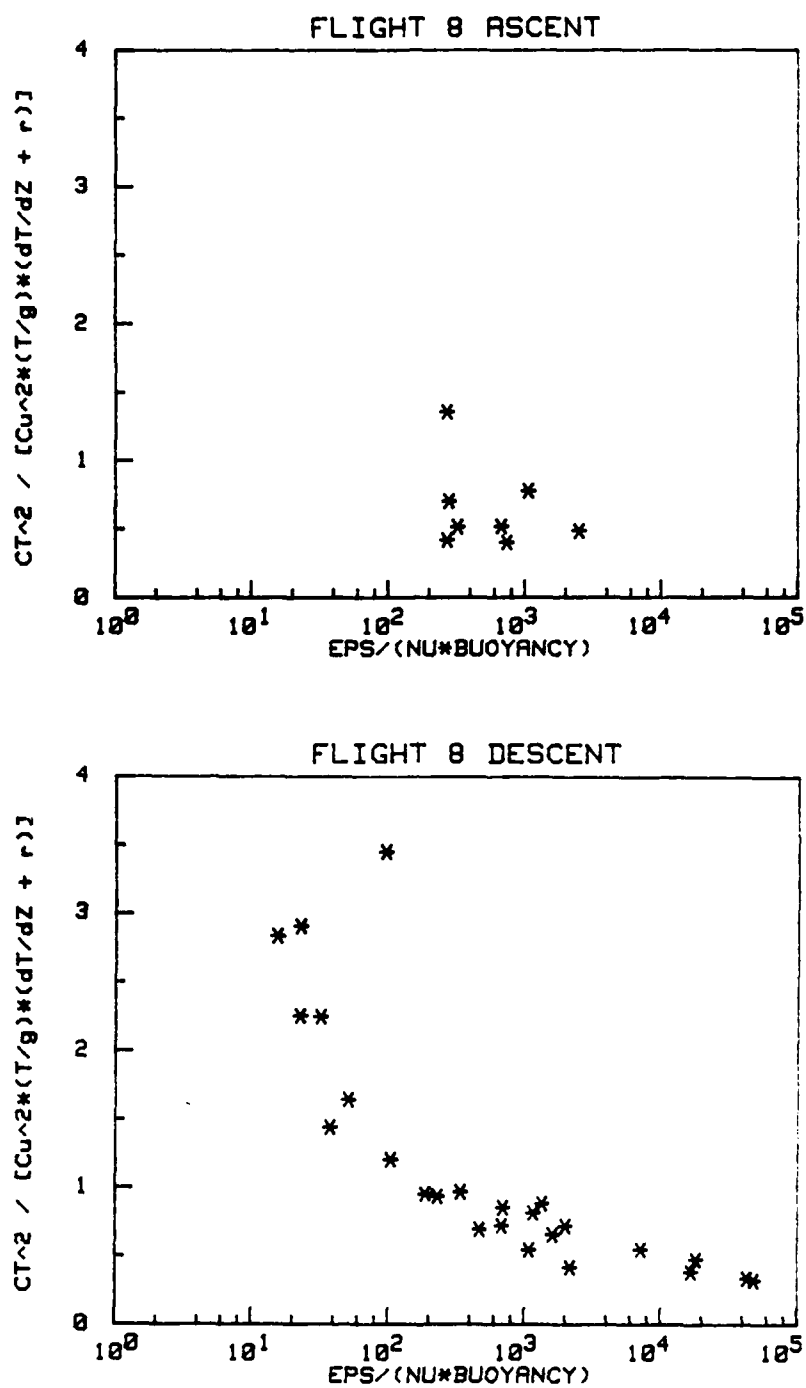


Figure 21. (continued)

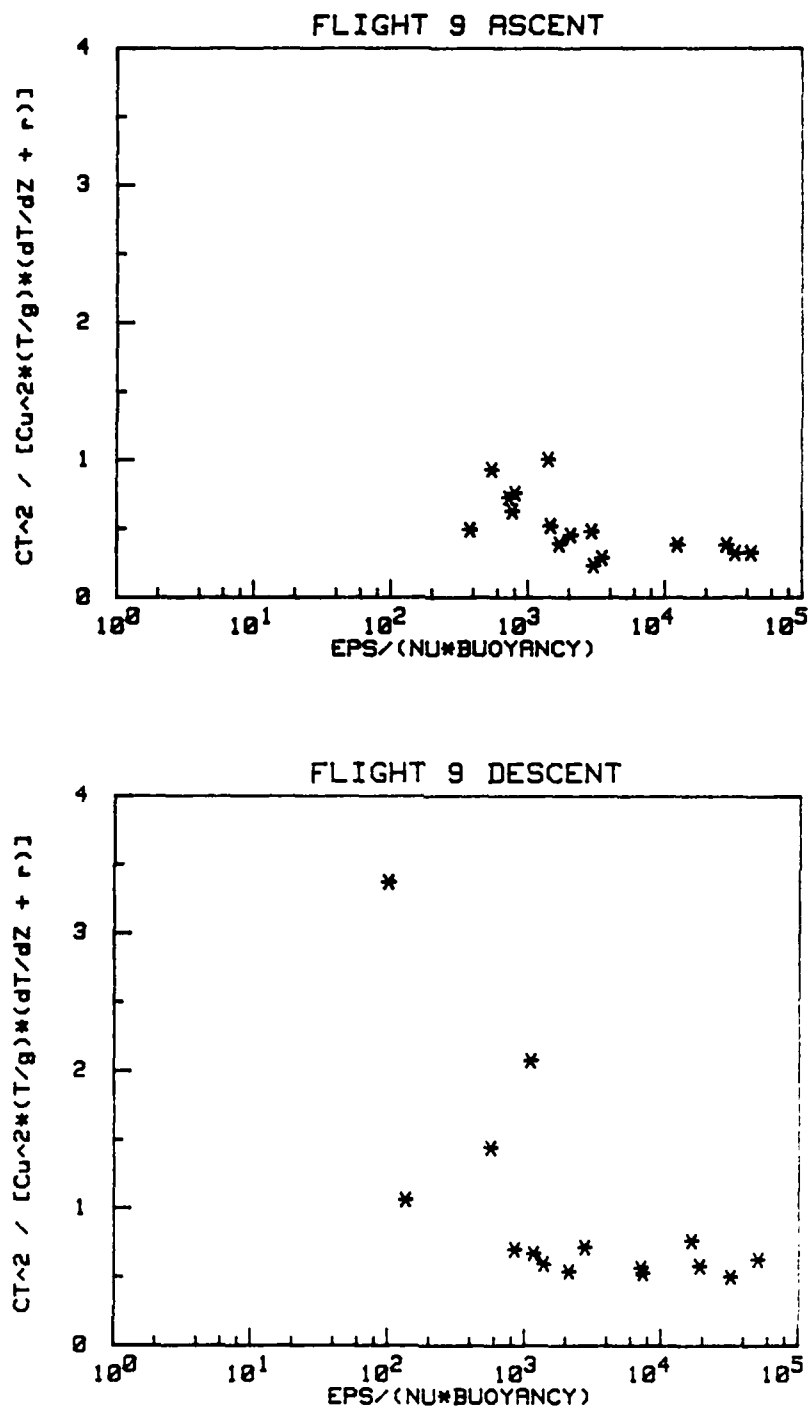


Figure 21. (continued)

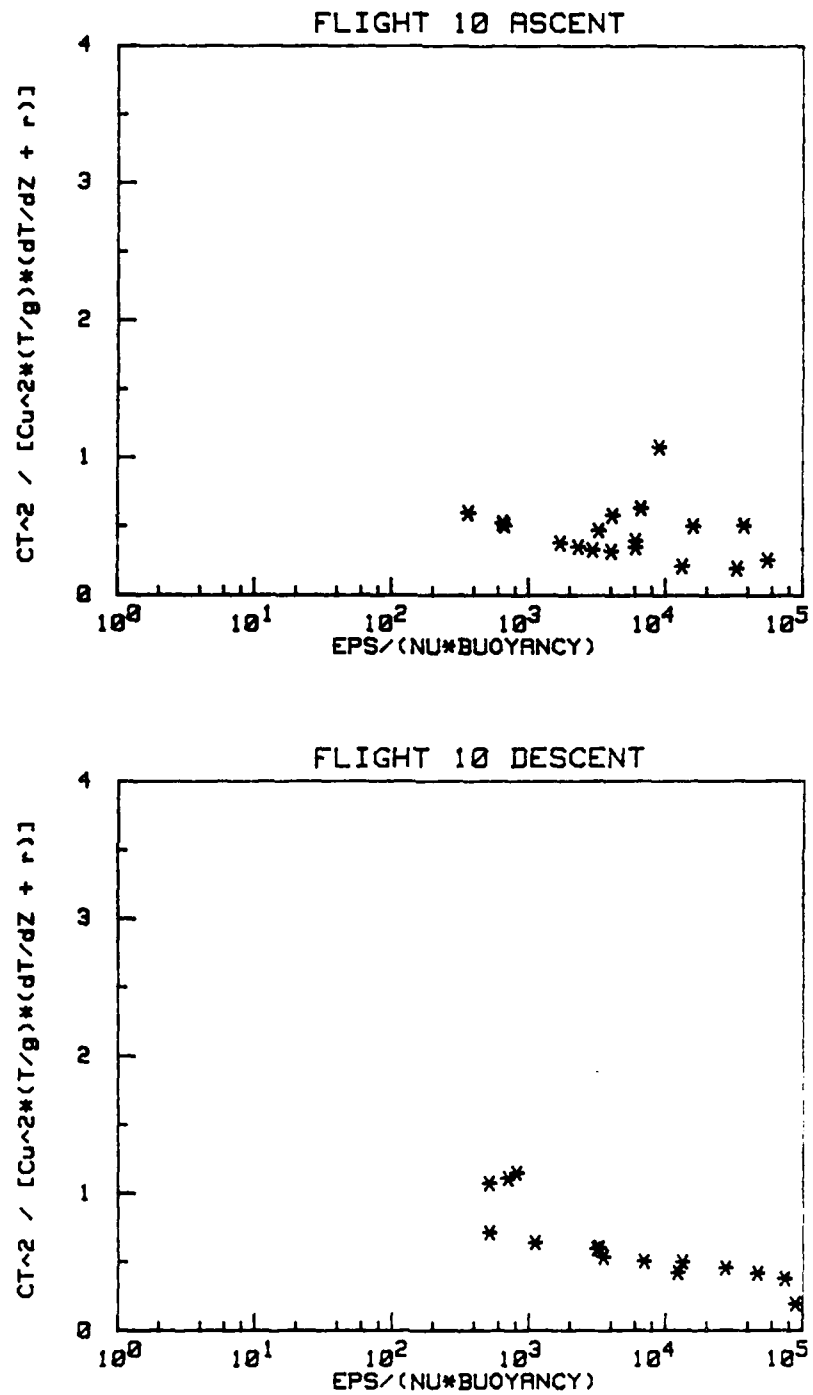


Figure 21. (continued)

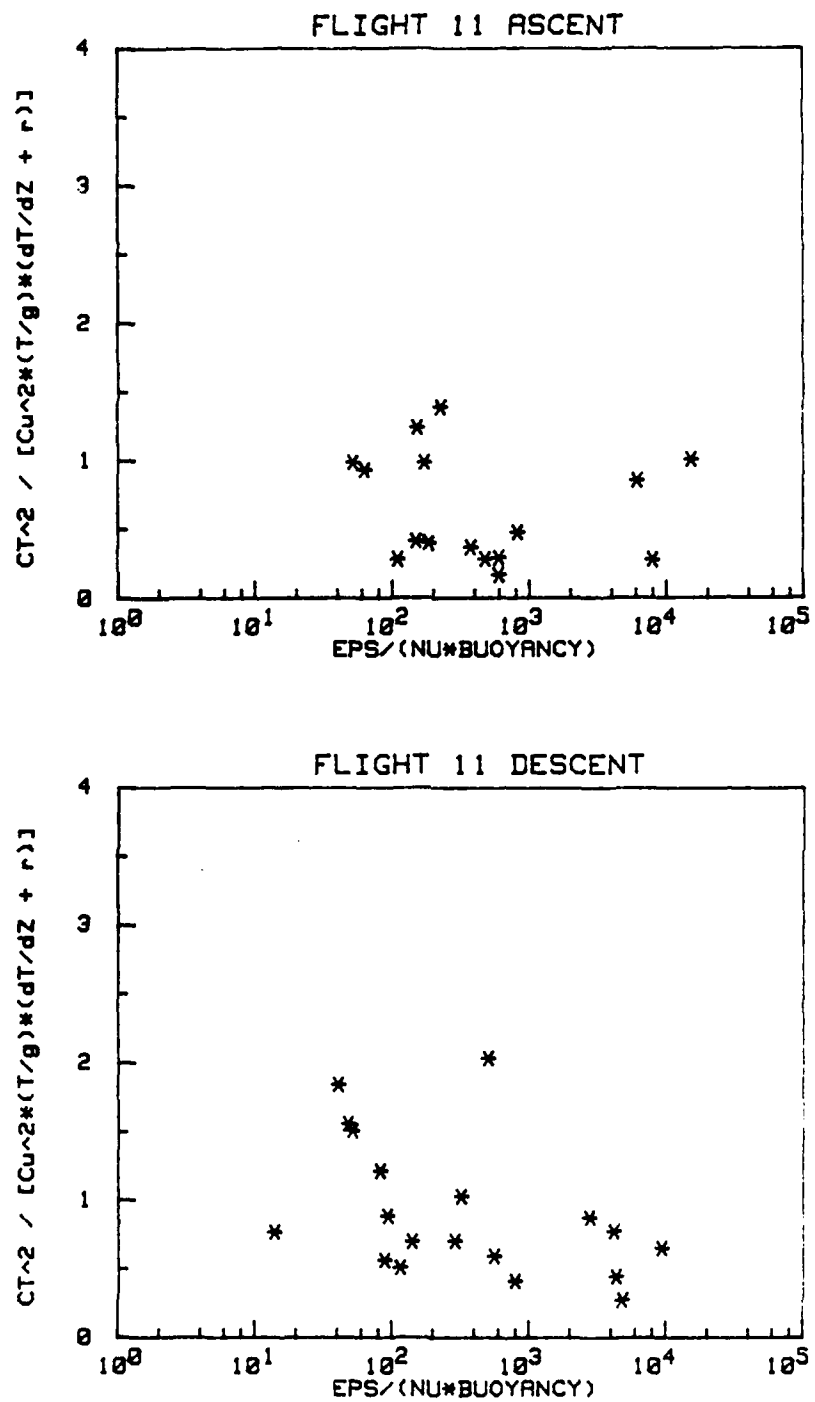


Figure 21. (continued)

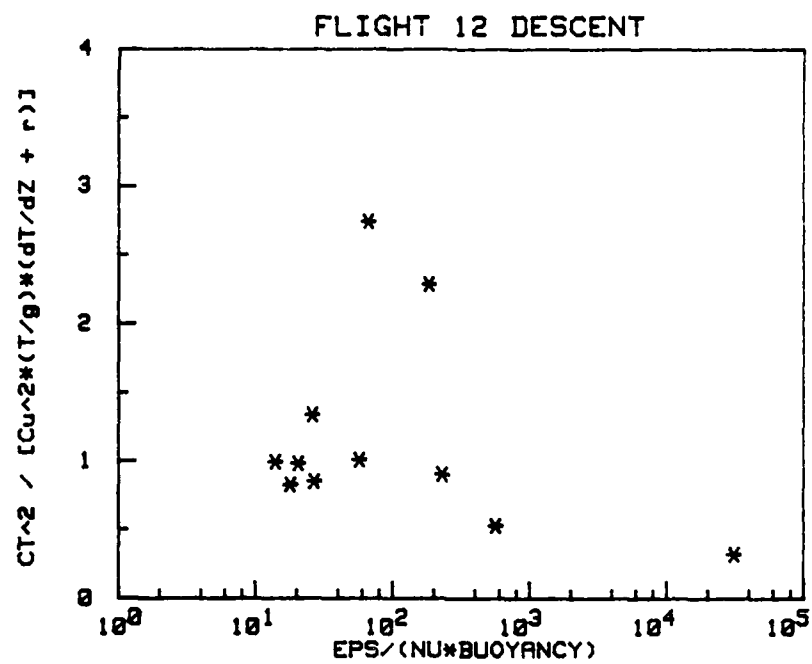


Figure 21. (continued)

were all calculated from the aircraft data. Figure 22 is a composite of all vertical flights. This plot clearly shows that as turbulence activity goes down, the ratio of C_T^2 to normalized C_u^2 goes up. For activity values above 10^2 , the $C_T^2/C_u^2(\text{norm})$ ratio becomes constant at about 0.4.

7.2 Mean Gradients and Richardson Number

Next, the Richardson number was evaluated. Since VanZandt et al. (1981) defined R_i as N/S , N versus S was plotted, thus showing Richardson number as a slope (Figure 23). N was calculated by a finite difference derivative between each level in the digitized aircraft potential temperature profiles, while S was calculated by finite difference from the profiler hourly average taken during the time the aircraft was collecting data (Table 1). S was calculated as $(\partial u/\partial z)^2 + (\partial v/\partial z)^2$. Figure 24 is a composite of all flights shown in Figure 23. Most values show $R_i > 0.25$ above the broken line, with the shear term on the order of 10^{-5} and the buoyancy term ranging from 10^{-5} to 4×10^{-4} . Richardson number profiles for each flight were directly calculated (Table 4), and then averaged (Table 5).

These values of N and S are the necessary input parameters for the VanZandt et al. model which was used to predict vertical profiles of C_n^2 and ϵ . This was done for each flight conducted at Penn State where profiler data was available (Figure 25). The model output is normalized optical C_n^2 . Standard pressure calculated from the geometric height and the aircraft temperature profile were used to

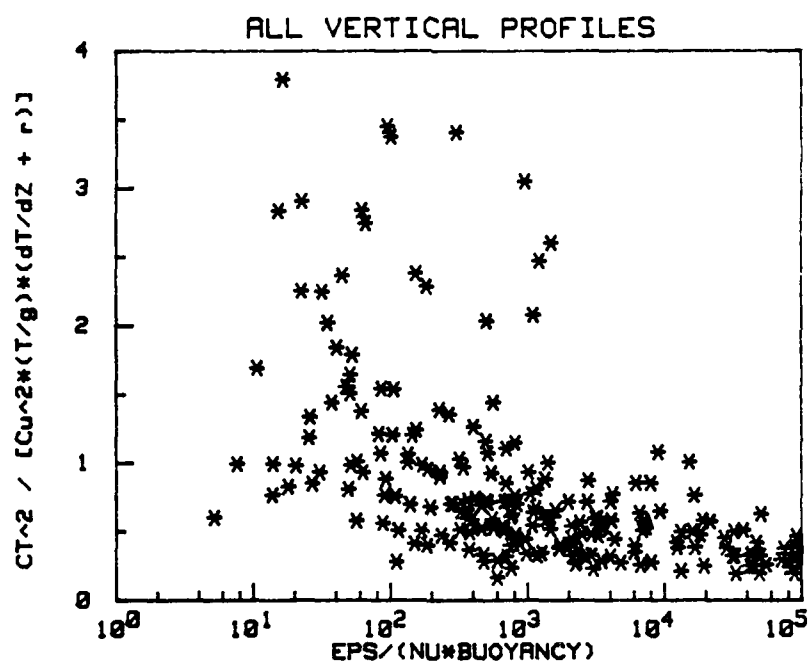


Figure 22. A composite comparison of C_T^2 divided by C_u^2 normalized as in Figure 20 versus a turbulent activity parameter $\epsilon/(\nu N)$ for all vertical profiles.

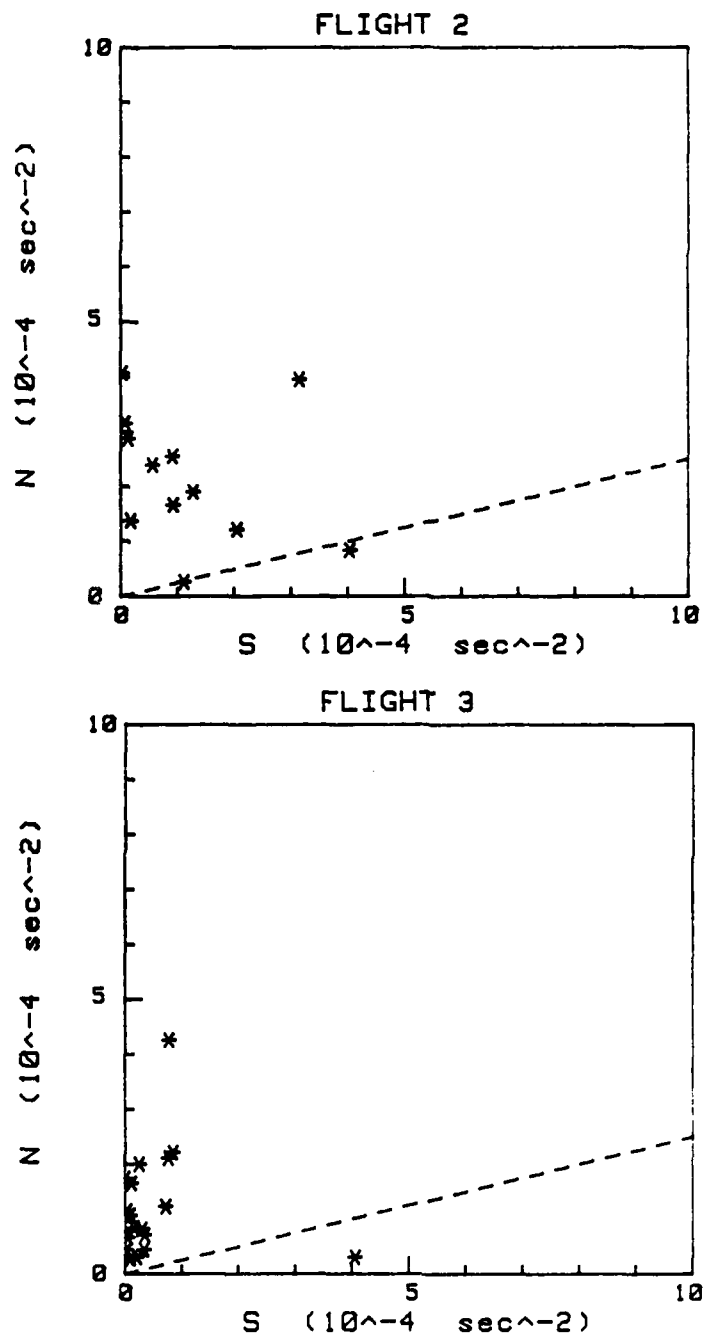


Figure 23. Comparisons of the VanZandt et al. parameters N , the Brunt-Vaisala frequency squared, and S , the shear squared. Comparison is shown for each vertical aircraft flight during which the radar operated (labeled above each graph). N was calculated using aircraft potential temperature profiles and S was calculated using radar wind profiles. Note units. Broken line represents $R_1 = 0.25$.

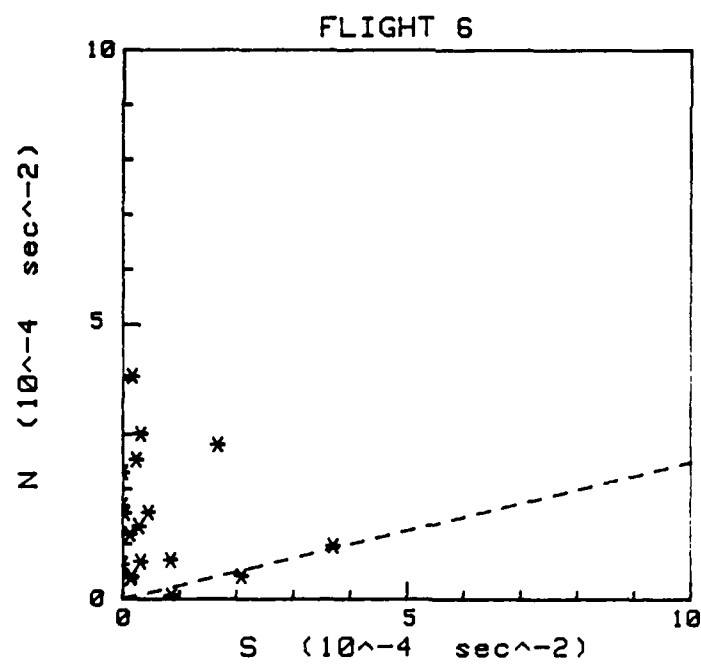
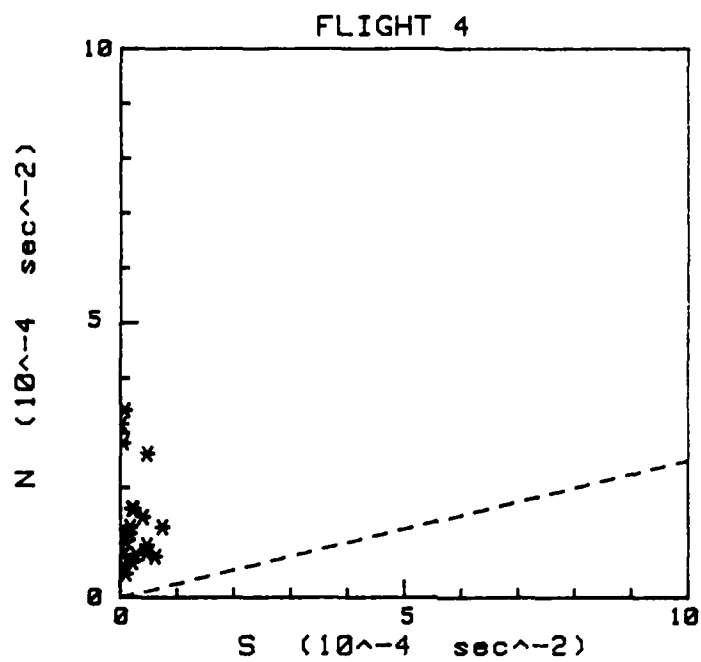


Figure 23. (continued)

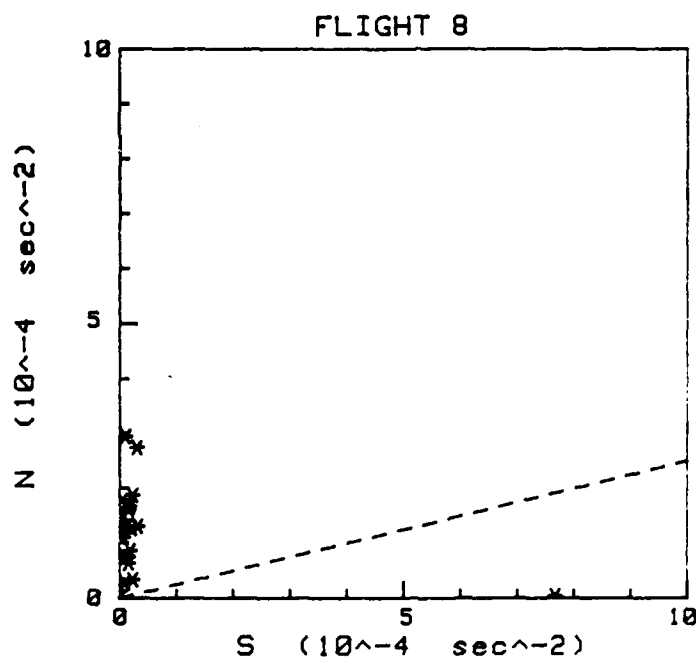
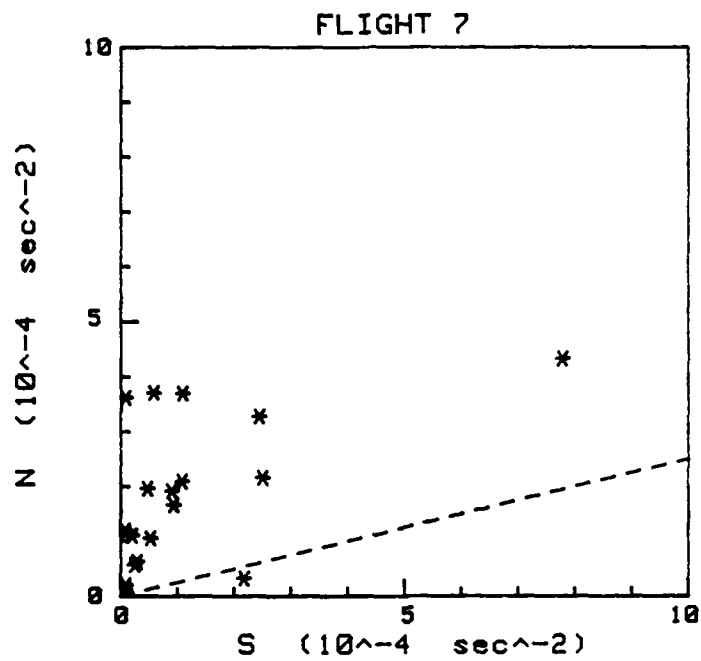


Figure 23. (continued)

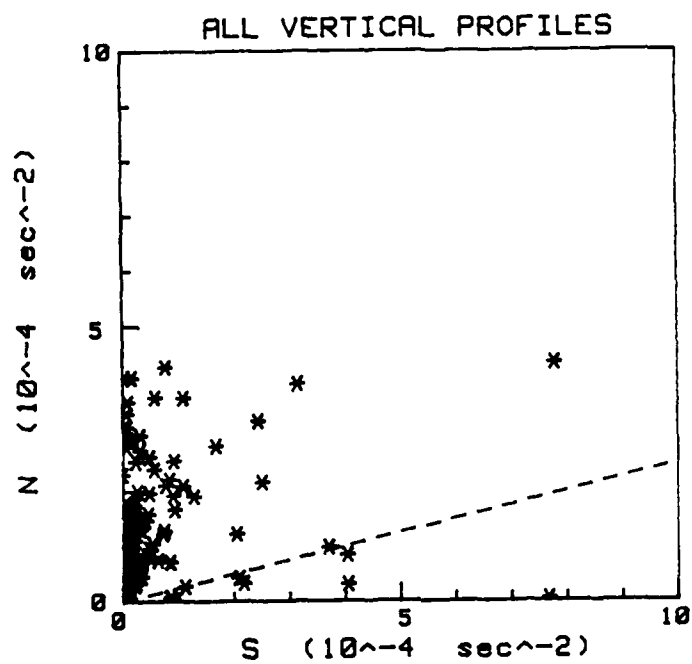


Figure 24. A composite comparison of N versus S for all flights shown in Figure 23. Note units. Broken line represents $R_1 = 0.25$.

Table 4.

Calculated vertical profiles of Richardson number based on $R_i = N/S$ and using N and S values shown in Figure 17. Altitude shown is MSL and is the average altitude between each vertical radar observation level.

Flight 2		Flight 3	
<u>Alt (km)</u>	<u>R_i</u>	<u>Alt (km)</u>	<u>R_i</u>
1.4	1.2	1.7	9.04
1.7	2.61	2	20.99
2	3.92	2.3	5.18
2.3	31.98	2.6	6.99
2.6	6.73	2.9	2.45
2.9	.19	3.2	88.53
3.2	.56	3.4	1.58
3.4	18.94	3.7	11.59
3.7	74.74	4	0
4	1.4	4.3	.07
4.3	.21	4.6	4.51
4.6	1.68	4.9	10.18
		5.2	1.15
		5.5	11.4
		5.8	1.17
		6.1	2.56
		6.4	1.83
		6.6	8.96
		6.9	2.39
		7.2	0
		7.5	2.02

Table 4.
(continued)

Flight 4		Flight 6	
<u>Alt (km)</u>	<u>R_i</u>	<u>Alt (km)</u>	<u>R_i</u>
1.4	2.45	1.4	-.03
1.7	34.24	1.7	142.19
2	86.56	2	.78
2.3	5.99	2.3	21.71
2.6	5.87	2.6	8.65
2.9	1.09	2.9	179.84
3.2	-.02	3.2	1.6
3.4	39.34	3.4	3.2
3.7	3.23	3.7	181.64
4	6.27	4	7.6
4.3	6.21	4.3	2.24
4.6	10.47	4.6	9.6
4.9	6.66	4.9	27.89
5.2	3.32	5.2	4.13
5.5	5.11	5.5	1.92
5.8	1.84	5.8	2.19
6.1	9.16	6.1	.05
6.4	31.57	6.4	-.02
6.6	138.56	6.6	-.02
6.9	2.49	6.9	.19
7.2	1.53	7.2	.25
7.5	1.6	7.5	0
7.8	-1.53		

Table 4.
(continued)

Flight 7		Flight 8	
<u>Alt</u> (km)	<u>R_i</u>	<u>Alt</u> (km)	<u>R_i</u>
1.4	-.05	1.4	.02
1.7	-.21	1.7	0
2	1.82	2	2.31
2.3	1.81	2.3	8.51
2.6	1.28	2.6	8.05
2.9	.82	2.9	8.64
3.2	3.21	3.2	8.93
3.4	1.67	3.4	23.48
3.7	32.94	3.7	17.85
4	.13	4	-1.22
4.3	.53	4.3	1.22
4.6	3.81	4.6	8.08
4.9	4.54	4.9	67.55
5.2	4.94	5.2	3.82
5.5	2.02	5.5	6.6
5.8	10.74	5.8	5.3
6.1	11.11	6.1	7.18
6.4	1.56	6.4	11.93
6.6	4.67	6.6	23.27
6.9	6.6	6.9	-8.82
7.2	1.9	7.2	3.68
7.5	1.1	7.5	7.03
7.8	1.99	7.8	3.3

Table 5.

The arithmetically averaged Richardson number at each height for all vertical flights.

Average Richardson Number

<u>Alt</u> (km)	<u>R_i</u>
1.4	0.72
1.7	31
2	19
2.3	12
2.6	6
2.9	32
3.2	17
3.4	15
3.7	54
4	2.36
4.3	1.75
4.6	6
4.9	23
5.2	3.67
5.5	5
5.8	4.25
6.1	6
6.4	9
6.6	35
6.9	0.57
7.2	1.47
7.5	2.35
7.8	1.25

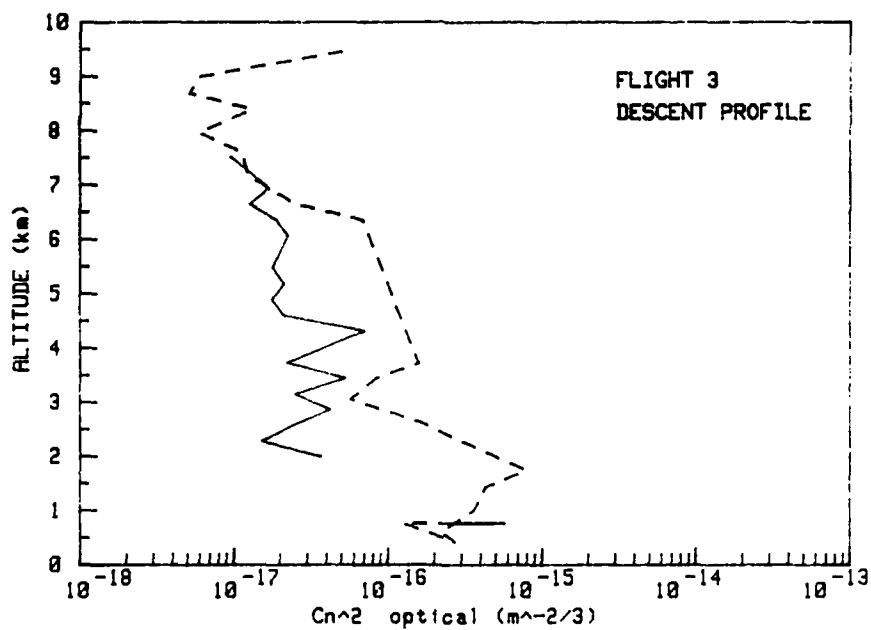
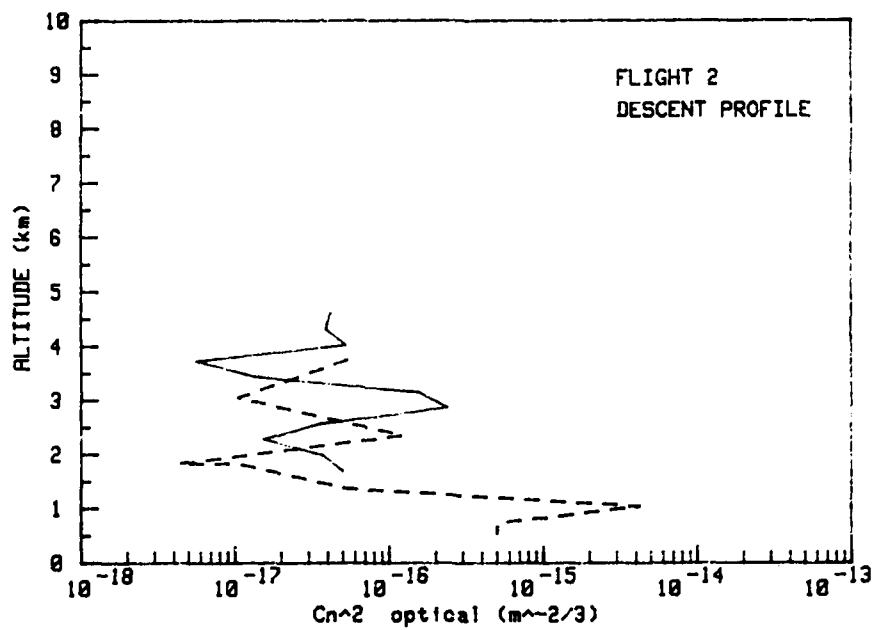


Figure 25. Comparison of the VanZandt et al. model vertical profile prediction of C_n^2 -optical (solid line) and the aircraft C_T^2 -derived vertical profile of C_n^2 -optical (broken line). PSU flights are shown (labeled interior to each graph).

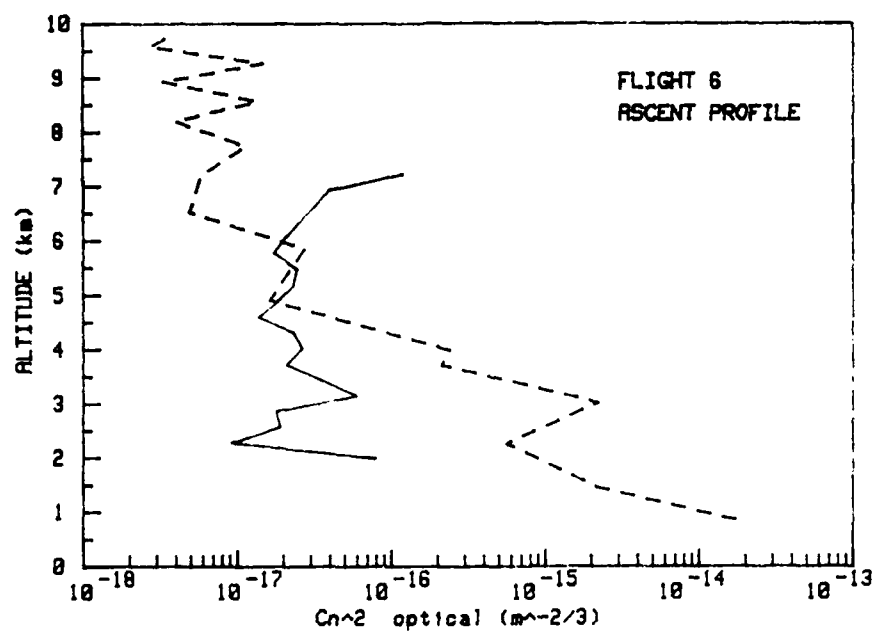
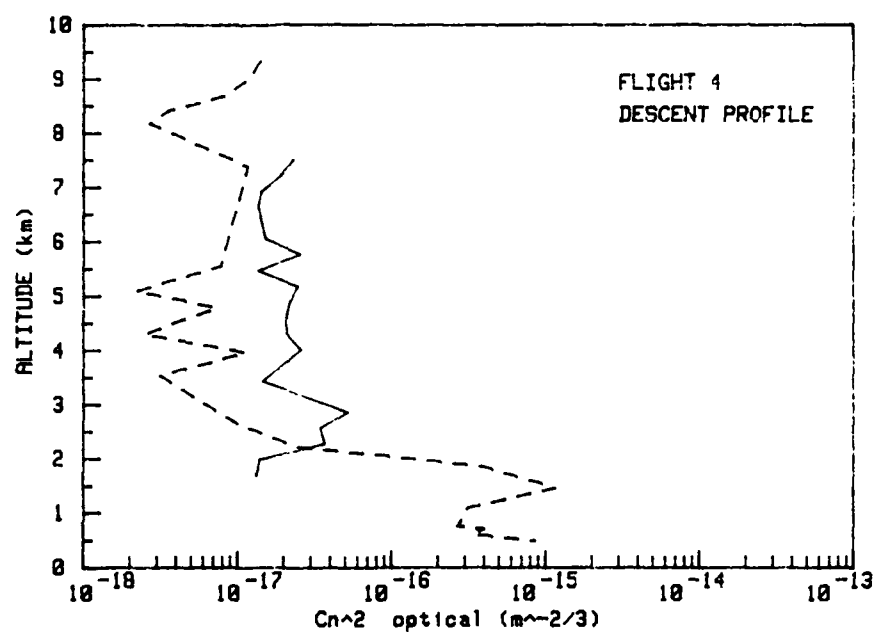


Figure 25. (continued)

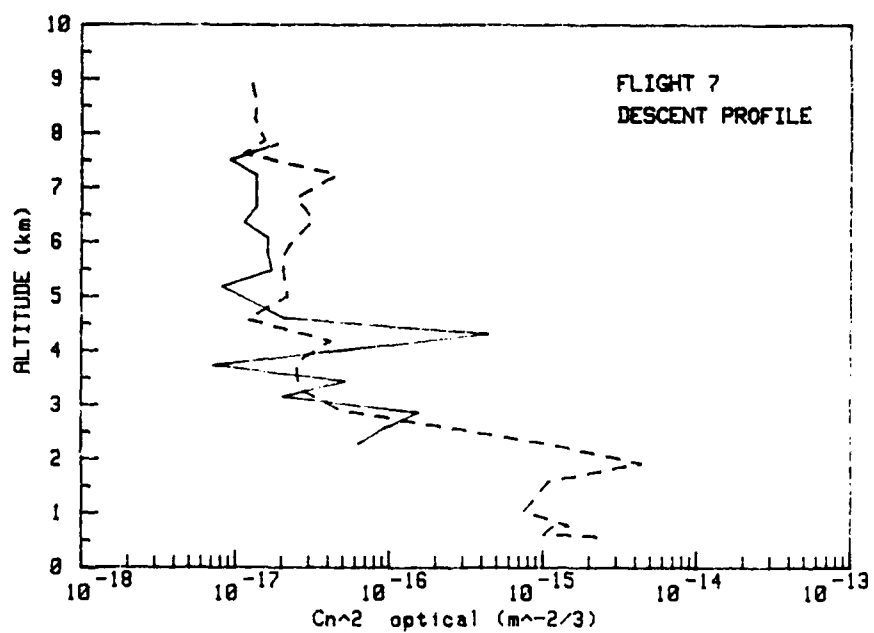
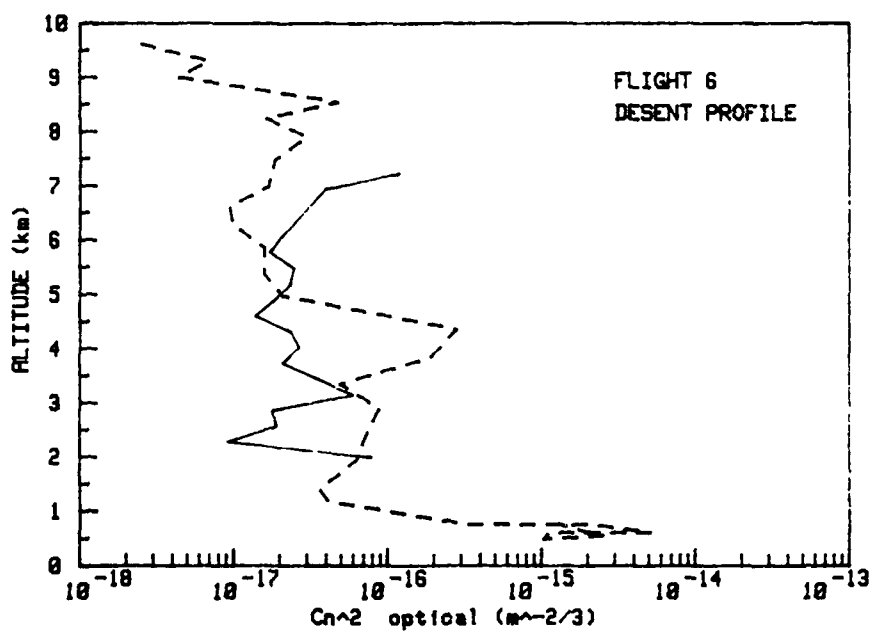


Figure 25. (continued)

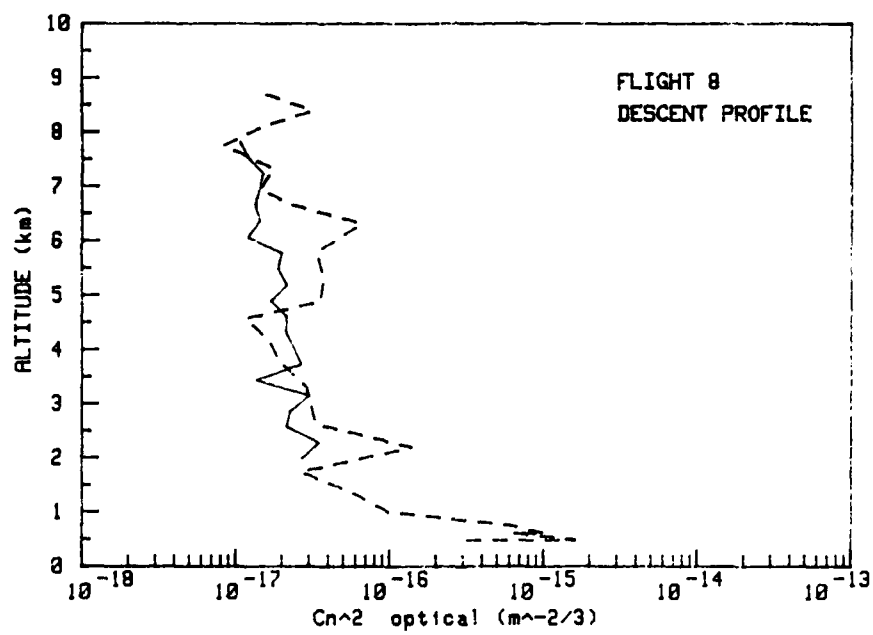
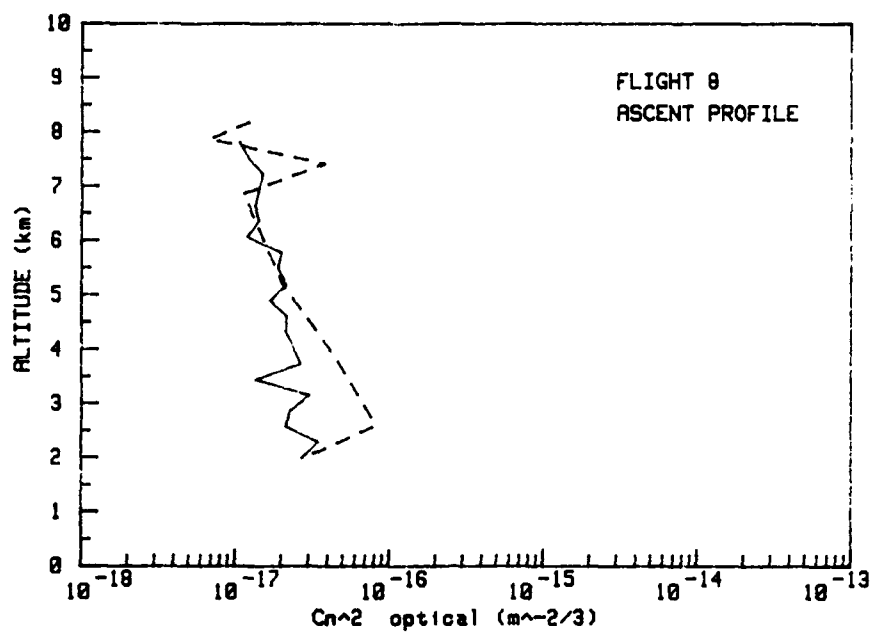


Figure 25. (continued)

"de-normalize" the model-derived parameter. Since only the high resolution profiler range gates were used to calculate S at a resolution of 290 m, the prediction was only calculated from 1410 m MSL to 7515 m MSL. An average MSL altitude for State College, PA, is 300 m. Except for flight 6(ascent) the model and aircraft profiles agreed to within an order of magnitude. This particular discrepancy in flight 6 is thought to be the result of errors in gain records for the flight.

7.3 Profiles of C_n^2

The VanZandt et al. model can also be used to give radar C_n^2 . The relationship between profiler measured C_n^2 -radar and C_n^2 -optical is a function of temperature and humidity (Tatarskii 1971). This parameter, previously referred to as X^2 , has been calculated using the aircraft specific humidity and temperature data. X^2 is the ratio of C_n^2 -radar to C_n^2 -optical. X^2 at each aircraft average observation level was calculated with a polynomial fit to the temperature profile and a finite difference derivative from the humidity profile. Smoothing of the vertical profiles was achieved by setting negative or zero temperature derivatives equal to 0.00001 K/m and positive specific humidity profiles equal to zero. This calculation is given in Table 6. X^2 at each average profiler high resolution gate height was also calculated with finite difference derivatives from both temperature and humidity digitized profiles. Smoothing was performed as before. This calculation is given in Table 7. An arithmetically averaged X^2 profile from Table 7 is given in Table 8. High humidity in the boundary layer gives extremely high

Table 6.
 X^2 vertical profiles for each flight during which the profiler operated, calculated at each aircraft observation level in MSL altitude with aircraft-measured temperature and specific humidity profiles.

Flight 2	Descent	Flight 3	Descent
Alt (km)	X^2	Alt (km)	X^2
4.4	1	9	1
3.8	1	8.7	1
3	1	8.4	1.6
2.3	1.2	8	1.3
1.8	1.1	7.6	1.3
1.4	42.8	7.2	1.2
1	25.5	6.6	1.4
.7	12.5	6.3	1.6
.5	148.6	5.8	1.9
		5.4	1
		5	1
		4.6	1.5
		4.1	1.8
		3.7	2.3
		3.4	1.7
		3	1.9
		2.6	1.5
		1.7	12.4
		1.4	2.6
		1	2.3
		.6	1914
		.4	13019
		.8	3717
		.3	12907

Table 6.
(continued)

Flight 4 <u>Alt</u> (km)	Descent <u>X²</u>	Flight 6 <u>Alt</u> (km)	Descent <u>X²</u>
9	76189	9	1
8.7	106301	8.5	1.3
8.4	104241	8.2	1.2
8.2	232623	7.9	6.4
7.4	1	7.5	1.1
6.8	1	7	1.8
6.1	1	6.6	18.9
5.6	1	6.3	4.6
5.1	4.6	5.9	1
4.8	1	5.4	1
4.3	3.8	5	1.9
4	1.1	4.4	12.8
3.5	1	3.8	2.4
3	1.8	3.4	1
2.7	1.6	2.9	13.4
2.2	1.8	2.4	3.2
1.9	3.4	2	13.9
1.5	227.8	1.4	7.7
.8	1.4	1.2	7.7
.7	2.33E+6	.8	1.3
.6	2.32E+6	.7	4.2
.5	2.3E+6	.6	3.7
		.5	3.2

Table 6.
(continued)

Flight 7 <u>Alt</u> (<u>km</u>)	Descent <u>X</u> ²	Flight 8 <u>Alt</u> (<u>km</u>)	Descent <u>X</u> ²
8.5	1	8.4	1.9
8.3	1	8.1	3.5
7.9	2.6	7.7	3.3
7.6	3.5	7.3	10.8
7.2	13.4	7	11.6
6.8	4.1	6.7	3.8
6.4	39.2	6.3	21.7
5.9	3.3	5.8	15.3
5.7	17.8	5.3	6.1
5	24.6	4.9	1.2
4.6	5.8	4.6	54.8
4.2	4	4.1	1.2
3.8	1.3	3.8	1.1
3.3	1	3.3	87.5
2.9	1	2.8	6.6
2.3	21.4	2.6	6.8
1.9	81.9	2.2	101.9
1.6	1.9	1.7	5.8
1	351269	1.4	2.2
.8	34447	1	1.6
.6	16	.8	1.6
.5	3.2	.6	1.5
		.5	1.5

Table 7.

χ^2 vertical profiles for each flight during which the profiler operated, calculated at each profiler observation level in MSL altitude with aircraft-measured temperature and specific humidity profiles.

Flight 2		Flight 3	
<u>Alt</u> (km)	<u>χ^2</u>	<u>Alt</u> (km)	<u>χ^2</u>
1.3	46.9	1.3	5.7
1.6	3.5	1.6	2.5
1.9	1.1	1.9	11.9
2.1	1.3	2.1	138.2
2.4	1.2	2.4	3.2
2.7	1.1	2.7	1.5
3	1	3	1.9
3.3	1	3.3	1.6
3.6	1	3.6	2.2
3.9	1	3.9	2.2
4.2	1	4.2	1.8
4.5	1	4.5	1.5
		4.8	1.2
		5	1
		5.3	1
		5.6	25.5
		5.9	1.9
		6.2	1.6
		6.5	1.4
		6.8	1.4
		7.1	1.2
		7.4	1.2
		7.7	1.3
		8	1.3

Table 7.
(continued)

Flight 4 Alt (km)	χ^2	Flight 6 Alt (km)	χ^2
1.3	34.9	1.3	7.8
1.6	210.3	1.6	2.9
1.9	3.4	1.9	14.9
2.1	1.8	2.1	56.2
2.4	1.9	2.4	3.2
2.7	1.6	2.7	1
3	1.8	3	13.2
3.3	1.3	3.3	1
3.6	1	3.6	1.2
3.9	1.1	3.9	2.5
4.2	3.8	4.2	1.1
4.5	6.9	4.5	13.9
4.8	1	4.8	4.2
5	4.6	5	2
5.3	2.8	5.3	1
5.6	1	5.6	5.9
5.9	1	5.9	1
6.2	1	6.2	4.2
6.5	1.9	6.5	20.4
6.8	1	6.8	6.1
7.1	1	7.1	1.7
7.4	1	7.4	1.1
7.7	1.5	7.7	2.4
8	1.1	8	6.2

Table 7.
(continued)

Flight 7		Flight 8	
<u>Alt</u> (km)	\bar{x}^2	<u>Alt</u> (km)	\bar{x}^2
1.3	1.2	1.3	2.3
1.6	1.9	1.6	1.6
1.9	12.9	1.9	5.4
2.1	27.4	2.1	107.4
2.4	6.5	2.4	7.7
2.7	1	2.7	6.7
3	1	3	112.1
3.3	1	3.3	87.6
3.6	1.2	3.6	9.6
3.9	1.3	3.9	1.1
4.2	4	4.2	1.2
4.5	5.5	4.5	50.9
4.8	1.2	4.8	1.2
5	25.6	5	1.2
5.3	1.5	5.3	6.1
5.6	16.3	5.6	25.8
5.9	3.3	5.9	15.3
6.2	4.7	6.2	22.4
6.5	41.3	6.5	10.3
6.8	4.1	6.8	3.7
7.1	14.8	7.1	11.1
7.4	6.5	7.4	10.8
7.7	3.5	7.7	3.2
8	2.6	8	3.1

Table 8.
Arithmetically averaged X^2 vertical profiles from the Table 7
profiles.

Average Radar X^2 <u>Alt</u> (km)	Profile <u>X^2</u>
1.3	16.5
1.6	37.1
1.9	23.3
2.1	55.4
2.4	3.9
2.7	2.1
3	21.8
3.3	15.6
3.6	2.7
3.9	1.5
4.2	2.2
4.5	13.3
4.8	1.8
5	6.9
5.3	2.5
5.6	14.9
5.9	4.5
6.2	6.8
6.5	15
6.8	3.3
7.1	6
7.4	4.1
7.7	2.4
8	2.9

values of C_n^2 -radar at these levels. Aircraft profiles of C_n^2 -optical adjusted with X^2 to give C_n^2 -radar show agreement with the profiler derived C_n^2 -radar profiles (Figure 26).

For the two night flights during which multiple instruments took data, comparisons of C_n^2 -optical vertical profiles are shown. The level at which C_n^2 was measured by the AFGL scintillometer varied because the instrument was measuring at different zenith angles. To aid in graphical interpretation, for each night, all the AFGL scintillometer profile C_n^2 values were log averaged and the heights arithmetically averaged, at each level. RADC data (Figure 14) was available for one night only and was omitted for clarity. Figure 27 shows a comparison of C_n^2 -optical from the averaged AFGL scintillometer profiles, the aircraft, the VanZandt et al. model predictions, the AFGL thermosonde, and the profiler (unadjusted raw C_n^2 -radar). The ascent profile for the aircraft on flight 6 is thought to have been an incorrect gain setting which leads to the unrealistically high values in the lower part of the profile. Figure 28 is the same comparison except that the radar profile has been converted to C_n^2 -optical using the calculated X^2 profiles of Table 7. These plots show again the agreement between the model and the aircraft, while the thermosonde has good agreement with the scintillometer. The profiler C_n^2 -optical values (from the hourly average observation during the aircraft flight) show some agreement with the thermosonde.

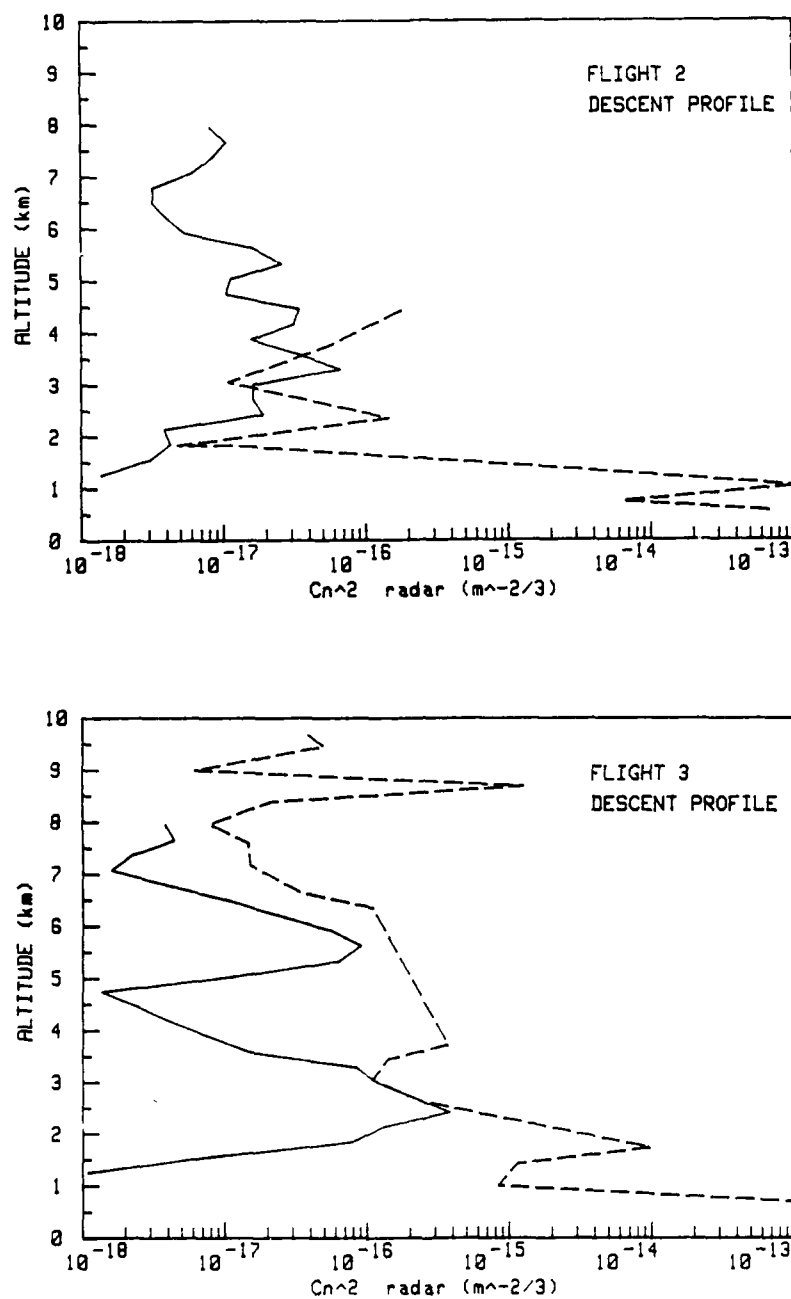


Figure 26. Comparison of C_n^2 -radar as derived from profiler (solid line) and from aircraft C_n^2 -optical, multiplied by the conversion factor X^2 to give C_n^2 -radar (broken line). PSU flights are shown (labeled interior to each graph).

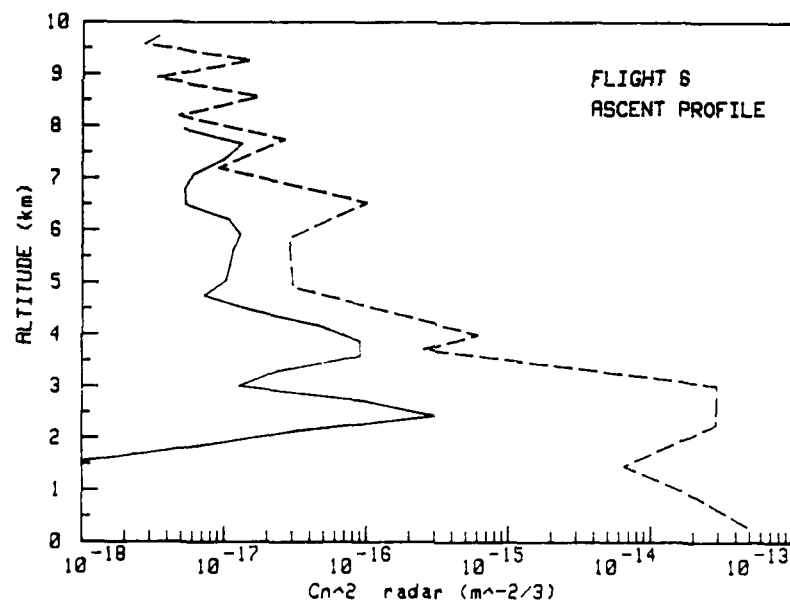
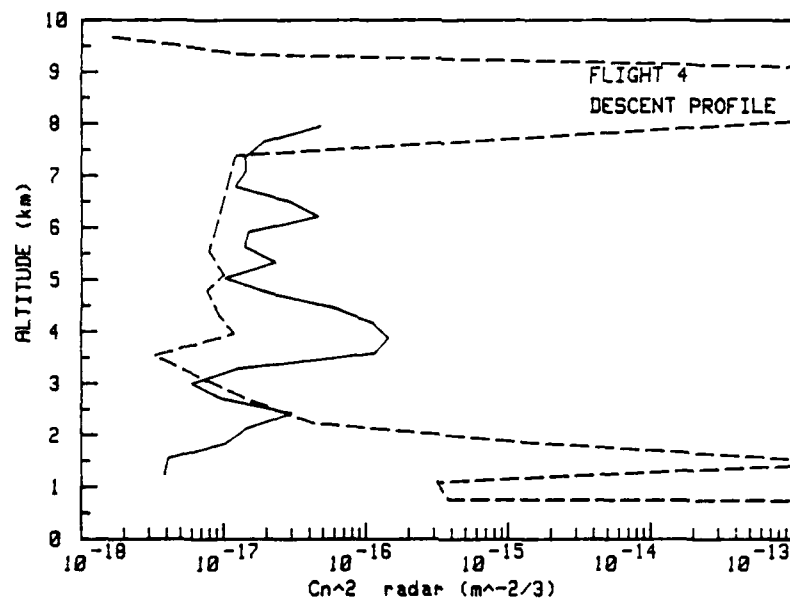


Figure 26. (continued)

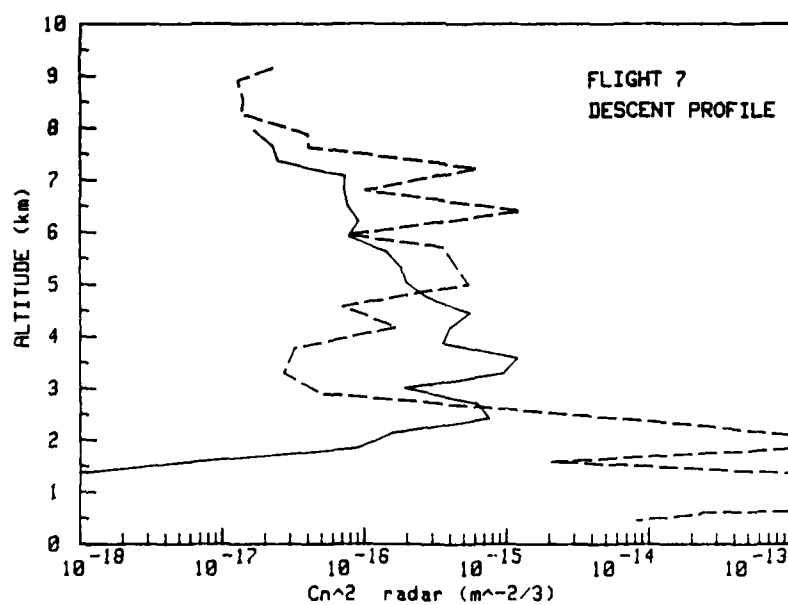
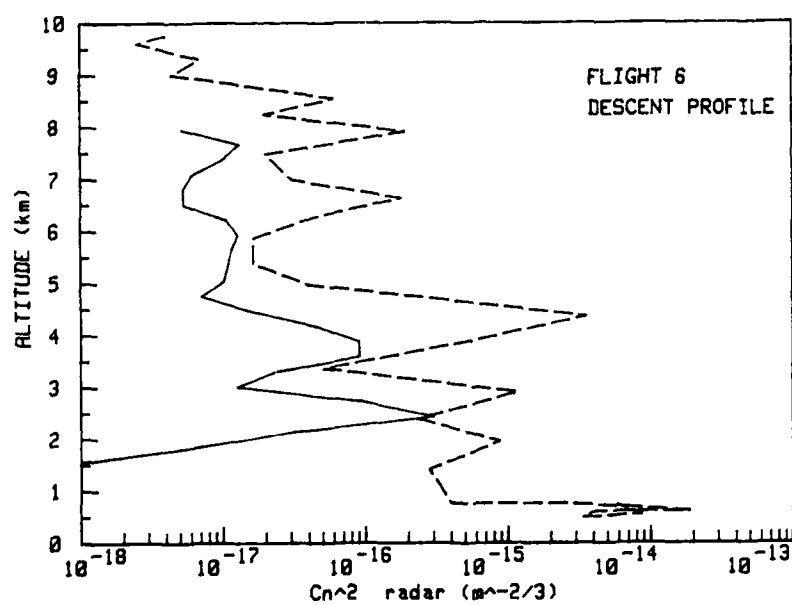


Figure 26. (continued)

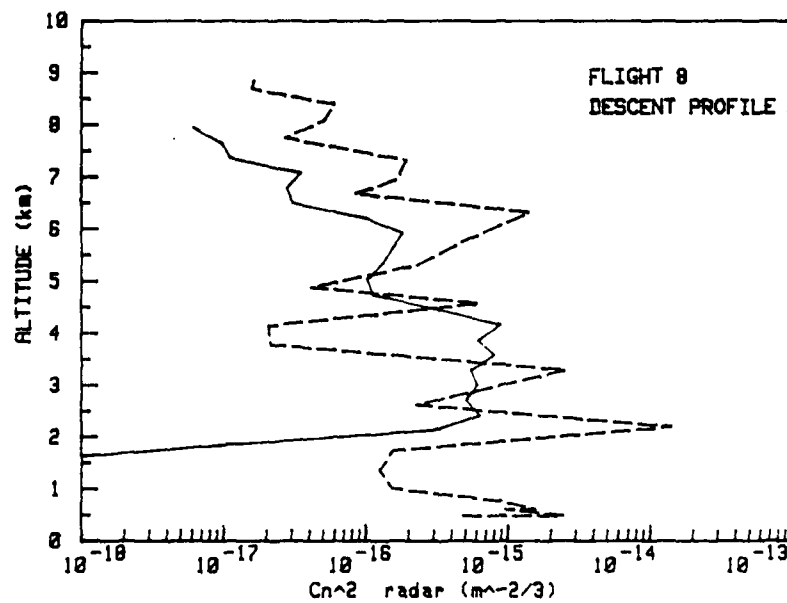
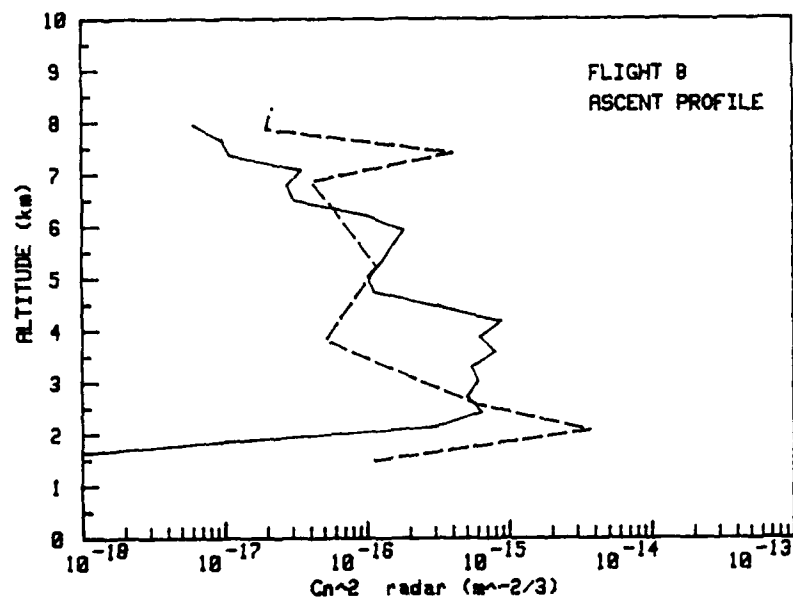


Figure 26. (continued)

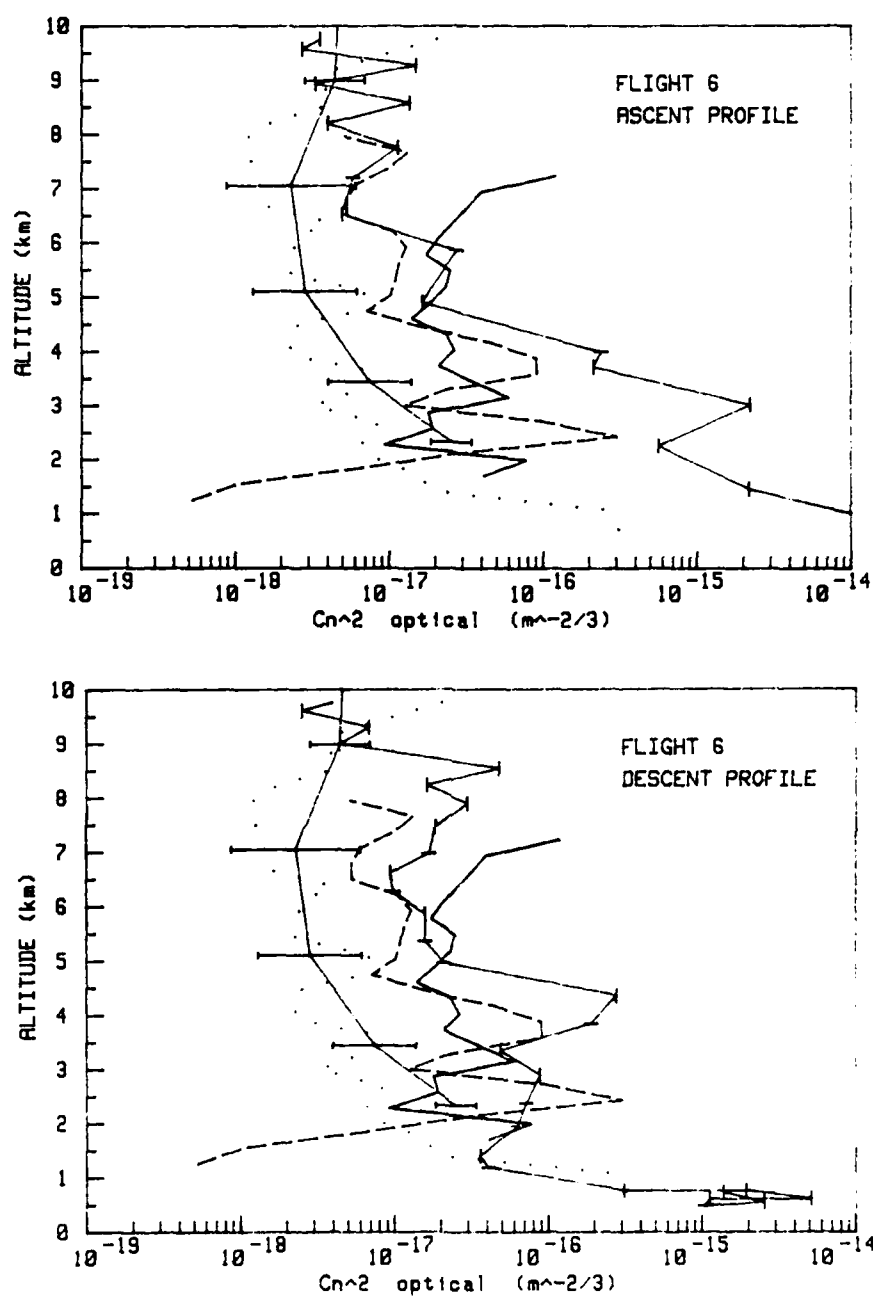


Figure 27. Comparison of vertical profiles of C_n^2 -optical. Altitude is MSL. Bars represent standard deviation of AFGL scintillometer data. Profiler values are raw C_n^2 -radar (not converted to C_n^2 -optical). Aircraft flight designations are labeled interior to each graph.

Log averaged scintillometer	— —	Aircraft	—+—
VanZandt et al. model	———	Profiler	- - - -
Arithmetically smoothed thermosonde		

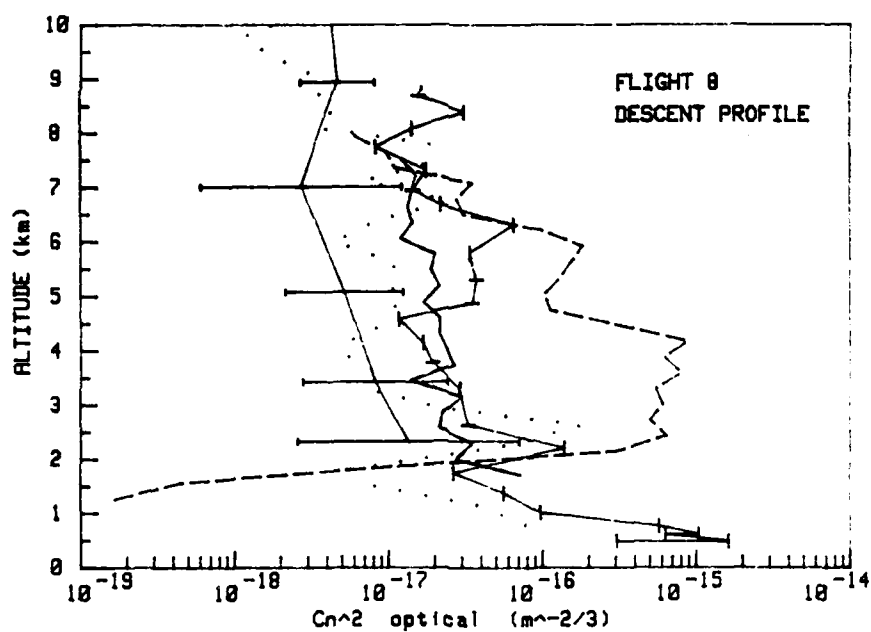
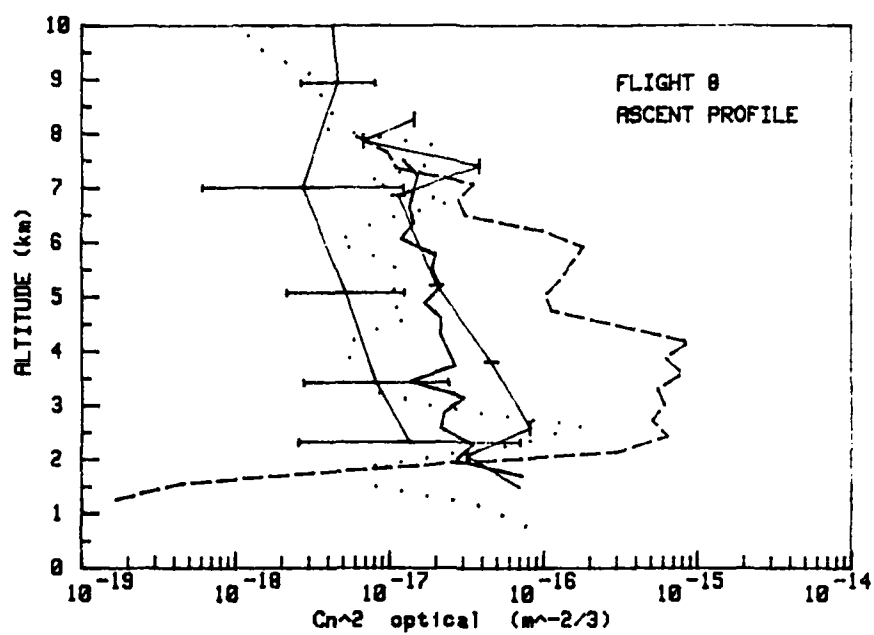


Figure 27. (continued)

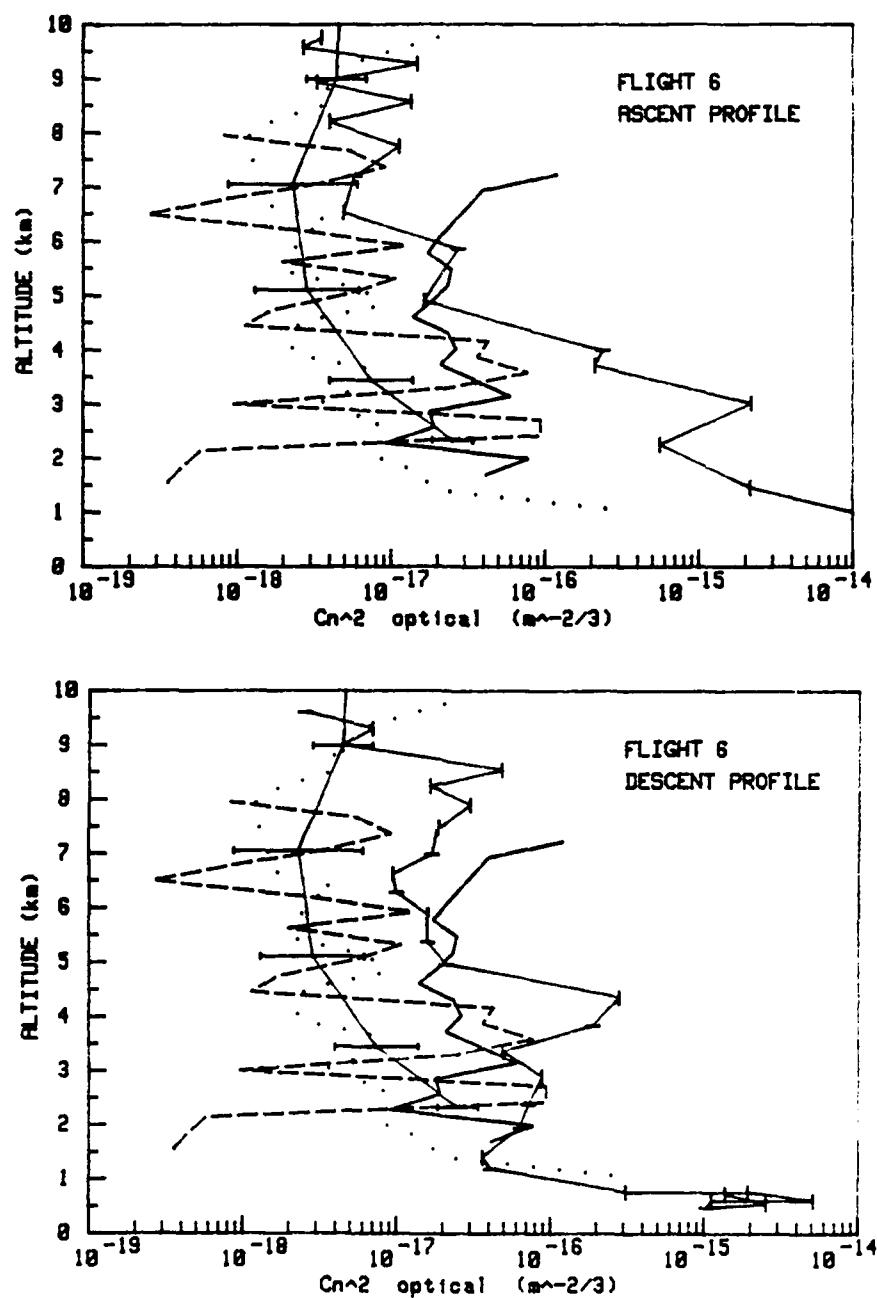


Figure 28. Comparison of vertical profiles of C_n^2 -optical. Altitude is MSL. Bars represent standard deviation of AFGL scintillometer data. Profiler values have been converted to C_n^2 -optical. Aircraft flight designations are labeled interior to each graph.

Log averaged scintillometer	— —	Aircraft	—+—
VanZandt et al. model	—	Profiler	- - -
Arithmetically smoothed thermosonde		

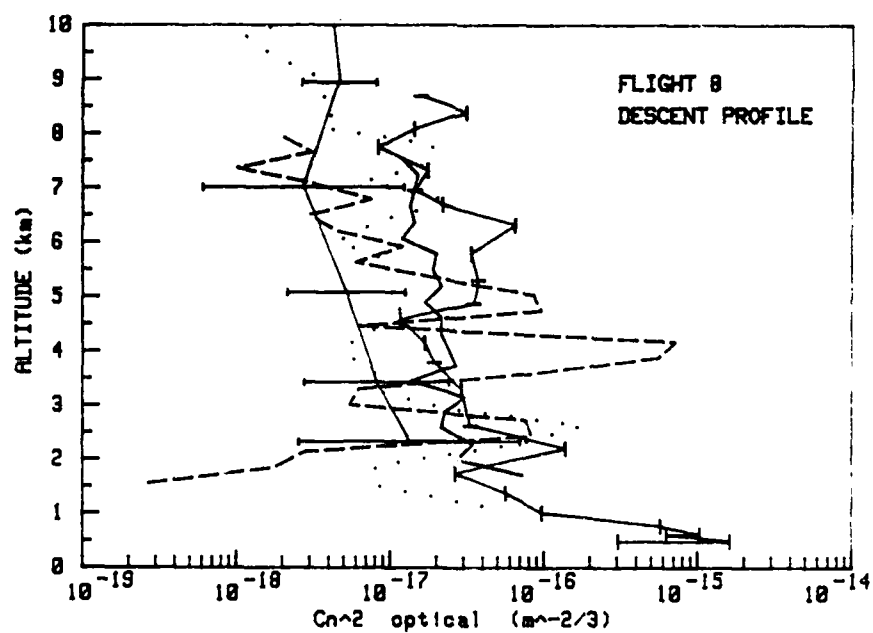
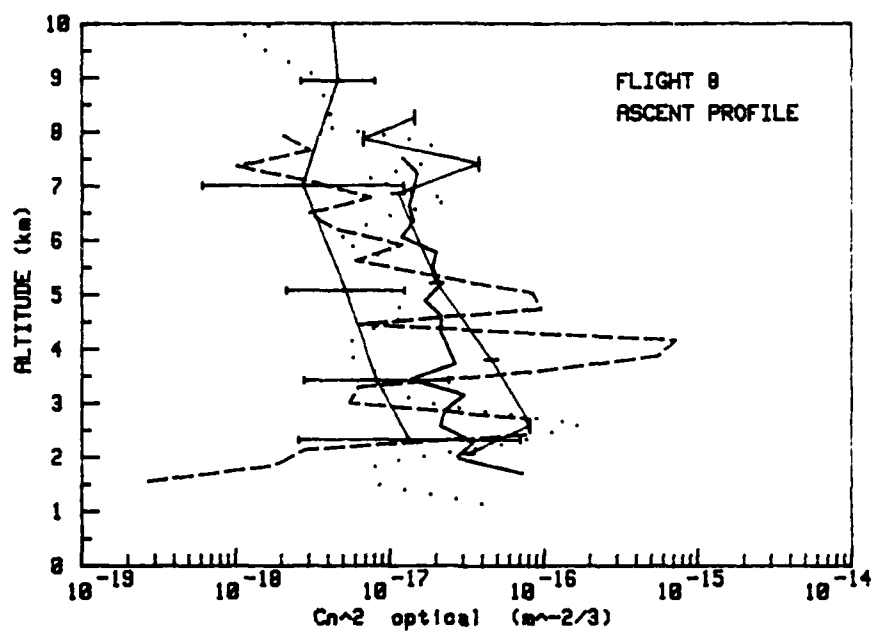


Figure 28. (continued)

7.4 Propagation Parameters

Other optical parameters of interest are the coherence length r_o and isoplanatic angle θ_o . These are related to vertical integrals of C_n^2 (Murphy and Battles 1986)

$$r_o = k_r \left[\int_0^\infty C_n^2(z) dz \right]^{-3/5} \quad (7.3)$$

$$\theta_o = k_t \left[\int_0^\infty C_n^2(z) z^{5/3} dz \right]^{-3/5} \quad (7.4)$$

where k_t and k_r are functions of wavelength ($\lambda^{1.2}$ dependence).

Assuming a wavelength, and a linear relation between observations of C_n^2 -optical at each level, the integrals can be evaluated numerically. But contributions from above and below the measured profile must be calculated based on theoretical assumptions. In the boundary layer, Murphy and Battles (1986) assumed C_n^2 to go as

$$C_n^2(z) = C_n^2(z_b) (z/z_b)^{-2/3} \quad (7.5)$$

where z_b is the lowest level of the measured profile. In the upper atmosphere, C_n^2 was modeled by an exponential decrease

$$C_n^2(z) = C_n^2(z_t) e^{-a(z-z_t)} \quad (7.6)$$

where $a = (\ln 10) DR$, and DR (the atmospheric drop off rate) = 1.3×10^{-4} . With these relationships, the integral portions for θ_o above and below become (Murphy and Battles 1986)

$$\int \text{Above} = z_t^{5/3} (C_n^2(z_t)/a) \left[1 + (5/3)(az_t)^{-1} + (10/9)(a^2 z_t^2)^{-1} \right] \quad (7.7)$$

$$\int \text{Below} = \frac{1}{2} z_b^{8/3} C_n^2(z_b) \quad (7.8)$$

and for r_o

$$\int \text{Above} = C_n^2(z_t)/a \quad (7.9)$$

$$\int \text{Below} = 3 z_b C_n^2(z_b) [1 - (6/z_b)^{1/3}] \quad (7.10)$$

As part of the AFGL thermosonde flights, r_o and θ_o were calculated using equations 7.3 and 7.4 linearly integrated for just the thermosonde profile, assuming $\lambda = .3 \mu$ (Robert Beland, letter to William Syrett, September 1986; Robert Beland, telephone conversation, November 1987). These values are shown in Table 9. r_o and θ_o were also calculated by Murphy and Battles (1986) with all the above integral equations and theoretical assumptions for the atmosphere above and below, for the AFGL scintillometer data, using $\lambda = 0.5 \mu$. An average value for each night is given in Table 10. No r_o values are shown for the AFGL scintillometer because the boundary layer has a large contribution to the r_o integral. The lowest scintillometer measurement level is roughly 2 km AGL. Comparisons of contributions to the total integral showed that the theoretical extrapolations below the measured profile were contributing the major percentage to the computed value. Calculated r_o values were thus considered unreliable (Murphy and Battles 1986). To facilitate comparison, this same method and assumptions were used to compute r_o and θ_o from the aircraft data at 0.3μ and 0.5μ wavelength (Table 11). Both the aircraft and thermosonde profiles start at much lower AGL altitudes and thus the measured profile is a significant contributor to the r_o calculations for both these instruments (Robert Beland, telephone

Table 9.
AFGL-calculated optical parameters from thermosonde data.

AFGL Thermosonde Optical Data
(calculated with $\lambda = .3\mu$)

<u>Flight</u>	r_o (<u>cm</u>)	θ_o (<u>μrad</u>)
L4033	4.3	3.2
L4019	4.4	4.5

Table 10.
Average of AFGL-calculated optical parameters from scintillometer
data.

AFGL Scintillometer Data
(calculated with $\lambda = .5\mu$)

<u>Date</u>	<u>GMT Time</u>	θ_o (<u>μrad</u>)	<u>Percent Contribution</u>	
5/4/86	0342-0513	8.02	a	56.5
			b	42.2
			c	1.3
5/6/86	0317-0420	10.29	a	61.4
			b	36.8
			c	1.8

a= Scintillometer Measurement

b= Atmosphere Above

c= Atmosphere Below

Table 11.

Optical parameters from aircraft data calculated with the Murphy and Battles assumptions.

Aircraft Data
(calculated with $\lambda = .5\mu$)

<u>Date</u>	<u>Flight</u>	θ_o (μrad)	<u>Percent Contribution</u>
4 May	6	8.3	a 84.8
			b 15
			c 0.2
6 May	8	7.9	a 49.2
			b 50.7
			c 0

Aircraft Data
(calculated with $\lambda = .3\mu$)

<u>Date</u>	<u>Flight</u>	θ_o (μrad)	<u>Percent Contribution</u>
4 May	6	4.5	a 84.8
			b 15
			c 0.2
6 May	8	4.3	a 49.2
			b 50.7
			c 0

<u>Date</u>	<u>Flight</u>	r_o (cm)	<u>Percent Contribution</u>
4 May	6	2.4	a 68.5
			b 0.5
			c 31
6 May	8	4.8	a 82.2
			b 6.4
			c 11.3

a= Thermosonde Measurement
b= Atmosphere Above
c= Atmosphere Below

conversation, November 1987). The θ_0 integral, inversely, weights the upper atmosphere most heavily. Since the aircraft is limited in altitude to ≈ 10 km, the contribution to θ_0 is limited. However, due to the integral approximation, profiles in which C_n^2 drops off sharply with altitude will weight the measured layer more heavily. This is seen in the profile of flight 6. θ_0 values from the scintillometer and the aircraft (at $\lambda = 0.5 \mu$) were similar on 4 May, but disagreed on 6 May. The thermosonde and aircraft θ_0 values (at $\lambda = 0.3 \mu$) disagreed on 4 May, but agreed on 6 May.

r_0 was also measured at optical wavelengths during the EWAK experiment by the NPS r_0 scintillometer. The measured r_0 average for the aircraft flight time on the night of 4 May 1986 was 5 cm. The thermosonde and aircraft r_0 values (at $\lambda = 0.5 \mu$) differed by a factor of two on 4 May. The night of 6 May, the thermosonde and aircraft r_0 values were similar.

7.5 VanZandt et al. Model for ϵ

The VanZandt et al. model ϵ predictions are compared to ϵ profiles from the aircraft data (Figure 29). The hot wire failed during flight 4, so that only a small amount of data is available. The model shows predictions generally ranging in the area of 5×10^{-4} for all flights. There is poor agreement between the aircraft and model, the aircraft (except for flight 3) often giving values three or four orders of magnitude smaller. Aircraft values also vary much more, ranging from 10^{-3} to 10^{-7} .

A crude average profile of η , the microscale, based on the aircraft ϵ profiles is shown in Figure 30. $\eta = (\nu^3/\epsilon)^{.25}$ was

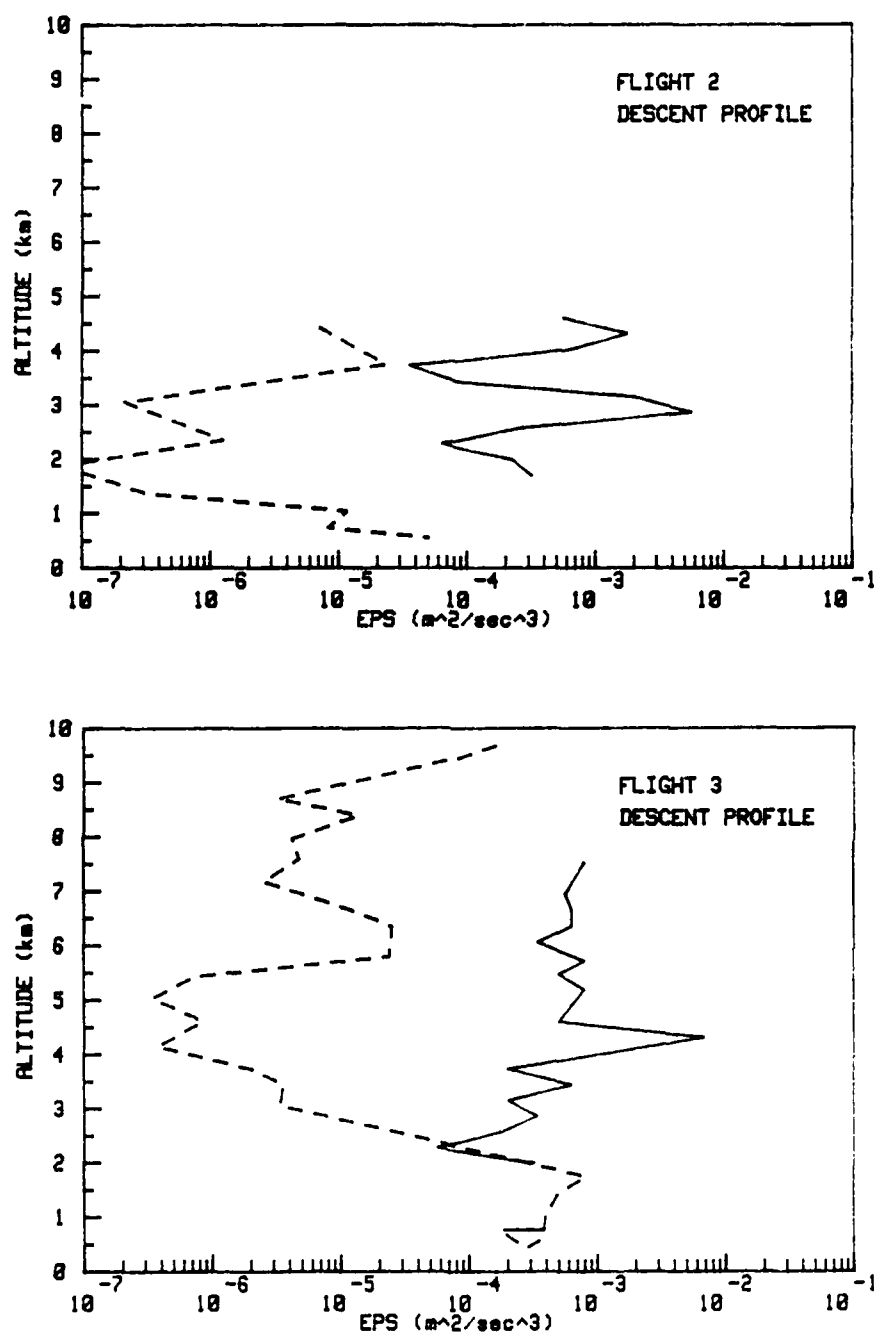


Figure 29. Comparison of vertical profiles of epsilon (ϵ), the turbulent kinetic energy dissipation rate, predicted by the VanZandt et al. model (solid line) and measured by the aircraft (broken line). Altitude is MSL. Aircraft flight designations are given interior to each graph.

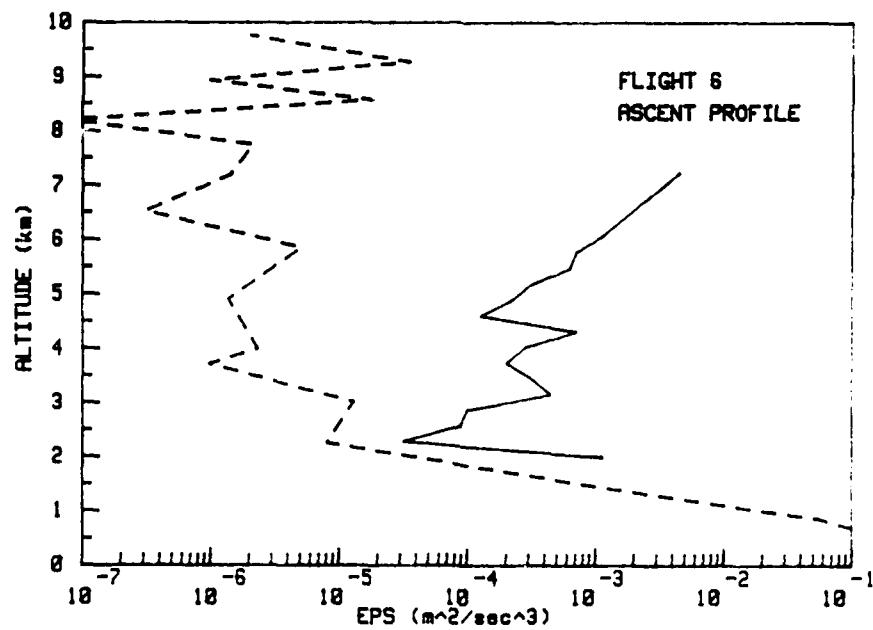
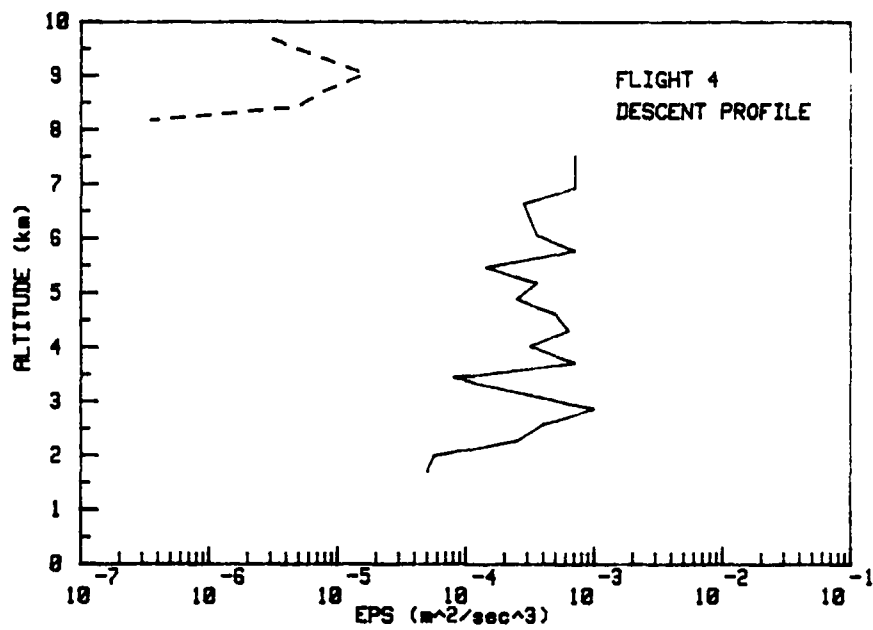


Figure 29. (continued)

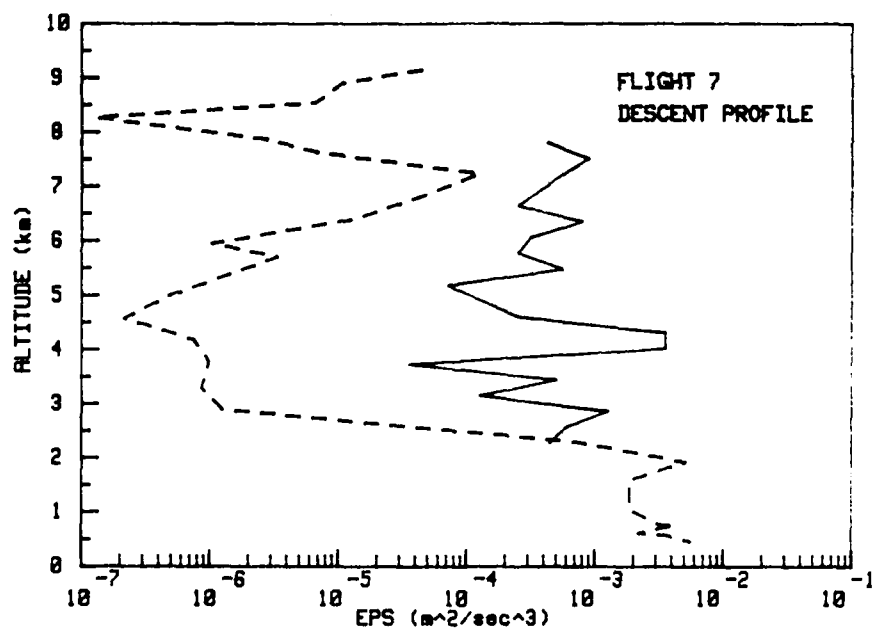
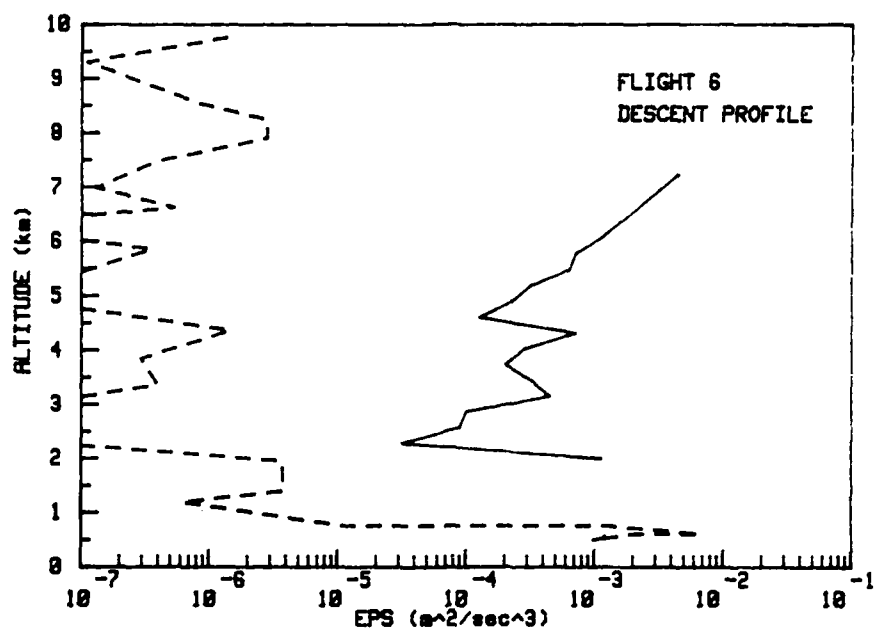


Figure 29. (continued)

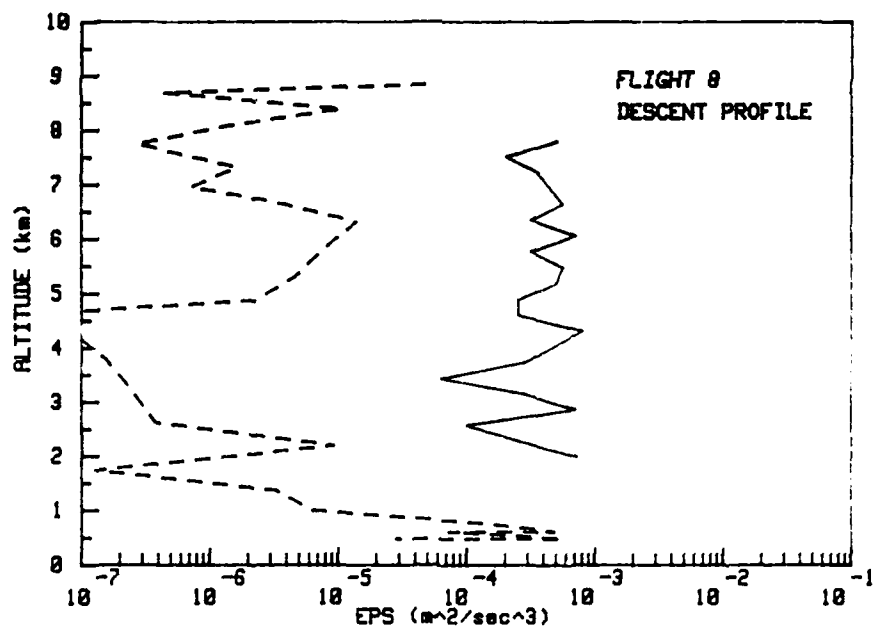
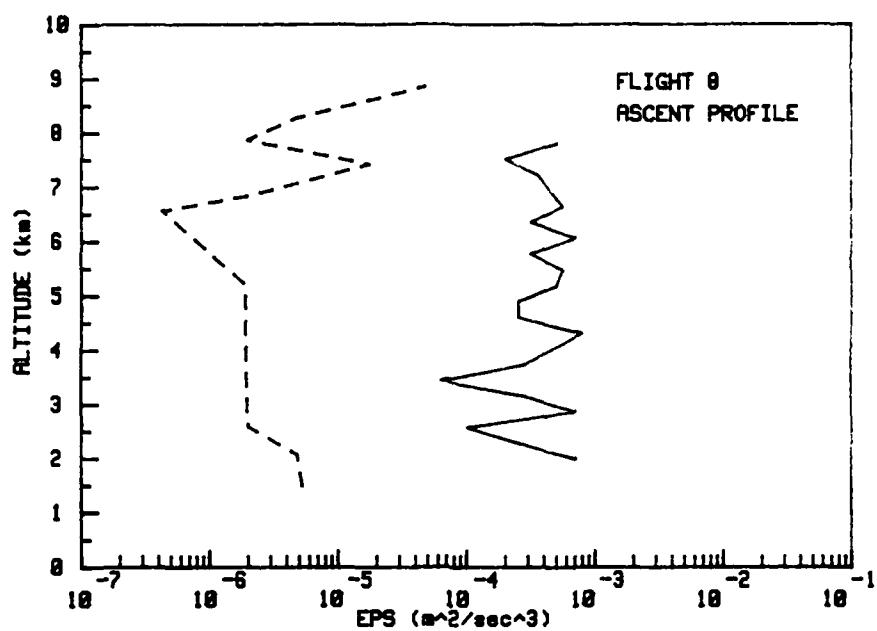


Figure 29. (continued)

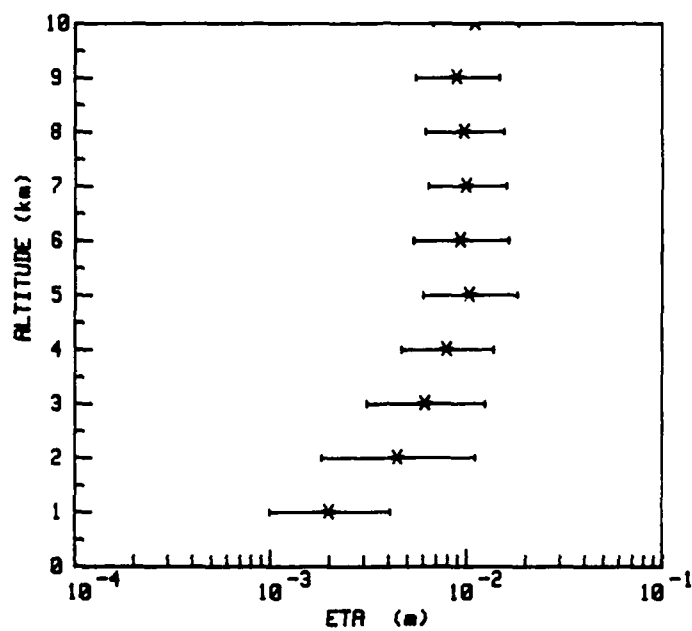


Figure 30. Average vertical profile of η , the turbulence inner size scale, from aircraft-measured epsilon profiles. Altitude is MSL

computed for each ϵ value using the previously mentioned formula for ν with the standard atmosphere temperature profile, and then averaged in 1 km layers. The average value of η spans one order of magnitude, from 1 mm in the boundary layer to an average of 1 cm above the boundary layer.

CHAPTER 8

SUMMARY AND CONCLUSIONS

The atmosphere has a temporally and spatially variable refractive index due to its inherently turbulent nature. This can affect electromagnetic beam propagation by introducing beam steering, image dancing, beam spread, spatial coherence degradation, temporal coherence degradation, and scintillation (Dewan 1980). Refractivity is wavelength dependent. At microwave radar wavelengths, molecular composition (e.g., water content) dominates refractivity changes. At visible wavelengths, density (parameterized by temperature) dominates (Balsley and Gage 1980). For many quantification purposes, the refractive index turbulent structure constant, C_n^2 , is a key parameter. This parameter can be inferred from optical turbulence (scintillometer), temperature turbulence (aircraft instrumentation or thermosonde) or radar backscatter (profiler) measurements. However, C_n^2 from a radar profiler will differ because of the wavelength dependence of refractivity. Theoretically, this can be compensated for, if the humidity profile is known (VanZandt et al. 1981). Vertical integrals of C_n^2 give transverse coherence length, r_o , and isoplanatic angle, θ_o . These can also be measured remotely (based on optical turbulence) by an r_o scintillometer and isoplanometer, respectively.

During an atmospheric optics/meteorology experiment (acronym EWAK) conducted at Penn State University primarily during April and May of 1986, data was collected by the aforementioned instruments. AFGL and RADC scintillometers produced vertical profiles of

C_n^2 -optical. An AFGL thermosonde produced vertical profiles of C_T^2 and other meteorological variables. A PSU profiler produced vertical profiles of wind direction and speed, and C_n^2 -radar. The instrumented ARA research aircraft produced vertical profiles of temperature and velocity turbulence (C_T^2 and C_u^2) and other meteorological variables.

An indepth analysis of the aircraft turbulence data was performed. The turbulence instrumentation aboard consisted of cold-wire and hot-wire sensors (for temperature and velocity variations, respectively) and FM recording apparatus. The taped data was processed via FFT to produce one-dimensional variance spectra (wavenumber range 0.01 to 10 m^{-1}). Flights usually produced a 10 km vertical profile; the data was processed to give roughly 0.5 km vertical resolution, similar to that of the profiler.

An atmospheric filter function was derived, based on PBL spectra and -5/3 inertial subrange slope. This function was applied to compensate for low frequency dropoff, as part of a spectral editing program. Editing was based on percent error between a regression analysis and theoretical -5/3 slope. Noise subtraction was performed in some low signal cases. In general, PBL spectra clearly showed the classical -5/3 inertial subrange slope, out to the broadband instrument noise level. A majority of spectra in the free troposphere showed good evidence of the inertial subrange with -5/3 slope. Further data collection should emphasize the low frequencies, since this appears to be the low noise region. Occasional anomalous and low signal-to-noise spectra were encountered above the PBL. Low signal spectra represent quiescent layers. C_T^2 and C_u^2 were

calculated from the regression fit to the inertial subrange power spectral density. The rate of dissipation of turbulent kinetic energy, ϵ , can be calculated by using the so-called Corrsin relation for velocity turbulence. C_n^2 can be calculated from C_T^2 .

Considerable interest has developed in models that relate microturbulence parameters to the mean gradients. One such model, proposed by VanZandt et al. (1978; 1981), has as a key variable the gradient Richardson number, R_i . In actively turbulent regions, R_i can be related to C_T^2 and C_u^2 as follows:

$$C_T^2 / C_u^2 = 1.6 R_i / (P_r - R_i) (\theta/g) (\partial\theta/\partial z) \quad (8.1)$$

A scatter plot of C_T^2 versus $(\theta/g \partial\theta/\partial z) C_u^2$ in the free troposphere has a slope that corresponds to $1.6 R_i / (P_r - R_i)$. This plot showed a range of values from 0.3 to 10 for high and low values of C_T^2 , respectively. Scatter plots of C_T^2 versus C_u^2 showed high correlation of these two parameters, with $\log C_u^2 = 1.7 \log C_T^2$. This implies that the mean gradient structure of the free troposphere would have a probability density maximum (Fairall and Markson 1985). This could be illustrated as a single curve in N-S space, where N is the Brunt-Vaisala frequency squared, and S is the shear squared and $R_i = N/S$. Plots of this type were done using aircraft temperature data and profiler wind data. A distribution was obtained roughly corresponding to the curve depicted by Fairall and Markson (1985). Generally, regions of high shear are at or below the $R_i = 0.25$ line, as expected.

Plots of $C_T^2 / C_u^2 (\theta/g \partial\theta/\partial z)$ versus a turbulent activity parameter (Gregg 1987) clearly show agreement with the suggested

activity levels and associated values. As the ordinate value [corresponding to $1.6 R_i / (P_r - R_i)$] decreases, turbulent activity increases. At high activity levels, the ordinate value approaches 0.4 (equivalent to $1.6 R_i$ when approximating P_r as 1 and R_i as 0.25).

Values of N and S were used to obtain values of C_n^2 and ϵ with the model of VanZandt et al. Comparisons of C_n^2 profiles measured by the various instruments showed good agreement between scintillometer and thermosonde, and between the VanZandt et al. model and the aircraft data. The profiler (converted optical values) had some agreement with the thermosonde. The difference in C_n^2 profiles between methods varied. An average ratio of each profile versus the thermosonde profile gave the following factors for flight 6: aircraft 11.7 (standard deviation 23.4), model 11.5 (stand. dev. 18.5), profiler 4.3 (stand. dev. 5.3), and the scintillometer 1.6 (stand. dev. 0.5). In the lower levels of the flight 6 ascent, the aircraft profile is thought to have an error in gain setting. For flight 8, the factors were: aircraft 4.2 (stand. dev. 4.5), model 2.2 (stand. dev. 2), profiler 12 (stand. dev. 34), and the scintillometer 0.7 (stand. dev. 0.6). Similar differences between aircraft and thermosonde were noted by Brown and Good (1984). It was later thought that this difference might have been due to spectral analysis technique. However, the increased effort to improve spectral analysis in this paper apparently seemed to have little effect. Structure constant values obtained by the two spectral analysis methods examined in this work (FFT board and the signal analyzer) differed on the average by about a factor of two for C_T^2 ; however individual

values differed by as much as two orders of magnitude.

To account for the difference in C_n^2 profiles between instrument systems, further research might seek to determine the difference in values obtained by thermosonde and aircraft instrumentation, since they actually measure some of the same variables (e.g., C_T^2) in slightly different ways. Since the scintillometer tended to agree with the thermosonde and the VanZandt et al. model tended to agree with the aircraft, no clear choice is evident. The radar does not have an absolute calibration, so there is no significance to its agreement with either system (Christopher Fairall, personal communication, December 1987).

Another noticeable difference between the aircraft and thermosonde is the measured vertical profiles of potential temperature. Since potential temperature and its gradient are input parameters in the VanZandt et al. model, this difference could obviously affect model output. Barat and Bertin (1984) state the need for accurate temperature profiles and suggest changes in Richardson number depend more on temperature gradient than on shear. This study only used aircraft data as model input. Comparing model output from thermosonde and aircraft input could be another interesting comparison for further study. There is also an obvious need for additional simultaneous data collection. Logistical and weather problems contributed to make only two nights of simultaneous operation possible during EWAK.

Numerical integration of C_n^2 gave estimates of r_0 and θ_0 . Values from scintillometer, thermosonde and aircraft did not show consistent agreement. Based on the aircraft values, both the

scintillometer and thermosonde differed by an average of 17% for θ_0 , and the thermosonde differed by an average of 35% for r_0 . With such a limited data set it is not possible at this time to conclude whether profiles of C_n^2 can be used to estimate these optical parameters. Acceptable approximations for unmeasured segments of the atmosphere must also be further studied.

Despite good agreement on C_n^2 , the aircraft data and the VanZandt et al. model output clearly disagreed on vertical profiles of ϵ . This difference was also noted by Fairall and Markson (1985). They suggest this effect is due to the adjustment of the model parameter L , turbulent layer thickness, to produce the best fit of model output to profiler C_n^2 data. Since few measurements of ϵ have been done, there is a definite need for a larger data base. Other areas of study might include adjusting L to best fit aircraft ϵ profiles. However, this would require either adjusting the constants (a and b) in the model equations or modifying the theory in order to preserve the good predictions for C_n^2 . Raw high speed aircraft data could also be used to study turbulent "episodes" individually without vertical averaging. The fraction of the profile that is actually turbulent could be computed and the microturbulence ratio could be examined for each active layer.

Overall, EWAK provided a chance to compare methods of measuring C_n^2 , as well as an opportunity to obtain microturbulence data that has some relation to the mean gradient structure. Hopefully, further research will provide a relationship that could be exploited in future predictive models.

REFERENCES

- Balsley, B. B. and K. S. Gage. 1980. The MST radar technique: Potential for middle atmospheric studies. Pure Appl. Geophys. 118: 452-93.
- Barat, J. and F. Bertin. 1984. Simultaneous measurements of temperature and velocity fluctuations within clear air turbulence layers: Analysis of the estimate of dissipation rate by remote sensors. J. Atmos. Sci. 41: 1613-19.
- Brown, J. H. and R. E. Good. 1984. Thermosonde and UHF radar measurements of C_u^2 at Westford, Massachusetts- July 1981. AFGL-TR-84-0109. Hanscom AFB.
- Brown, J. H., R. E. Good, P. M. Bench, and G. Faucher. 1982. Sonde experiments for comparative measurements of optical turbulence. AFGL-TR-82-0079. Hanscom AFB.
- Champagne, F. H., C. A. Friehe, J. C. LaRue, and J. C. Wyngaard. 1977. Flux measurements, flux estimation techniques, and fine scale turbulence measurements in the unstable surface layer over land. J. Atmos. Sci. 34: 515-30.
- Dewan, E. W. 1980. Optical turbulence forecasting: A tutorial. AFGL-TR-80-0030. Hanscom AFB.
- Eaton, F. D., W. A. Peterson, J. R. Hines, and G. Fernandez. 1985. Isoplanatic angle direct measurements and associated atmospheric conditions. Applied Optics 24: 3264-73.
- Environmental Science Services Administration, National Aeronautics and Space Administration, and United States Air Force. 1966. U. S. Standard Atmosphere Supplements, 1966. Washington, D. C.: U. S. Government Printing Office.
- Fairall, C. W. and R. Markson. 1984. Aircraft measurements of atmospheric velocity and temperature microturbulence spectra. Dept. of Meteo. Tech. Report. Pennsylvania State University.
- Fairall, C. W. and R. Markson. 1985. Aircraft measurements of temperature and velocity microturbulence in the stably stratified free troposphere. Seventh Symposium on Turbulence and Diffusion. American Meteorological Society (12-5 November): 180-3.
- Fairall, C. W. and R. Markson. 1987. Mesoscale variations in surface stress, heat fluxes, and drag coefficient in the marginal ice zone during the 1983 marginal ice zone experiment. J. Geophys. Res. 92: 621-32.

REFERENCES

- Fairall, C. W. and G. E. Schacher. 1977. Frequency response of hot wires used for atmospheric turbulence measurements in the marine environment. Rev. Sci. Inst. 48: 12-7.
- Fairall, C. W. and D. W. Thomson. 1985. Some preliminary comments and conclusions on radar-performance-related parameters extracted from CAPTEX raob sounding measurements. Dept. of Meteorology Tech. Report. Pennsylvania State University.
- Fried D. L. and G. E. Mevers. 1974. Evaluation of r_o for propagation down through the atmosphere. Applied Optics 13: 2620-2.
- Gregg, M. C. 1987. Diapycnal mixing in the thermocline: A review. J. Geophys. Res. 92: 5249-86.
- Hecht, E. 1986. Optics. 2d ed. Reading: Addison-Wesley.
- Hill, R. J. and S. F. Clifford. 1978. Modified spectrum of atmospheric temperature fluctuations and its application to optical propagation. J. Opt. Soc. Am. 68: 892-9.
- Hinze, J. 1975. Turbulence. 2d ed. New York: McGraw-Hill.
- Iribarne, J. V. and W. L. Godson. 1981. Atmospheric thermodynamics. 2d ed. Dordrecht: D. Reidel.
- Kennedy, P. J. and M. A. Shapiro. 1980. Further encounters with clear air turbulence in research aircraft. J. Atmos. Sci. 37: 986-93.
- Loos, G. C. and C. B. Hogge 1979. Turbulence of the upper atmosphere and isoplanatism. Applied Optics 18: 2654-61.
- Murphy, E. A. and F. P. Battles. 1986. Isoplanatic angle from stellar scintillometer measurements at Pennsylvania State University. Private communication AFGL-TM-129. Hanscom AFB.
- Nastrom, G. D., K. S. Gage, and B. B. Balsley. 1981. Variability of C_n^2 at Poker Flat, Alaska, from mesosphere, stratosphere, troposphere (MST) Doppler radar observations. Proceedings of the SPIE 277: 10-5.
- Ochs, G. R., R. S. Lawrence, T. Wang and P. Zieske. 1976. Stellar-scintillation measurement of the vertical profile of refractive-index turbulence in the atmosphere. Proceedings of the SPIE 75: 48-53.

REFERENCES

- Ochs, G. R., T. Wang, and E. Merrem. 1977. Stellar scintillometer model II for measurement of refractive turbulence profiles. Tech. Memo. ERL WPL-25. National Atmospheric and Oceanic Administration.
- Ottersten, H. 1969. Atmospheric structure and radar backscattering in clear air. Radio Sci. 4: 1179-93.
- Panofsky, H. A. and J. A. Dutton. 1984. Atmospheric diffusion. New York: John Wiley and Sons.
- Stevens, K. B. 1985. Remote measurements of the atmospheric isoplanatic angle and determination of refractive turbulence profiles by direct inversion of the scintillation amplitude covariance function with Pikhonov regularization. Ph. D. diss., Naval Post-graduate School, Monterey.
- Strauch, R. G., A. S. Frisch, and B. L. Weber. 1986. Wind measurements in the upper troposphere with UHF and VHF radar. 23rd Conference on Radar Meteorology Preprints 1 (22-6 September): 48-51.
- Strohbehn, J. W., ed. 1978. Laser beam propagation in the atmosphere. Berlin: Springer-Verlag.
- Tatarskii, V. I. 1971. The effects of the turbulent atmosphere on wave propagation. Jerusalem: Israel Program for Scientific Translations.
- Wallace, J. M. and P. V. Hobbs. 1977. Atmospheric science an introductory survey. New York: Academic Press.
- Wesely, M. L. 1976. The combined effects of temperature and humidity fluctuations on refractive index. J. Appl. Meteo. 15: 43-9.
- VanZandt, T. E., J. L. Green, K. S. Gage, and W. L. Clark. 1978. Vertical profiles of refractivity turbulence structure constant: Comparison of observations by the Sunset Radar with a new theoretical model. Radio Science, 13: 819-29.
- VanZandt, T. E., K. S. Gage and J. M. Warnock. 1981. An improved model for the calculation of profiles of C_n^2 and ϵ in the free atmosphere from background profiles of wind, temperature and humidity. Twentieth Conference on Radar Meteorology Preprints. (30 November to 3 December): 129-35.